Slow mergers of massive stars

Natalia Ivanova

Balliol College, Oxford

April 2002
Thesis submitted for the degree of Doctor of Philosophy

Declaration

I declare that no part of this thesis has been accepted, or is currently being submitted, for any degree or diploma or certificate or any other qualification in this University or elsewhere.

This thesis is the result of my own work unless otherwise stated. The original evolutionary code has been given by Dr. Ph. Podsiadlowski. The reaction library data and code for reaction rates has been provided by Dr. R. Cannon (the reaction libary data orginally has been provided by Thielemann group). The hydrodynamical code PROMETHEUS has been provided by Dr. E. Müller (MPIA). Chapter 4 involved collaboration with Dr. H. Spruit (MPIA).

Natalia Ivanova

Balliol College, Oxford

Submitted for the Degree of Doctor of Philosophy

April 2002

Abstract

Most stars are members of binary or multiple systems, and up to 50% of binaries are interacting at some stage during their evolution. One of the most important evolutionary channels for an interacting binary involves the spiral-in of the two components inside a common envelope. The result of this evolutionary channel is either that the binary survives and forms a short-period binary, or that the binary components merge completely to form a rapidly rotating single star. If the resulting single star is sufficiently massive, it will continue its evolution until it will explode as a core-collapse supernova.

This thesis is primarily devoted to modelling the complete slow merger of a massive binary within a common envelope and the detailed subsequent evolution of the object produced as a result.

Chapter 1 presents an overview of our current understanding of common-envelope evolution, concentrating on massive stars. We also discuss the progenitor of SN1987A as a possible example of a merger product. In Chapter 2, we analyse the different processes involved in the spiral-in of the secondary which precedes the merger phase. We briefly describe the code we use to simulate this stage and discuss in detail how this evolution varies within the range of uncertainties of the input parameters.

The following chapter investigates the behavior of the stream emanating from the secondary when it fills its own Roche lobe inside the common envelope, but before the effect of the common envelope becomes significant. We describe the model to estimate the mass-loss rate from the secondary within the common envelope. We also analyse the behavior of the stream in the vicinity of L_1 and discuss the physics of a stream formed for an asynchronously rotating secondary. For this case we provide a new formalism for calculating the trajectory of the stream. We then describe the code calculating quasi-ballistic trajectory for the stream and discuss the results of the ballistic calculations.

Chapter 4 is devoted to the study of the stream behavior during the early stages of the merging from a hydrodynamical point of view. Our main objective is to estimate how deep the stream can penetrate depending on its initial parameters and on the structure of the ambient medium. We discuss different physical processes affecting the stream dissipation and, based on the results of our simulations, we provide a simple recipe that allows the determination of the stream penetration

depth for a wide range of conditions.

In Chapter 5 we describe how we model the merger using a stellar evolution code and discuss the key factors which affect the results of the merger. Three different regimes for the merger have been identified which result in qualitatively different post-merger evolution and envelope composition. The "quiet merger" case does not lead to significant changes in composition, and the star remains a red supergiant. In the case of a "moderate merger", the star may become a blue supergiant and end its evolution as a blue supergiant, depending on the core to total mass ratio. In the case of the most effective "explosive merger" the merger product stays a red giant. In the last scenario the composition change proceeds in two phases when the merger product is a RSG: during the merger and during a delayed dredge-up phase (a few thousand years after the merger). A BSG, which can only be formed in the case of a "moderate merger" scenario, appears to experience only one dredge-up phase. Significant s-processing is mainly expected in the case of the "explosive merger" scenario. The "moderate merger" can create a single merged object with the main characteristics of the progenitor of SN1987A. An "explosive merger" may be responsible for the creation of such objects as V Hydrae, i.e. a rapidly rotating red supergiant with anomalous carbon abundances.

Acknowledgements

I would like to thank my supervisor, Philipp Podsiadlowski, for his support, guidance and enthusiasm throughout. Most of my knowledge about specific features of evolution I gained from discussions with him. I am very grateful to Henk Spruit who directed me in the right way at the start of my hydro-simulations epoch, and later for his comments of the results in Chapter 3 and Chapter 4. Particular thanks I have to Alexei Kritsuk: without him it will be no code for the video representation of hydro-simulations. I am also very grateful to Dmitri Novikov for long lasting discussions regarding different aspects of hydrodynamics.

On the personal level, I am most grateful to my friends Sema, Dima and Olya, who supported me really hard, especially at the end of the DPhil. And to all my Oxford friends for full of life years I had in Oxford and for all hike trips we did together.

I would like to acknowledge the financial support by scholarship the Dulverton Trust. Also I would like to thank Mr. George Soros for the given me possibilityto come to Oxford in 1997 , since all what has happened since then, including this thesis, has happened because of that.

Now this is not the end.
It is not even the beginning of the end.
But it is, perhaps, the end of the beginning.

Winston Churchill, 1942

Contents

Chapter 1

Introduction

Common envelope (CE) evolution is one of the most interesting evolutionary stages of an initially close binary. This is the stage when the two components of a binary system orbit inside a common, extended envelope, which is not in synchronous rotation with the embedded binary (Iben and Livio 1993). Historically the concept of CE evolution came from attempts to understand how cataclysmic variables have formed. Being short period binaries, with an accreting white dwarf and a Roche-lobe overfilling main-sequence (MS) star as components, these systems are characterized by very low angular momentum. It was first proposed by Ostriker (1975) (in the contest of massive binaries containing a neutron star) and by Paczyński (1976) (for cataclysmic variables) that this kind of system is the result of the evolution of an initially long period binary, which has undergone one or more phases of angular momentum and mass loss. The transformation from a system with high angular momentum to one of low angular momentum then necessarily involves a phase when the more evolved companion (a red giant star) swallows the companion inside a differentially rotating envelope.

Three possible mechanisms have been proposed to describe how a binary encounters a CE phase. *First* as originally described by Darwin at the end of the last century is the dynamical instability, also known by various other names as secular instability, tidal instability, or gravo-gyro instability (for more recent discussion see Hut 1980, Lai, Rasio and Shapiro 1993, 1994). The tidal instability occurs when the mass transfer starts from the mass-loosing star which is not in a corotation with the binary rotation (if it were not enough of the orbital angular momentum in the system initially to transfer it to the giant envelope to spiral it up to the corotation state). More precisely, it takes place when the moment of inertia of the more evolved star (or the sum for both stars) exceeds one third of the orbital moment of the inertia (Hut 1980). Then, if the mass the companion is very low, it may fall into the envelope of the primary. The tidal instability occurs only for mass ratios $\geq 5-6$ for evolved red giant stars (Taam and Sandquist 2000). *The second* case can happen in nova systems because of the expansion of the nova shell engulfing the companion. *The third*, considered as the most important situation leading to the formation of a CE system, is a consequence of a dynamical mass transfer event. It happens when the more massive and more evolved primary (a giant or AGB star) has a well developed convective envelope and, after filling its Roche lobe, starts to transfer mass to the secondary. If the angular momentum and total mass are conserved, the orbit shrinks while the mass losing star expands, and therefore the degree of Roche lobe overflow increases – mass transfer becomes dynamically unstable. If the accreting star is not able to accrete all the matter transferred from the donor star, then at some stage it will be surrounded by the primary's envelope. It has been also shown that a red giant star undergoing the adiabatic mass loss responds with expansion of the convective envelope whenever the convective envelope exceeds 50% of the stellar mass (Hjellming and Webbink 1987, Hjellming 1989), therefore the degree of the Roche lobe overflow in such a star increases during the mass transfer.

Once a common envelope has formed, the secondary continues to orbit around the core of the primary within this common envelope (which is composed of material from the giant's envelope). As the secondary is affected by various drag forces due to its interaction with the envelope, the orbit of the binary slowly shrinks. The transfer of angular momentum from the orbital motion to the envelope causes the spin up of the envelope. The final result of this slow spiral-in depends on how much of the released orbital energy has been deposited into the envelope compared to the binding energy of the envelope. The deposited frictional energy may drive expansion of the envelope, causing its partial or complete ejection. If most of the envelope has been ejected, the binary survives as a close binary consisting of the core of the primary and the secondary. This evolutionary path provides the favorite channel for the formation of a short-period binary with compact components.

The primary area of interest of the research in this thesis is the situation when the deposited energy is not sufficient to eject the common envelope. Then the spiral-in continues until the secondary starts to fill its own Roche lobe and begins to transfer mass to the core of the giant. Eventually, the binary will merge resulting in the formation of a rapidly rotating single star. During this merger, the material from the secondary forms a stream which emanates from the secondary and falls towards the primary core, encountering an ambient medium with increasing pressure and density. This hydrogen-rich material may penetrate to a depth of about 10^{10} cm, where the temperature of the ambient matter may be as high as few 10^8 K. This deep penetration may have two major consequences:

– the initiation of hydrogen burning through the hot-CNO cycle which may provide a neutron flux sufficient for efficient s-processing;

– the injection/generation of high entropy material near the primary core which may lead to the dredge-up of helium, eventually changing the surface composition of the merger product.

Both effects will sufficiently change the chemical composition of the merger product, which will eventually became a supernova progenitor. As an example, the progenitor of SN 1987A had a number of atypical features within the framework of the normal evolution theory.

The Blue-Supergiant Progenitor. The normally expected progenitor for a Type II supernova is a red supergiant, but the progenitor of SN 1987A, known as $Sk - 69^{\circ}$ 202, was a blue supergiant (BSG), a more compact object, which supposedly experienced a blue loop after the red supergiant stage. It may have been that it was a single $B3$I star or a binary with faint components, and that no luminous red supergiant was a component of $Sk - 69^{\circ}$ 202 (e.g. Blanko 1987; White, Graeme and Malin 1987; for detailed quantitative estimate of the magnitude of a red supergiant consistent with the observed colours see the discussion in Joss *et. al* 1988). Using evolutionary calculations and observations, the mass of the progenitor has been estimated as $19 \pm 3M_{\odot}$, the radius as $3 \pm 1 \times 10^{12}$ cm, the mass of the helium core at the exploding time as $6 \pm 1M_{\odot}$, with a radius of $5 \times 10^{10} cm$, a luminosity $3 - 6 \times 10^{38}$ ergs s^{-1}, an effective temperature $15.000 - 18.000K$ and an iron core mass of $1.45 \pm 0.15M_{\odot}$ (Woosley 1988).

Triple structure of the nebula. Observations of the nebulosites near SN 1987A in 1989 show that the structure of the circumstellar matter around the supernova is very none spherical (Wampler *et al.* 1990). The approximately axisymmetric nebula surrounding the supernova consists of three rings – the inner ring with the supernova at the center and two rings shifted to the South and North. The dynamical age of the inner nebula around the progenitor has been estimated as $1.5 \div 2 \times 10^4$ y

(Crotts and Heathcote 1997; Meyer 1997; Smith *et al.*, 1998), which is consistent with the estimate of the duration of a late blue loop for a massive star as $\approx$ 20000 y for a model star of $20M_{\odot}$ with a low-metallicity composition $Z = 1/4Z_{\odot}$ (Woosley 1988; also see Langer, El Eid and Baraffe 1989)[1]. It implies that the star became a BSG very recently. It was suggested that this nebula could be the result of two distinct shell injections when the progenitor was in its RSG phase (Wang and Mazzali 1991), if it was a fast rotator at this stage (Chevalier and Soker 1989). But the rotation speed, required for this, is atypical for the RGB star – usually a single star, which is rotating fast at the main sequence, will be a slow rotator in any subsequent supergiant phase.

<u>*The chemical anomalies.*</u> There are a few clues to the chemical composition of the progenitor. Two of them correspond to the composition of the inner and outer rings in the nebula. The composition of CNO elements there shows that there were two ejections at different stages of the RGB phase. The inner ring is overabundant in He as well (factor 2 to solar) (Höflich 1988; Allen, Meikle and Spyromilio 1989; Fransson *et. al* 1989; Wang 1991; Lundqvist and Fransson 1996; Sonneborn *et. al* 1997). The outer rings show smaller abundances of CNO-processed material (Panagia *et. al* 1996). This amount can be associated with the normal convective dredge-up in a massive star.

A very interesting chemical anomaly was revealed by the chemical abundances of the ejected envelope during the early stages of the SN 1987A explosion. The matter ejected first had an unusual chemical composition with regard to the s-elements, which were overabundant. Most heavy elements are approximately 3 times less abundant than in Sun (Höflich 1988), and those values are more or less consistent with the chemical abundances of the LMC, where heavy elements 2 times less abundant than in Sun (Russel and Dopita 1992). But in the early-time spectra of SN 1987A the strong Ba II 6141 line and other s-elements have been found (Williams 1987a; 1987b). Detailed atmospheric calculations for overabundances of s-elements have show that Sc, V, Cr, Sr are about 2 times greater than the solar abundance, Ti is about solar, Ba is 10 solar and Na is about 5 solar (Höflich 1988; Mazzali, Lucy and Butler 1992).

Also in June 87 overabundances of helium by a factor of $1-2$ in the hydrogen rich layers have been seen (Höflich 1988). The mass of the H-rich layers has been estimated to be about $9-11M_{\odot}$

[1]Currently, with the new OPAL stellar opacities, the evolutionary scenario where a single star experiences a late blue loop is more difficult to achieve, especially for models with rotation (Woosley *et al* 1997).

(Höflich 1988) and $7 - 11 M_\odot$ (Saio, Nomoto and Kato 1988a). It has been suggested that almost the whole ejected envelope was uniformly mixed (possibly because of rapid rotation) and that the CNO composition in the ejected material was $N/C \approx 30(N/C)_\odot$ and $N/O \approx 10(N/O)_\odot$ (Saio, Nomoto and Kato 1988).

Later calculations of synthetic spectra have confirmed that there are overabundances of Ba of at least a factor of 5 to the supposed initial one and this overabundance is necessary for all layers in the ejecta with velocity between 1500 and 9000 km s^{-1}, which includes almost all of the ejected mass (89%)(Mazzali and Chugai 1995) . For Sr the overabundance factor is 2 over the adopted LMC metal abundance and there is no Sc overabundance .

To produce s-elements close to observed distributions, it is necessary to have a neutron flux of about $10^{15} - 10^{16}$ cm^{-2} s^{-1} (Chechev and Kramarovskii 1981). Such a flux can be the result of hydrogen burning in high-temperature region – the hot CNO cycle (in this case (α, n) reactions will take place, e.g., on the ^{13}C,^{17}O,^{21}Ne,^{25}Mg isotopes). The temperature at which this nucleosynthesis will be effective corresponds to a He burning temperature. In a star the helium burning region is generally void of any hydrogen. Therefore, this kind of nucleosynthesis can only take place in the case of the injection of hydrogen into the helium burning region. Such a process occurs in intermediate mass stars in the AGB phase. Weak s-processing occurs in a massive star during helium core burning (Busso and Gallino 1985; Langer, Arkorogi and Arnould 1989) and s-processing can play a minor role during C-shell burning (Raiter *et al.* 1993). A substantial neutron density in the case of helium core burning is provided by the reaction $^{22}\mathrm{Ne}(\alpha, n)$ and the resulting neutron flux strongly depends on the rate of the concurrent reaction $^{22}\mathrm{Ne}(\alpha, \gamma)$. But elements created in more or less sufficient quantity will be so-called “light s-elements”, i.e. elements in the range $A < 90$ (Raiter *et al.* 1993, Baraffe , El Eid and Prantzos 1993), and so the s-process in a normal massive star cannot explain the overabundance of Ba in the SN 1987A progenitor (Langer, Arkorogi and Arnould 1989; Mazzali and Chugai 1995).

The described peculiarities, such as the hypotheses of a rapidly rotating progenitor, efficient mixing of the envelope and the s-processing for elements with $A \rightarrow 130$ (Ba) are not in agreement with standard stellar evolution calculations, and it has been proposed that the progenitor of the SN 1987A was the result of the merger of two stars(Podsiadlowski, Joss and Rappaport 1990; for detailed review see Podsiadlowski 1992 and Podsiadlowski 1997; also see Hillebrandt and Meyer 1989).

As a metal-poor, sub-luminous and s-overabundant supernova of type II, SN 1987A is not a unique supernova with these peculiarities – the spectrum of SN 1990H is very close to that of SN 1987A. Although 12 weeks after core collapse, the Ba II line in SN 1987A was relatively stronger than in SN 1990H, it has been suggested that its physical nature is similar to that of SN 1987A (Filippenko and Dickinson 1990). Another recently observed object – SN 1999A – also shows strong absorption lines of s-process elements (Ba, Sc) and this object also appears to be sub-luminous (Filippenko and Hamann 1999).

After the concept of CE evolution has been introduced by Paczyński and Ostriker, a substantial amount of work in the field has been done. Modeling common-envelope evolution involves consideration of many physical processes, mainly important at different phases and characterized by different time scales. Therefore different numerical tools should be applied. E.g., the purely hydrodynamical phases of the CE evolution using hydrodynamical modeling have been significantly studied in the studies of of Taam, Bodenheimer, Ostriker, Sandquist, Livio, Rasio (for review see Taam and Sandquist 2000, Taam and Sandquist 1998). It involves 3-d simulations using SPH and 2-d and 3-d grid based hydro-methods. The slower, quasi-hydrostatic phases of the spiral-in have been modeled by Meyer and Meyer-Hofmeister 1979 (MMH) using an evolutionary code. In particular, they have shown that, once the envelope has expanded, a phase of self-regulated spiral-in may follow in which all the frictional energy that is released by the spiraling-in binary can be transported to the surface by convection and be radiated away without causing any ejection of the envelope. Nevertheless, the question of the merging phase for massive stars binary has not been explored in any detail to date.

In this thesis we are considering the situation called the slow merger of massive stars. Though the merger itself is a very special process, the general picture of the problem consists of several consecutive stages and processes. These stages are initial conditions for the consequent stages and therefore should be all considered; also the stellar evolution is not finished after the merger is completed. Shortly these stages and processes are the spiral-in of the secondary and its interaction with the primary envelope; the mass transfer from the secondary; the interaction of the transferred matter with the primary; the further evolution of the merger product. In more detail:

Once the secondary enters the primary envelope (by one of the three mechanisms described at the start of this Chapter), the evolution of the primary cannot be described in terms of single star evolution any more. The spiralling-in secondary changes the structure of the common envelope formed from the primary envelope material, transferring continuously energy into the CE. Sources of this energy are orbital energy and the potential energy of the primary envelope material released due to the accretion on the secondary. Presence of the secondary within the common envelope changes the gravitational field affecting the envelope as compared to the single star case. The angular momentum transferred into the CE is redistributed over the envelope, creating differentially rotating shells. The kinetic energy of differentially rotating shells is released as the heating energy due to viscous friction. All these details should be taken into account in order to obtain most realistic initial conditions for further stages, like mass transfer.

The spiral-in goes until either the common envelope is ejected, or, if not enough orbital energy was deposited into the envelope, the fast stage of the spiral-in (plunge-in) is replaced by the slower spiral-in, when the deposited energy is almost balanced with the energy radiated away. When the binary orbit shrinks enough and the secondary overfills its own Roche lobe, the mass transfer from the secondary toward the primary core starts. This mass transfer is not usual, compared to the case of normal mass transfer in a close binary: the stream of the material from the secondary is formed within the hot and dense envelope. The stream structure (density profile over the stream cross-section) is mainly determined by the potential field at the vicinity of L_1. If the secondary is not in corotation with the orbital motion, the stream behavior at the point where stream is formed might be different from the case of the secondary in corotation. The trajectory of the falling stream is also affected by the presence of the ambient material. This situation is close to the case of a jet ejected into the interstellar medium. The difference is that in the case considered the gravitational field, as well as the pressure and the temperature are increasing in the direction of the stream propagation. Also, as ejected jet is normally a single event, and its propagation is strongly defined by the energy dissipation at the jet head, while in the case of the flow emanating from the secondary we have ”infinite” source of the material (”infinite” since the time-scale of the mass transfer is much larger than the dynamical timescale of the stream fall). It is also should be mentioned that the stream trajectory can be approximately divided into 2 parts: the part when the ambient pressure does not affect much the stream structure and the part where the ambient pressure is already so high that its effect on the stream should be calculated in details. Uncertainties in the result of the interaction between the stream and the ambient material are increased due to possible presence of rotation in some form in the ambient medium, like partial non-corotation of the ambient medium with the binary orbital motion or like faster rotation of the core due to its spinning up during the mass transfer. These uncertainties, plus change of the primary pressure and temperature profiles within the region of interest during the evolution, and plus possible nucleosynthesis within the stream and in the surrounding medium makes the problem of the stream penetration complicated.

While we listed before only problems connected with the stream as the result of the primary effect, the effect of the stream penetration on the primary structure is even more complicated and is the main aim of our study. On the one hand, the structure of the primary star should be calculated with all effects which take into account the presence of the secondary within the envelope, as described above. Additionally the mass loss rates should be calculated, and this is not possible without separate calculation of the secondary response on the mass loss in such extreme conditions as hot and dense ambient medium. It also required detailed calculations of the orbital separation evolution. Even nowadays it is not possible to make hydrodynamical simulations for each time-step of evolutionary calculation during the merger for the stream-core interaction, which is necessary to calculate how deep the hydrogen rich material could penetrate – we need a parameterized model for these interactions. Being placed into hot medium, the hydrogen rich material starts intensive (and sometime explosive) nucleosynthesis. This gives rise to two effects. First of all, it raises the question about the intensive mixing in the region of this burning. On the other hand, the nucleosynthesis taking place will not necessarily be typical (in terms of standard single star evolution). Also, this burning might proceed on the timescale which is comparable with the timescale of the mixing in the burning region, and therefore a special numerical method for calculations of chemical species evolution should be used in such a region.

This thesis will attempt to model the merger phase using appropriate numerical tools for different sub-problems. Chapter 2 focuses on the modeling of the evolution of the primary star during the slow spiral-in of the secondary. We present a model describing the secondary-envelope interaction and discuss results of this modeling for a few types of CE systems. The main goal of these calculations is the creation of the initial conditions within the CE for the subsequent calculations at the merging stage. In Chapter 3 a few aspects concerning the earliest stages of the mass outflow are discussed. It includes such sub-problems as the formation of the stream in the L_1 neighborhood, the effect of the secondary's asynchronized rotation and calculations of the stream trajectory at the beginning of its fall. Chapter 4 is devoted to the consideration of different aspects of the hydrodynamical simulations of the stream infall. We analyze the behavior of a stream depending on the different conditions in the primary envelope and discuss the mechanisms of jet dissipation. Finally, in Chapter 5 the problem of the modeling of the primary star during the merging is discussed.

Chapter 2

CE: Spiral-In Stage

When the primary star evolves to the supergiant stage , its envelope expands and, for an initially close binary, starts to fill its Roche lobe. In this case the subsequent mass loss from the primary and accretion of this material onto the secondary will cause the orbit of the binary to shrink as long as the primary is more massive then secondary. If the accreting companion can not accrete all of the material lost from the primary, the secondary enters into the primary envelope, forming a system consisting of the primary core, the secondary star and a common envelope (CE). Due to the frictional drag between the stellar components and the envelope, the orbit of the immersed binary continues to shrink. The secondary continues to accrete material from the primary and the accretion luminosity heats up the CE. Angular momentum of the shrinking binary is transferred from the orbital angular motion to the CE, causing its spin-up. Subsequently some layers of the envelope start to rotate faster than others. In the viscous medium the differential rotation transforms the kinetic energy of the envelope to heat. The spiral-in stage continues up to the moment where the secondary starts to overflow its Roche lobe, when mass transfer from the secondary into the CE starts. As a result of the spiral-in the structure of the CE has changed and therefore it is necessary to consider this stage to obtain the initial conditions for the later merging phase.

In this chapter we describe how we model the spiral-in of the secondary star in a CE (until secondary RLOF). In Section 1 the energy and angular momentum balances during the binary orbit decay are considered. Also, the adopted model of viscous friction is discussed. Section 2 presents the model of diffusive evolution of the angular momentum in the primary star. Section 3 contains the results of numerical simulations and discussion.

2.1 Energy and angular momentum balance

For our simplified spiral-in calculations we follow the conservation of the total angular momentum of the CE system. This total angular momentum is composed of the orbital angular momentum and of the spin angular momentum of each component:

$$J_{\mathrm{CE}} = J_{\mathrm{orb}} + J_{\mathrm{P}} + J_{\mathrm{S}} \ . \tag{2.1}$$

The angular momentum of the primary here consists mainly of the angular momentum of the common envelope. The angular momentum of the primary core can be neglected from the consideration, since the core is very dense and compact and contains little angular momentum.

Loss of the total angular momentum is caused only by the equatorial stellar wind:

$$\dot{J}_{\mathrm{CE}} = -\dot{M}_{\mathrm{sw}} R_{\mathrm{p}}^2 \Omega_{\mathrm{surf}} \ .$$

Here R_{p} is the radius of the common envelope and Ω_{surf} is the surface angular velocity.

The orbital angular momentum changes due to the the binary-CE interaction. In particular, the viscous, the gas and the tidal frictions cause transfer of angular momentum from the orbital angular momentum to the common envelope, and $\dot{J}_{\mathrm{P}} = -\dot{J}_{\mathrm{orb,\ drag}}$. The rate with of this transfer can be found from considering the rate of the orbit dissipation.

The total energy of the CE system consists of the orbital energy of the binary, of potential energies of both components and of thermal energies of both components. The orbital energy is dissipate due to the mentioned drag forces: viscous, gas and tidal friction. The rate of the orbital separation dissipation due to the drag forces can then be written then as the following:

$$\left(\frac{d\ln D}{dt}\right)_{\dot{M}_{\mathrm{acc}}=0} = -\frac{\dot{E}_{\mathrm{orb}}}{E_{\mathrm{orb}}} = \frac{\dot{E}_{\eta}}{E_{\mathrm{orb}}} + \frac{\dot{E}_{\mathrm{gas}}}{E_{\mathrm{orb}}} + \frac{\dot{E}_{\mathrm{tid}}}{E_{\mathrm{orb}}} \tag{2.2}$$

Here D is the binary separation, $\dot{E}_{\eta}$ and $\dot{E}_{\mathrm{gas}}$ are the rate of loss of orbital energy because of viscous and gas friction and $\dot{E}_{\mathrm{tid}}$ is the rate of orbital energy dissipation due to the tidal friction.

The mass exchange between the components (accretion on the secondary), expansion or contraction of the primary within the orbit or mass loss from the primary's surface (and in general case $\dot{M}_{\mathrm{p}} \neq \dot{M}_{\mathrm{s}}$) also causes a change in the orbital separation. In the assumption that the mass exchange and the primary expansion or contraction do not cause change in the orbital angular momentum (or, in other words, during such interactions, the orbital angular momentum is not transferred from orbital angular momentum to the rotational angular momentum of the primary or of the secondary), the resulting rate of the orbit change can be found as the following:

$$J^2_{\rm orb} = G\frac{M_{\rm p}^2 M_{\rm s}^2}{M_{\rm p}+M_{\rm s}} D \tag{2.3}$$

$$\left(\frac{d\ln D}{dt}\right)_{\dot M_{\rm p}, \dot M_{\rm s} \neq 0} = -\frac{\dot M_{\rm s}}{M_{\rm s}}\frac{2M_{\rm p}-M_{\rm s}}{M_{\rm p}+M_{\rm s}} - \frac{\dot M_{\rm p}}{M_{\rm p}}\frac{2M_{\rm s}-M_{\rm p}}{M_{\rm p}+M_{\rm s}} \tag{2.4}$$

Here $M_{\rm p}$ is the mass of the of the primary inside the secondary orbit, $M_{\rm s}$ is the secondary mass.

The total orbital dissipation rate can be found as the sum of orbit dissipations due to different reasons as in equations 2.2 and 2.4. In the following subsections we describe this in more details.

2.1.1 Interaction with the ambient medium: viscous and gas friction

Viscosity model

The nature of viscosity depends on the location of the secondary inside the envelope.

Convective regions. In stars convection is normally considered to be turbulent in nature. The coefficient of the turbulent viscosity is proportional to the speed of a vortex and its size. According to the mixing length theory, an elementary theory of turbulence invented by Prandtl, the speed of a vortex should be the average velocity of a convective element and the characteristic eddy size should be the characteristic length scale at which this vortex will disappear; so for the viscosity $\eta_{\rm c}$ in the convective zone we may use

$$\eta_{\rm c} = \alpha_{\rm c} \rho v_{\rm c} l \ , \tag{2.5}$$

where ρ is the density, $v_{\rm c}$ is the convective velocity and l is the mixing length. $\alpha_{\rm c}$ is a unit-less coefficient of order unity (e.g., in MMH it is taken as 0.5, assuming that convective eddies will disappear after moving half a the mixing length; in Bisnovatyi-Kogan 2001 $\alpha_{\rm c}$ is quoted as 1). The mixing length also contains an uncertain parameter $\alpha_{\rm p} = l/H_{\rm P}$ ($H_{\rm P}$ is the pressure scale) of order unity, which usually is taken to be in a range between $0.5 - 2.0$. By default we use that $\alpha_c = 1$ and $\alpha_p = 2$.

Radiative regions. Normally viscosity in radiative regions can be taken to be the ordinary viscosity (i.e., molecular plus radiative), which is (Schatzman *et al.* 1981):

$$\eta_{\text{rad}} = \frac{4aT^4}{15\kappa c\rho}\,, \tag{2.6}$$

$$\eta_{\text{mol}} = 1.84 \cdot 10^{-17}(1+7X)T^{\frac{5}{2}}\ [\text{g cm}^{-1}\text{s}^{-1}]\,. \tag{2.7}$$

Here κ is the opacity, c is the speed of light, T is the temperature and X is the hydrogen abundance.

The radiative and molecular viscosities are quite small. Apart from these viscosities, which are inherent for laminar layers, it is reasonable to expect the creation of viscosity produced by turbulent motion whenether this turbulence will arise. A variation of the angular velocity with radius, or vertical shear, results in a shear flow instability, the basic mechanism of which is the extraction and clumping of vorticity from a laminar shear flow (Cox , Vauclair and Zahn 1983). Zahn (1992) derived for this case the coefficient of turbulent diffusion taking into account radiative losses from turbulent eddies:

$$\eta_{\text{t}} = \frac{8}{45} Ri_{\text{c}} \rho \frac{K}{N^2} \left(\frac{\partial \Omega}{\partial \ln r}\right)^2\,, \tag{2.8}$$

where Ri_{c} is the Richardson critical number [1] (Cox , Vauclair and Zahn 1983); the described shear instability takes place only if $Ri \leq Ri_{\text{c}} = \frac{1}{4}$ [2].

$$K = \frac{4acT^3}{3\kappa C_P \rho^2}$$

is the thermal diffusivity ($C_P = T\left(\frac{\partial S}{\partial T}\right)_P$ is the specific heat) and

[1]This is a dynamically significant stability indicator. As $Ri \to 0$ convection becomes strong.

[2]In the code we did not calculate Ri and therefore did not make the check for satisfying of criterion for the shear instability, using in 2.8 the maximum possible value $Ri_{\text{c}} = 0.25$. However, it does not produce very wrong result: since $Ri \propto \left(\frac{d\ln r}{dw}\right)^2$, it becomes very large in the case of no differential rotation and should stop the instability and cancel the viscosity. The viscosity calculated using 2.8 will became zero in the case of fixed value for Ri.

$$N^2 = \frac{g}{H_{\rm P}} \left(\nabla_{\rm ad} - \nabla_{\rm rad}\right)$$

is the buoyancy frequency (Brunt-Vaisala frequency) (Cox , Vauclair and Zahn 1983). Here g is the gravity, $\nabla_{\rm ad}$ and $\nabla_{\rm rad}$ are adiabatic and radiative gradients.

Viscous friction

We may consider the secondary star as a sphere, which moves in a viscous medium and looses its kinetic energy due to viscous friction, and deposits this energy in the ambient viscous medium. Under these assumptions the viscous force, which affects the secondary can be written as (see Landau and Lifshitz 1959, the problem of a sphere moving in a viscous medium):

$$F_\eta = 12\pi R_{\rm s}\eta v_{\rm rel} \qquad \text{for} \qquad Re >> 1, \tag{2.9}$$

or

$$F_\eta = 6\pi R_{\rm s}\eta v_{\rm rel} \qquad \text{for} \qquad Re \approx 1, \tag{2.10}$$

Here $R_{\rm s}$ is the radius of the secondary star, $v_{\rm rel}$ is the relative velocity of the secondary star with respect to the ambient viscous medium (which is the common envelope in our case), η is the total dynamical viscosity and Re is the Reynolds number, which for the case of a star moving in a convective zone can be roughly estimated as

$$Re = \frac{2\rho v_{\rm rel} R_{\rm s}}{\eta} \le \frac{2\rho R_{\rm s}}{\eta}\sqrt{\frac{G(M_{\rm p}+M_{\rm s})}{D}} \le 20\ . \tag{2.11}$$

As can be seen from this formula, for the case of a radiative zone, where the viscosity coefficient is normally a few orders of magnitude smaller than in the convective zone, the motion will be intrinsically turbulent, and we can apply there the turbulent diffusion coefficient (2.8).

The rate of energy transfer to the CE is

$$\dot{E}_\eta = F_\eta v_{\rm orb}, \tag{2.12}$$

where $v_{\rm orb}$ is the orbital velocity of the secondary.

We then can estimate the characteristic time of the spiral-in as

$$t_{\text{vis}} \sim \frac{dt}{d\ln D} = \frac{M_{\text{p}}M_{\text{s}}}{(M_{\text{p}}+M_{\text{s}})}\frac{1}{12\pi R_{\text{s}}\eta}\ . \tag{2.13}$$

For a binary system of $20M_\odot$ and $5M_\odot$ and with assumed a typical average viscosity of 10^{11} [g cm^{-1} sec^{-1}] the viscous spiral-in time will be about 300 years. The variability of this energy dissipation rate depends on α_{c} and α_{p} for the turbulent diffusion coefficient.

Gas friction

The viscous friction is quite sufficient in convective layers, but in a radiative zone it is very small, even when taking into account the turbulent viscosity in differentially rotating layers. Another mechanism works more efficient here – gas friction. The energy drag due to the resistance force affecting the secondary is approximately

$$\dot{E}_{\text{gas}} = 4\pi\rho v_{\text{rel}}^2 R_{\text{s}}^2 v_{\text{orb}}\ . \tag{2.14}$$

2.1.2 The accretion

We treat the accretion on the secondary as Bondi-Hoyle accretion (Bondi and Hoyle 1944):

$$\dot{M}_{\text{BH}} = \pi R_{\text{acc}}^2 \rho v_{\text{rel}}\ . \tag{2.15}$$

Here we used the accretion radius $R_{\text{acc}} = 2GM_{\text{s}}/v_{\text{rel}}^2$ and ρ is the density of the CE at the position of the secondary. In the case of the secondary which is not in the corotation with the ambient envelope material (this is the definition of the CE, but might not be the case only at the very late stages, when the spiral-in is almost slowed down), the standard way to estimate the energy released due to the accretion is to take it as the released potential energy of the accreted material:

$$\dot{E}_{\text{acc}} \equiv \frac{GM_{\text{s}}\dot{M}}{R_{\text{s}}}. \tag{2.16}$$

Since the accreted material falls from the distance about the tidal Roche lobe of the secondary, for most of the spiral-in stages this approximation is good (Roche lobe radius of the secondary for stages where the accretion plays non-negligible (compared to other orbit dissipation mechanisms) role is much larger than the radius of the secondary). However, the uncertainty here is introduced by the R_s, which could be changed during the spiral-in: the accretion of high entropy material on the secondary surface causes the expansion of the secondary (see e.g. Hjellming and Taam, 1991). We also want to mention that in the case of the corotation of the secondary with the envelope and with relatively high mass accretion rates, e.g., it will lead to the fast build up of the hydrostatic structure of the secondary up to its Roche lobe and will therefore stop of the accretion. In our simulations we do not follow these features in details except of the special treatment of the secondary expansion (see 2.3.1).

The accretion luminosity calculated in the code is taken not to exceed the critical Eddington luminosity. This limit physically is determined by the condition on the density gradient in the envelope of the accreting star (if the luminosity is higher than critical, the density gradient becomes positive) and is the function of the local opacity and the mass of the star):

$$\dot{E}_{\rm edd} = \frac{4\pi c G M_{\rm s}}{\kappa} \ . \tag{2.17}$$

It implies the limitation on the accretion rate compared to the Bondi-Hoyle accretion as

$$\dot{M} = \ min[\dot{M}_{\rm BH}, \dot{M}_{\rm edd}] \ , \tag{2.18}$$

$$\dot{M}_{\rm edd} = \frac{4\pi c R_{\rm s}}{\kappa} \ . \tag{2.19}$$

Here κ is the opacity at a secondary surface and is the function of the temperature and density at the secondary's orbit. Since the accretion mass rate formula assumes that the accretion luminosity is equal to the full release of the potential energy of the accreted material, the real mass accretion rate could be higher.

A main sequence star placed inside the CE accretes almost at the Eddington limit; so we can estimate a minimal accretion time as:

$$t_{\rm acc} \sim \frac{M_{\rm s}}{\dot{M}_{\rm edd}} \ . \tag{2.20}$$

For a secondary of 5 $M_\odot$ it will be about 1300 years with an adopted average $\kappa = 0.3$ [cm^2 g^{-1}] (we want to mention that in the CE the opacity can be much higher that the electron scattering opacity used in this estimate).

2.1.3 Tidal friction

The formalism of the evolution of a close binary system due to the viscous tidal interaction of two components has started to be developed more than 30 years ago (see e.g. Kopal 1972a,b; Zahn 1975). Mainly this mechanism is applied for the synchronization and circularization in close binaries; this mechanism is very effective in the case of components with outer convective envelopes (see e.g. Press, Smarr and Wiita 1975). It therefore is one of most effective mechanisms of the orbital energy dissipation during the spiral in too, since at least the part of the convective envelope inside the binary orbit will react in the same way as the outer convective envelope in a close binary. Indeed, hydrodynamical simulations of gas flows around semi-detached binary have shown the formation of the spiral structure in these flows, analogously to the formation of tidal bulges in the convective envelope of the component of a close binary system (Sawada, Hachisu and Matsuda 1984). Also, it has been found that gravitational torques are most important mechanisms to spin up the envelope into a state of corotation with the orbital motion when the companion has spiraled to a radius of about few 10^{11}cm (Taam, Bodenheimer and Ròżycka, 2d hydrodynamical calculations); these tidal torques are important for distance of about 3 times of the orbital separation.

However, not many numerical simulations were carried out on the problem of the viscous tidal dissipation in the binary immersed into the common envelope, and no specific analytic method has been developed for this case. To introduce the orbit dissipation due to the tidal friction in our case we decided to use the prescription which has been developed for the case of tidal interactions of close binary systems.

The mass in tidal bulges can be estimated as (Savonije and Papaloizou 1985)

$$M_{\rm bul} \approx \frac{1}{16}\left(\frac{M_{\rm s}}{M_{\rm p}}D\right)^3 \rho_{\rm bul} \approx \frac{1}{64}q^2 M_{\rm s}\eta_{\rm bul}, \qquad (2.21)$$

where $\rho_{\rm bul}$ is the density of the tidal bulge, $\eta_{\rm bul} = \rho_{\rm bul}/\rho_{\rm av}$, where $\rho_{\rm av}$ is the average density of the primary inside the secondary orbit, $\eta \approx 1$, $q = M_{\rm s}/M_{\rm p}$ is the mass ratio of the binary components. As a crude estimate, the tidal bulges inside the CE will be at the same distance from the center of mass as the secondary. Then the tidal forces , for the case of a secondary inside the CE, can be

binary	$t_{\rm visc}$	$t_{\rm tid}$	$t_{\rm acc}$
20+5	300 yr	420 yr	1150 yr
20+1	230 yr	81500 yr	720 yr
15+5	285 yr	170 yr	1150 yr

Table 2.1: Characteristic time-scale for different binary systems due to different mechanisms of slowing down.

written as

$$F_{\rm tid} = \frac{G M_{\rm bul} M_{\rm s}}{R_{\rm cm}^2}, \tag{2.22}$$

(where $R_{\rm cm} = D/(1+q)$) and the corresponding orbital energy dissipation is

$$\dot{E}_{\rm tid} = F_{rmtid} v_{\rm orb} = \frac{G M_{\rm bul} M_{\rm s}}{D} \Omega (1+q)^2 \tag{2.23}$$

The time-scale of spiral-in based on the tidal dissipation can be estimated as

$$t_{\rm tid} \sim \frac{32}{q^3 (1+q)^2 \Omega \eta_{\rm bul}} \,. \tag{2.24}$$

For a binary system of $20 M_\odot$ and $5 M_\odot$ with an assumed $\eta_{\rm bul} \approx 1$ the time-scale of the orbit dissipation due to tidal friction will be of the same order as the viscous time-scale – about 500 years.

In the code instead of the rough estimate in equation 2.21 we used formula for the radial amplitude for the equilibrium tide provided in Savonije and Papaloizou 1985.

$$\zeta_r \approx \frac{1}{4} \frac{M_{\rm p}}{M_{\rm s}} \left(\frac{R_{\rm s}}{D} \right)^3 R_{\rm s} \,. \tag{2.25}$$

In table 2.1 we provide estimates for the spiral-in time-scale due to different sources. As can be seen, the viscous friction promises to be most important mechanism for the secondary's orbital decay, with tidal friction as the second most important one.

2.1.4 Kinetic energy of the CE

As mentioned before, the evolution of the angular momentum of a CE system is determined by the angular momentum loss due to a stellar wind and the exchange of angular momentum between orbital angular momentum and the spin angular momentum in the common envelope. Since the angular momentum of the secondary itself is very small, compared to the orbital angular momentum and to the primary's angular momentum, we neglect its from the consideration of total angular momentum conservation (for the spiral-in calculations). It also means that we neglect the drag of the angular momentum from the CE to the secondary due to accretion. The rate with which angular momentum is transported from the orbit to the CE, causing its spin-up, due to the CE-secondary interaction, is:

$$\dot{J}_{\rm P} = -\left(\dot{J}_{\rm orb}\right)_{\dot{M}_{\rm acc}=0} = -\frac{d}{dt}\left(\frac{M_{\rm p}M_{\rm s}}{M_{\rm p}+M_{\rm s}}D^2\Omega\right)_{\dot{M}_{\rm acc}=0} = -\frac{1}{2}\left(\frac{d\ln D}{dt}\right)_{\dot{M}_{\rm acc}=0} J_{\rm orb}. \quad (2.26)$$

and can be calculated using formula 2.2 for the orbit dissipation rate . On the other hand, in terms of the common envelope spin-up, it can be written as:

$$\dot{J}_{\rm P} = \int_{\rm CE} \dot{\omega}(r) dI_{\rm shell}(r), \quad (2.27)$$

where $dI_{\rm shell}(r)$ is the momentum of inertia of the layer between r and $r+dr$ and $\dot{\omega}(r)$ is the spin-up rate of the angular velocity of the shell. Then the rate with which the kinetic energy is deposited in the CE is:

$$\dot{E}_{\rm kin} = \int_{\rm CE} \omega(r)\dot{\omega}(r) dI_{\rm shell}(r) \ , \quad (2.28)$$

where w is the angular velocity of the shell. To order of magnitude the kinetic energy $\dot{E}_{\rm kin} \approx 0.5\ \dot{E}_{\rm orb}$. As heating the envelope energy it will reappear later.

The total heating energy, deposited in the CE due to the orbital shrinkage is:

$$\dot{E}_{\rm heat}(r) = \dot{E}_{\eta} + \dot{E}_{\rm gas} + \dot{E}_{\rm tid} + \dot{E}_{\rm acc} + \dot{E}_{\rm pot1} - \dot{E}_{\rm kin} + \dot{E}_{\rm visc}(r) \ . \quad (2.29)$$

Here $\dot{E}_{\rm pot1}$ is the change in the potential energy of the primary due to the change of the orbital separation and $\dot{E}_{\rm visc}(r)$ is the viscous friction energy source – energy, converted from the kinetic energy of the differentially rotating layers due to viscous friction. The angular velocity profile of the CE evolves not only because of the shrinking of the orbit, but also because of the diffusive transfer between differentially rotating shells. We therefore need to consider the problem of angular momentum transport in the CE as well.

2.2 Angular momentum transport in the CE

2.2.1 Equations of motion

The equations of motion are:

$$
\begin{aligned}
\frac{\partial \vec{u}}{\partial t} + (\vec{u} \cdot \nabla)\vec{u} &= -\frac{1}{\rho}\nabla P - \nabla\Phi + \frac{\nabla \cdot ||\tau||}{\rho} + \frac{1}{\rho}\vec{f}\,, && (2.30)\\
\frac{\partial \rho}{\partial t} + \nabla \cdot (\rho\vec{u}) &= 0\,, && (2.31)
\end{aligned}
$$

where Φ is the potential, P is the pressure and $\vec{u}$ is the velocity of a particle in the CE, $\vec{f}$ denotes some other general forces causing the acceleration and τ is the viscous stress tensor (Landau and Lifshitz 1959), which, without the bulk viscosity, is

$$
\tau_{ij} = \eta_{ij}\left(\frac{\partial u_i}{\partial x_j} + \frac{\partial u_j}{\partial x_i} - \frac{2}{3}\delta_{ij}\nabla \cdot \vec{u}\right)\,. \tag{2.32}
$$

This tensor produces general viscous forces, which affect on the redistribution of the angular momentum.

In conservative form equations (2.30) (2.31) can be rewritten as:

$$
\frac{\partial \rho\vec{u}}{\partial t} + \vec{u}\nabla \cdot (\rho\vec{u}) + \rho(\vec{u} \cdot \nabla)\vec{u} = -\nabla P - \rho\nabla\Phi + \nabla \cdot ||\tau|| + \vec{f}. \tag{2.33}
$$

2.2.2 The angular momentum transport equation

Our primary goal when solving the angular momentum transport problem is not to obtain the precise velocity pattern itself in all 3 dimensions, but rather to determine the averaged distribution of the energy source inside the common envelope due to this velocity pattern, which afterwards can be used in a consistent way in the stellar evolution code. Since the code which calculates the structure of the star is one-dimensional, we can use only the one-dimensional energy distribution. Therefore we want to consider a reasonable simplification for the angular momentum transport equation. Deviations from the symmetry are changes of the velocity pattern due to tidal interactions of the envelope with the secondary and changes of the velocity pattern due to the angular velocity evolution because of the convective angular momentum transport. The first mechanism causes deviations in the $\varphi-$ coordinate as well as in the $\vartheta-$ coordinate, while the effect of convection on rotation velocity pattern works only in the $\vartheta-$ coordinate.

First, let us consider the asymmetry in the $\varphi-$coordinate. The deviation from the symmetry arises from the gravity produced by the rotating binary, which results in the creation of tidal bulges. As a result of interactions, the secondary exchanges angular momentum with the CE matter, shrinking its orbit and spinning up the surrounding matter. The spin-up of the CE matter also depends on the local viscosity. For a convective region the characteristic time-scale of the turnover of a turbulent eddy $t_{\rm c} = l/v_{\rm c}$ in the convective zone could be more than a few orbital periods. The evolution of the angular velocity evolves on the viscous time scale; therefore the effect of the rotating binary on the evolution of the angular velocity physically will be averaged over a few periods. To consider the influence of the rotating binary averaged over one period, one needs to consider the net acceleration for the φ-component of the velocity due to the angular momentum source in equation (2.26). The deviation in the $\vartheta-$ coordinate for a case of a tidally distorted body inside the convective envelope has been discussed by Meyer and Meyer-Hofmeister (1979). Comparing the efficiency of the gravitational acceleration and the centrifugal forces, the ratio of which is proportional to r^{-2n+3} (n here is the power law index for the angular velocity decrement with radius $\omega(r) = \Omega\left(\frac{r}{D}\right)^{-n}$, $n \approx 3$), they claimed that the deviation from spherical symmetry due to the gravity can be neglected, when considering its affect on the inner structure of the envelope.

Heger and Langer (1998, HL) developed a more sophisticated treatment of angular momentum transport inside a convective envelope of a RSG. They also discussed the problem of the latitude variations for the angular momentum transport in convective zones of RSG and noted that it is reasonable to use the approximation which does not take this into account these variations.

In our case, apart from the simplicity of the equations, the approximation of spherically symmetry provides a more consistent way to apply the energy source from the differential rotation to the 1d stellar model. In real life, the angular velocity profile in the convective zone could, of course, be different. In a number of numerical simulations (see Robinson and Chan 2001 for review), it has been found that the angular velocity distribution has cylindrical iso-contours, but these simulations are also not quite consistent with real life: helioseismology observations of the angular velocity distribution in the solar convection zone (SCZ) have shown that the rotation rate is constant on radial lines (i.e. has cone-like structure, Gilman 2000, Scherrer 1995). Hence, we decided to consider the spherically symmetric case as primary choice, and also performed for test purposes calculations with cylindrical symmetry for the rotation law.

In a spherical coordinate system (r, ϑ, φ), where r is the radial coordinate, φ is the azimuthal angle and ϑ is the polar angle associated with the rotation axe, the $\varphi-$component of the momentum conservation equation (2.33) can be written in the form (for full derivation see Appendix A) :

$$\frac{\partial}{\partial t}\left(\rho r^4 \Omega\right) + \frac{\partial}{\partial r}\left(\rho r^4 u_r \Omega\right) = \frac{\partial}{\partial r}\left(r^4 \eta_{\varphi r} \frac{\partial \Omega}{\partial r}\right) + \frac{3}{8\pi}\frac{\partial j_s}{\partial t} \tag{2.34}$$

and in a cylindrical coordinate system (r, φ, z)

$$\frac{\partial}{\partial t}\left(\rho r^3 \Omega\right) + \frac{\partial}{\partial r}\left(\rho r^3 u_r \Omega\right) = \frac{\partial}{\partial r}\left(r^3 \eta_{\varphi r} \frac{\partial \Omega}{\partial r}\right) + \frac{1}{2\pi}\frac{\partial j}{\partial t} \,. \tag{2.35}$$

The source of the angular momentum $\frac{\partial j_s}{\partial t}$ can be found from Eq. 2.26, where the viscosity model is taken from section 2.1.1 and the spatial density distribution is obtained from a stellar model produced by the evolutionary code. For the radial velocity we use the speed of envelope expansion from the evolutionary code, which has been upgraded to take into account the acceleration term. For numerical reasons it is more convenient to solve the equation of angular momentum transport (2.34) on a logarithmic scale $x = \ln r$. Then our equations have the following form (from here we drop index of η since it is the only viscosity coefficient now):

$$\begin{aligned}\frac{\partial \Omega}{\partial t} - \frac{\eta}{\rho r^2}\frac{\partial^2 \Omega}{\partial x^2} \quad &+ \quad \frac{\partial \Omega}{\partial x}\left(\frac{u_r}{r} - \frac{3\eta}{\rho r^2} - \frac{1}{\rho r^2}\frac{\partial \eta}{\partial x}\right) \\ &+ \quad \Omega\left(\frac{4u_r}{r} + \frac{\partial \ln\rho}{\partial x}\frac{u_r}{r} + \frac{1}{r}\frac{\partial u_r}{\partial x} + \frac{\partial \ln \rho}{\partial t}\right) = \frac{3}{8\pi}\frac{1}{\rho r^4}\frac{\partial j}{\partial t}\end{aligned} \tag{2.36}$$

in a spherical coordinate system and

$$\frac{\partial\Omega}{\partial t} - \frac{\eta}{\rho r^2}\frac{\partial^2\Omega}{\partial x^2} + \frac{\partial\Omega}{\partial x}\left(\frac{u_r}{r} - \frac{2\eta}{\rho r^2} - \frac{1}{\rho r^2}\frac{\partial\eta}{\partial x}\right) + \Omega\left(\frac{3u_r}{r} + \frac{\partial\ln\rho}{\partial x}\frac{u_r}{r} + \frac{1}{r}\frac{\partial u_r}{\partial x} + \frac{\partial\ln\rho}{\partial t}\right) = \frac{1}{2\pi}\frac{1}{\rho r^4}\frac{\partial j}{\partial t} \qquad (2.37)$$

in a cylindrical system of coordinates. Since the viscosity coefficient η in a radiative zone (in the presence of the gradient of angular velocity) depends on the derivative of the angular velocity (2.8), equations became non-linear in Ω.

2.2.3 Differential rotation as energy source

The kinetic energy of the differentially rotating shells is dissipated due to viscous friction and provides a heating source. Since the angular momentum is transported from inner shells to outer regions, this energy is not necessarily deposited in the same place where the angular momentum has initially been deposited.

The amount of the dissipated kinetic energy in a shell due to the viscous friction is (Landau and Lifshitz 1959) :

$$\dot{E}_{\rm kin} = \int_{\rm shell} \tau_{ij}\left(\frac{\partial u_i}{\partial x_j} + \frac{\partial u_j}{\partial x_i} - \frac{2}{3}\delta_{ij}\nabla\cdot\vec{u}\right) dV = \int_{\rm shell} \eta r^2 \sin^2\vartheta \left(\frac{\partial\Omega}{\partial r}\right)^2 dV\ . \qquad (2.38)$$

Then the rate of energy dissipation for the case of spherical symmetry can be written as

$$\varepsilon_\eta = \frac{\dot{E}_{\rm kin}}{\int_{\rm shell} dm} = \frac{1}{3}\frac{\eta}{\rho}\left(\frac{\partial\Omega}{\partial r}\right)^2 r^2 \quad [erg\cdot g^{-1}sec^{-1}]\ . \qquad (2.39)$$

(this rate of energy dissipation is different from MMH by the factor $2/3$).

2.3 Numerical simulations

2.3.1 The method and model set up

The spiral-in was modelled using a Henyey-based evolutionary code (see Podsiadlowski and Rappaport 2000; also see Appendix C). One of the modification to the code was the inclusion of hydrodynamic terms in the equations of the stellar structure. The artificial viscous pressure Q, which require to treat shocks, has been taken in the following prescription:

$$
\begin{aligned}
Q &= c_0\rho l^2\left[\frac{1}{r^2}\frac{\partial}{\partial r}(r^2v_r^2)\right]^2 , & \frac{\partial v_r}{\partial r} < 0 \\
Q &= 0\,, & \frac{\partial v}{\partial r} > 0\,,
\end{aligned}
\tag{2.40}
$$

where c_0 is a dimensionless parameter of order unity (we use 1), l is the spacing between mesh points, and v_r is the radial velocity.

The angular momentum transport equation is solved using an iterative implicit finite difference method. In our implementation of the method each derivative in the equation of angular momentum transport is obtained using a 5 points representation, i.e. for a k-th derivative of the variable y at the point j it can be written as

$$
\frac{d^k y_j}{dx^k} = a_{1k}y_{j-2} + a_{2k}y_{j-1} + a_{3k}y_j + a_{4k}y_{j+1} + a_{5k}y_{j+2}\,. \tag{2.41}
$$

The resulting band matrix

$$
\begin{matrix}
X & X & X & X & X & 0 & 0 & ... & 0 & 0 & 0 & 0 & 0 & 0 \\
X & X & X & X & X & 0 & 0 & ... & 0 & 0 & 0 & 0 & 0 & 0 \\
0 & X & X & X & X & X & 0 & ... & 0 & 0 & 0 & 0 & 0 & 0 \\
0 & 0 & X & X & X & X & X & ... & 0 & 0 & 0 & 0 & 0 & 0 \\
. & . & . & . & . & . & . & ... & . & . & . & . & . & . \\
0 & 0 & 0 & 0 & 0 & 0 & 0 & ... & X & X & X & X & X & O \\
0 & 0 & 0 & 0 & 0 & 0 & 0 & ... & 0 & X & X & X & X & X \\
0 & 0 & 0 & 0 & 0 & 0 & 0 & ... & 0 & X & X & X & X & X
\end{matrix}
$$

is solved by using a modified Gauss method. This numerical method has previously been used for calculations of the evolution of the angular velocity profile in massive main sequences stars (Ivanova, 1998; Denissenkov, Ivanova and Weiss, 1999). The method has been verified for stationary solution (i.e. no evolution of the angular velocity with time) by comparing these with numerical results using the code given by Urpin (Urpin, Shalybkov and Spruit, 1996), which have shown a perfect match.

Implicit surface and inner boundary conditions guarantee angular momentum conservation (to the same order of numerical precision as is provided by the solution of the angular velocity profile). Furthermore, in order to reduce a numerical noise, we insisted that the viscosity can not change faster than the turbulent eddy turnover time. When energy source is placed inside the common envelope, this may create a zone where radiative and adiabatic gradients are very close to each other; numerical noise then occasionally produce a radiative zone for one time-step, thereby affecting the viscosity. The time derivative of the viscosity in this case is very high. But from a physical point of view convective eddies should not disappear faster than the order of its turnover time t_c).

As initial condition we use the combination of uniform rotation for the inner region and for the outer region we use either constant angular velocity or a constant specific angular momentum (where the specific angular momentum is taken from the top of the uniformly rotating region). For the later case we also assume as an additional restriction that at least for initially the angular velocity does not increase with radius. Since with this description the inner region can be taken as large as the whole star, it includes also the case of completely uniform rotation (i.e. case of the primary co-rotating with the binary).

We use the mass loss rates from the surface in Reimer's formalism with the modification for rotationally induced increase in the mass loss rate as the star approaches $\Omega-$limit from Langer (1997):

$$\frac{\dot{M}}{\dot{M}(\Omega=0)} = \left(\frac{1}{1-w}\right)^{0.43} , \tag{2.42}$$

where

$$w = \Omega/\Omega_c \ , \quad \Omega_c = \sqrt{\frac{Gm}{r^3}}(1-\Gamma) \ , \ \ \Gamma = \frac{\kappa L}{4\pi c G M} \ .$$

The equation for angular momentum transport as in Eq. 2.36 works well in stages when no shock arises. In the case of the secondary inside the CE, a large gradient in u_φ occurs near the secondary's position. The finite elements method is not the best method to resolve shocks, but the problem can be avoided by solving instead of Eq. 2.36 two equations, one the conservation of the specific angular momentum during the expansion or contraction of the star, and the other solves the diffusion of the angular momentum due to viscosity.

The common envelope evolution has been calculated taking into account the following:

– The structure of the primary star is calculated with the gravitational potential of the secondary[1].

– The orbital separation of the binary D is found from the condition of the total angular momentum conservation. At the start of each step we update D using the new structure of the primary (in particular, the updated value of the mass of the primary within the secondary's orbit), after that we find the rates of the orbital decay due to friction forces and due to the accretion onto the secondary.

– For each time step we update the angular velocity profile, solving the diffusion equation for its transport with the angular momentum source due to tidal and viscous (gas) friction.

– The additional energy source for the primary – the heating energy – is calculated as in equation 2.29.

– Apart from the mass loss from the primary's surface, we keep the total mass of the system conserved: we take out the mass accreted onto the secondary's from the primary in the region close to the secondary orbit. The exception is the stage when the secondary is still outside of the primary's envelope: the mass accretion is still taken there at the limiting regime, but mass the loss rate from the primary does not match this rate.

– As the end of the spiral-in we take the moment when the secondary would start to loss mass if it would have an initial mass and an initial radius (in other words, for determination of this point we neglect the effect of the accretion on the secondary).

The response of a MS secondary within a CE has previously been considered in the work by Hjellming and Taam (1991). As theirs calculations have shown, the secondary, even after accreting only 5% of its mass of the high entropy CE material, expands very dramatically (by as much as a factor of 100). The radius of the secondary is the important parameter for such drag forces as viscous and gas friction. We included the change of the secondary radius as one of the parameters in studying this problem (the results of the calculations of Hjellming and Taam have shown that a radius is roughly a linear function of radius, where the maximum radius corresponds to the moment

[1]Here we mean that all the equations for the stellar structure which include gravity acceleration takes into account the presence of the tidal mass (the secondary) at a certain (updated with time) distance from the center of the primary

soon after the secondary enters into the CE and where the minimum radius is of order the initial one near the hot and dense inner zone; the maximum secondary expansion depends on the envelope entropy).

We calculated a number of models varying the prescriptions for the initial conditions of the angular velocity distribution, the efficiency of tidal and viscous friction, the coordinate system, e.t.c. The standard model A refers to the evolution of a CE system consisting of $20M_\odot$ and $1M_\odot$, which has been calculated with the standard prescription for viscosity and tidal friction. We took the models of an evolved $20M_\odot$ star, having low metallicity Z=0.01, at the age of $9.15 \cdot 10^6$ years. The star has 2 nuclear shell-sources – hydrogen and helium burning shell – and a CO core. Initially the star is considered to be in complete corotation with the secondary, which is placed at the orbit $D = 7 \cdot 10^{13}$cm (the secondary is just outside the primary envelope, which initially has a radius $R_\mathrm{p} = 6.3 \cdot 10^{13}$cm). The models have the following modifications:

B — modified viscosity prescription: viscosity is reduced as $\alpha_\nu = 0.1$

C — modified efficiency of tidal interaction: $k_\mathrm{tid} = 0.1$

$D - F$ — modified initial conditions for the angular velocity distribution:

$D \rightarrow \Omega_0 = 0.1\Omega_\mathrm{orb}$, uniform rotation;

$E \rightarrow \Omega_0 = 0.0001\Omega_\mathrm{orb}$, uniform rotation;

$F \rightarrow$ fast rotating core of $R_\mathrm{core} = 0.001R_\mathrm{p}$ has $\Omega_\mathrm{core} = 1000\Omega_\mathrm{orb}$ and the rest of the star has constant specific angular momentum (with the restriction of no radial increase of the angular velocity)

G — calculated using the hydrostatic version of the code

H — the energy source due to viscous friction is not calculated as having the spatial distribution over the CE, but placed nearby the secondary orbit

I — cylindrical symmetry for the angular velocity

K — the radius of the secondary is taken to be a function of the distance (in the parameterized model of the secondary's response to the accretion of material from the primary). The

Model	$t_{\text{sp-in}}$	M_{s}	M_{p}	$\lg D$
A	1008	1.130	19.151	11.489
B	1510	1.217	19.209	11.416
C	2104	1.192	19.337	11.780
D	729	1.117	19.913	11.331
E	692	1.104	19.920	11.413
F	715	1.119	19.904	11.391
G	1036	1.143	18.621	11.319
H	992	1.132	19.254	11.382
I	975	1.130	19.614	11.392
K	348	1.069	19.757	11.338

Table 2.2: Time of the spiral-in in years, the final mass of the secondary and of the primary in M $_\odot$, and the final orbital separation for different models for the CE system initially consists of stars of $20M_\odot$ and $1M_\odot$.

maximum expansion is taken be as much as 10 times of the undisturbed secondary radius

The results of the calculations, such as the time of the spiral-in and the mass of the secondary, of the primary and the orbit separation at the moment of the end of the spiral-in are presented in the Table. 2.2 and discussed in detail below. Since the mass loss rate from the primary when the secondary is still outside the primary and the mass accretion rate are not the same, the secondary artificially accumulates about $0.03M_\odot$ and the total mass of the CE system changes slightly. The decrease of the total mass is due to the mass loss.

Before we go in more details with results of the calculations, we shortly outline here phases of the CE evolution, which can be later distinguished in calculations (for more details see the discussion in Introduction and the discussion in further sections; also see Podsiadlowski 2000):

- *The initial phase:* the loss of co-rotation.
- *The plunge-in phase:* the rapid spiral-in, the envelope expansion (may lead to the envelope ejection).
- *The slow spiral-in phase:* establishing of the self-regulating regime and of the co-rotation in the inner zone, surrounded by the differentially rotating envelope.
- *The end of the slow spiral-in:* the merge phase or the break down of the self-regulating

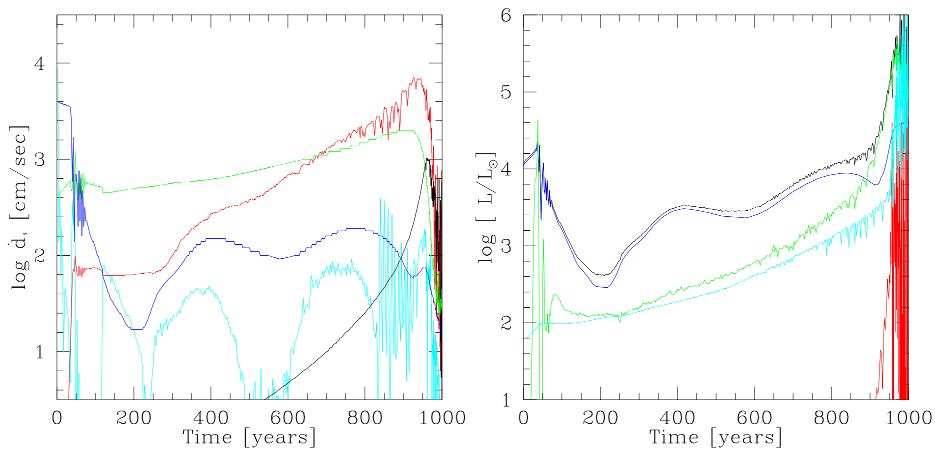

Figure 2.1: Rates of the decay of the orbital separation and energy sources. Left panel: $\log|\dot{d}|$, rate of orbit dissipation due to the: blue – accretion, red - viscosity, black – gas, green – tidal, cyan – envelope expansion/contraction. Right panel: $\log|L/L_\odot|$, luminosity sources: black – total additional, blue – accretion, green – rate of the orbital energy dissipation excluding the part placed as kinetic energy, cyan – the rate with which the kinetic energy is transferred to the CE, red – heating due to the differential rotation of the CE.

regime and the second envelope expansion phase (leading to the envelope ejection)

2.3.2 A CE system of $20 + 1\mathrm{M}_\odot$: the standard model (model A)

In this case a CE forms because of a dynamically unstable mass transfer event. This problem has to be treated as three-dimensional and has been, e.g., studied in detail using by SPH calculations (Rasio and Livio, 1995). As the code we use is one-dimensional, it can not treat the initial phase correctly. Nevertheless, using angular momentum conservation due to the mass loss from primary and the mass accretion onto the secondary and also applying the model of tidal friction and for the heating of the primary envelope due to the secondary's accretion luminosity, our calculations can approximately follow the evolution of the orbital separation together with the primary's expansion (see the plot for the radial velocity in Fig. 2.2). The main source for the orbital decay is the mass accretion, the second most efficient is tidal friction. The accreting secondary heats up the primary envelope and drives its expansion.

Once the secondary orbits at the outer layers of the primary's envelope, viscous friction starts to act. On the other hand, the orbital decay due to the secondary's accretion slows down very dramatically, since the opacity in this part of the envelope is very high (see Fig. 2.1). Tidal

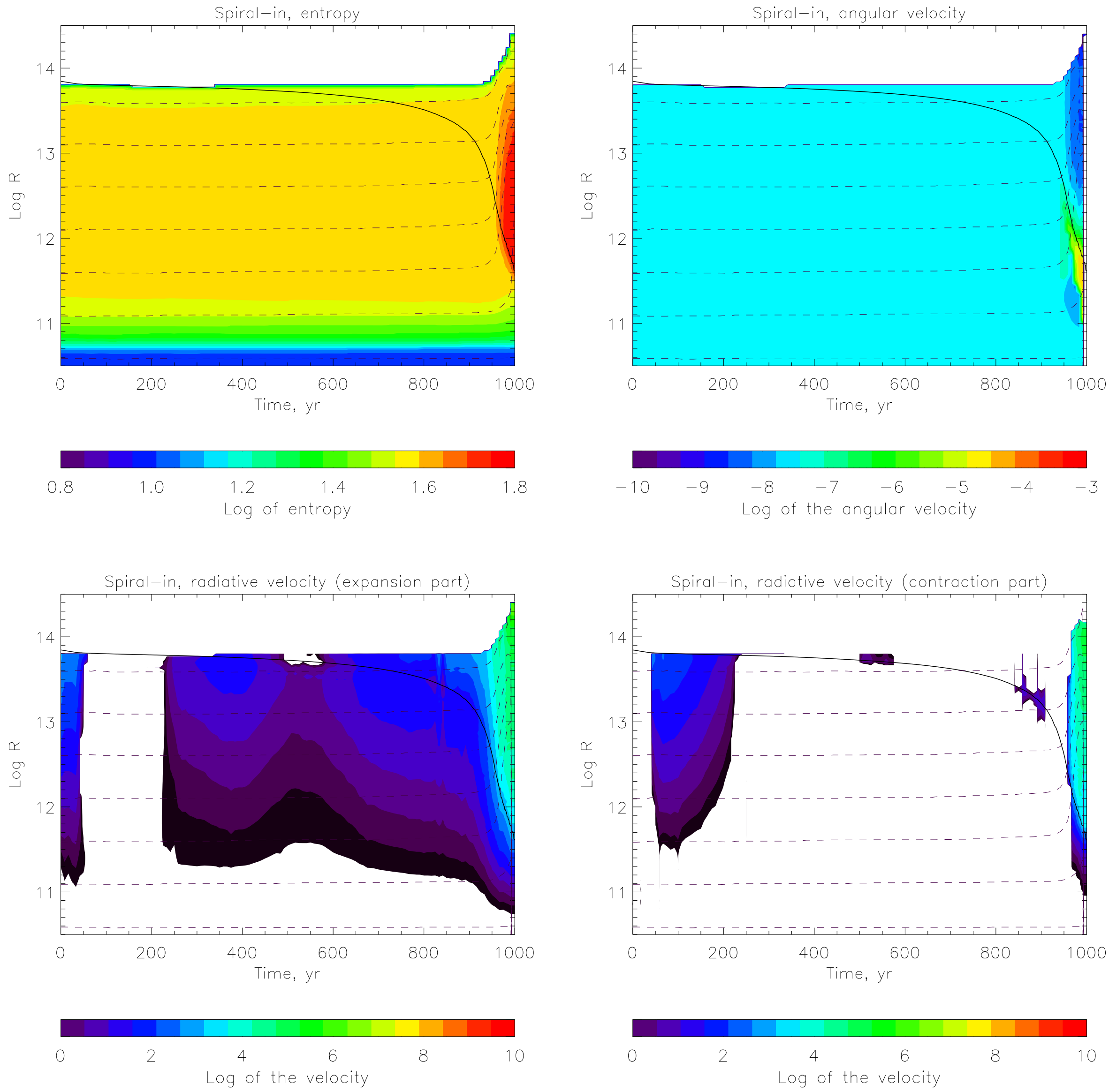

Figure 2.2: The common envelope system consists of 20 and 1 $M_\odot$ stars : evolution of entropy, angular velocity $\Omega(r)$ and radial velocity u_r (expansion and contraction). Mass lines correspond to $M = 16.7, 9.61, 7.77, 7.315, 7.168, 7.101, 6.83$ (from the top).

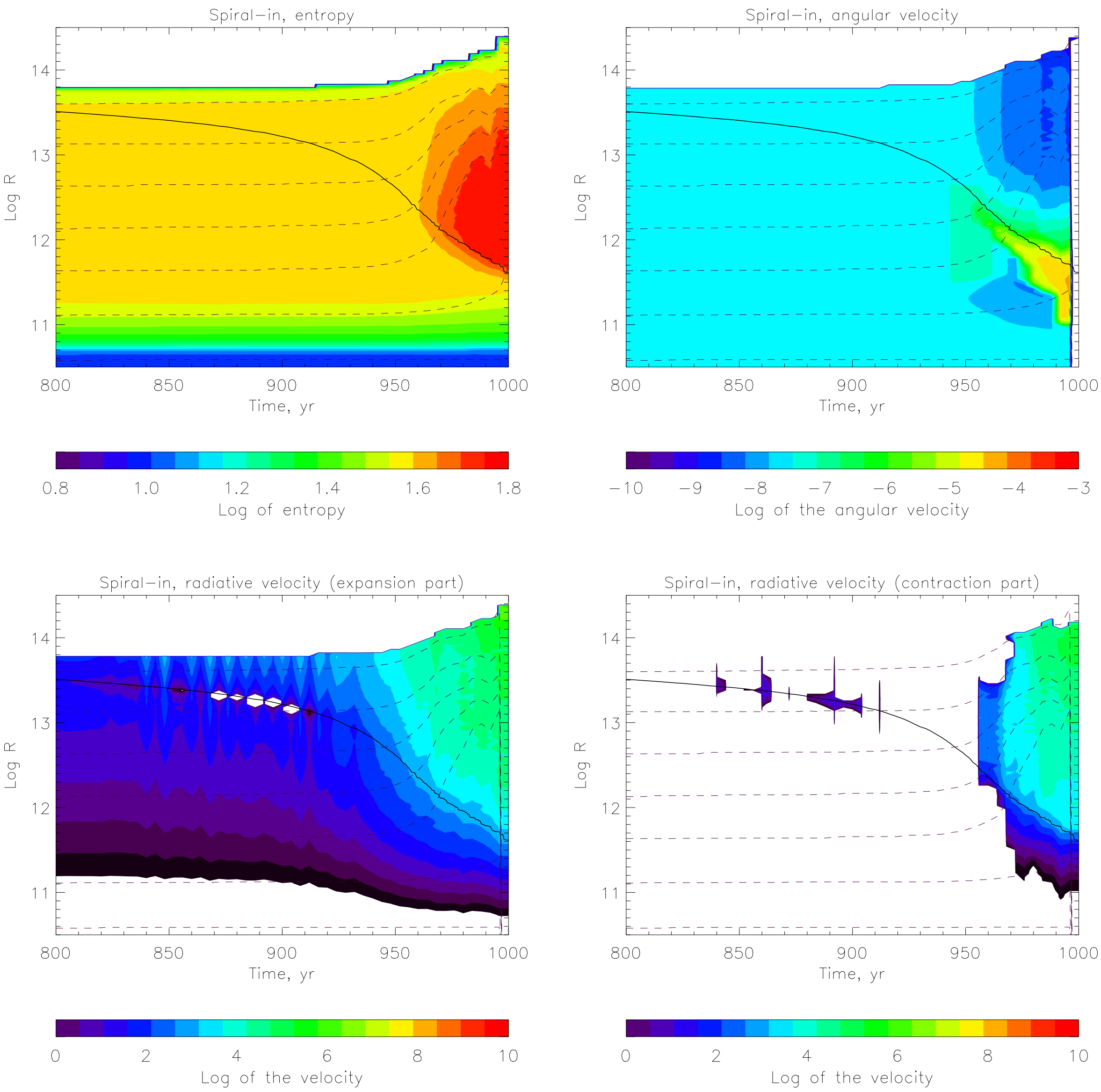

Figure 2.3: Expanded view of Fig. 2.2 for the end of the spiral-in.

friction remains roughly constant, to order of magnitude, for almost all of the spiral-in. Since the accretion luminosity decreases dramatically, and the energy source due to viscous friction has not yet developed, the total luminosity, injected into the envelope decreases by 2 orders of the magnitude. As a result of this decrease and also due to the additional gravitating body within, the envelope stops expanding and start to slowly contract. This contraction phase continues till the moment when the total rate of the energy injected into the primary envelope becomes larger than $\sim 1000 L_{\odot}$. As the envelope contracts and the mass of the primary within the secondary's orbit increases, the orbit separation expands of the orbit[1] (see cyan line at the Fig. 2.1). It can be seen from Fig. 2.1 and Fig.2.2, that the second contraction phase occurs at the moment when the secondary enters the region of high opacity and $L_{\rm acc}$ has a local minimum. Soon after the second contraction phase, the role of the energy source due to viscous friction increases. Viscous friction also becomes the dominant mechanism for the orbit dissipation. At the latest stage of the spiral-in the most effective mechanism of the orbit dissipation is a gas friction and the most effective energy source are the orbital energy dissipation and the viscous friction due to the differential rotation. The latest stages are shown in more detail in Fig. 2.3. During this plunge-in stage, the star is dynamically unstable and pulsates with a period about 0.4 year.

As this calculation has shown, at the end of the spiral-in the zone of the primary within the secondary orbit is not in the corotation with the binary. Also, for this system there is no stage of a slow spiral-in stage – the deposited orbital energy is not high enough to cause significant expansion of the zone inside the secondary orbit, and gas friction works very effectively till the end of the spiral-in (it is by about one order of magnitude higher than the rate of the orbit dissipation due to the tides and the accretion).

2.3.3 Deviations from the standard model

The effect of varying of the viscous and the tidal efficiency – models B and C

The effects of the decreasing of the viscous and the tidal efficiencies are consistent with the predicted behavior: the rate of orbital dissipation decreases and the time of spiral-in is longer. As a result, the secondary accretes more mass.

[1]It can be seen from the Eq. 2.4 with used the $\dot{M}_{\rm S} = 0$ and using that at this separation $2M_{\rm S} < M_{\rm P}$.

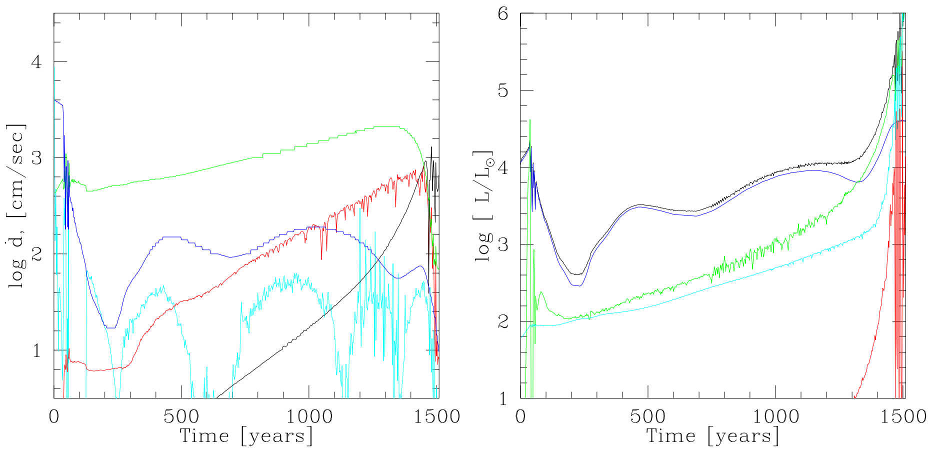

Figure 2.4: The same as Fig. 2.1, but for model B.

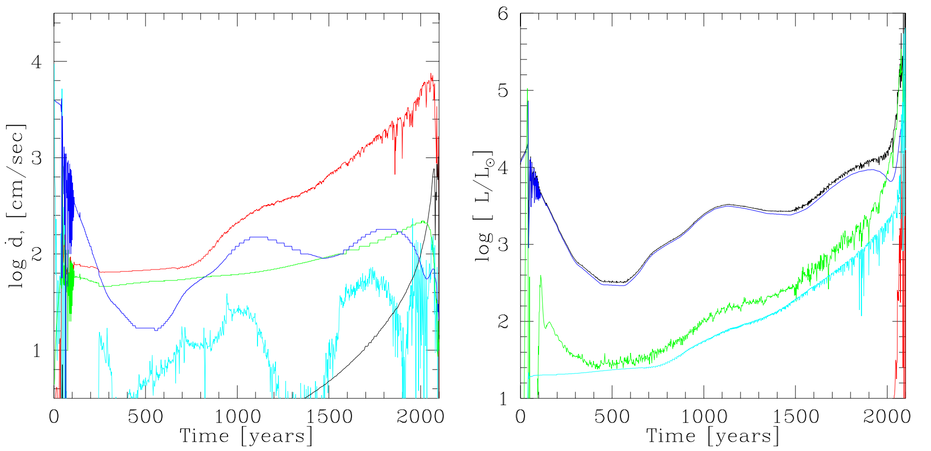

Figure 2.5: The same as Fig. 2.1, but for model C.

As the viscosity is decreased, the time-scale for the diffusion of angular momentum is increased by the same order. But the total time for the spiral-in increases only twice, since other drag forces continue to be effective. Therefore during the spiral-in less angular momentum will be transported to the surface, and the surface angular velocity will be smaller (comparison of the numerical results shows that the difference is about a factor of 2 in the surface angular velocity for models A and B). Another circumstance which affects the total angular momentum in the envelope and the surface angular velocity in particular is the following: as the spiral-in time is longer, the secondary can accrete more mass. Due to the conservation of the total angular momentum of the CE (apart from the angular momentum loss in the stellar wind), the amount of the angular momentum transferred into the CE will be smaller compared to the model A. This circumstance is effective for both cases, B and C. Corresponding to the adopted mass loss model, a smaller surface angular velocity causes a smaller surface mass loss rate, and therefore the mass of the primary at the end of the spiral-in is larger.

Although the time of the spiral-in is longer for the model with changed tidal efficiency (model C), the accreted mass is smaller. The main reason for this is that in this case the companion spends relatively more time within the zone with larger opacity, where the accretion rate is smaller (see Fig. 2.4 and Fig. 2.5).

The effect of initial conditions for the angular velocity distribution – models D, E and F

There are two main outcomes from a change of the initial angular velocity profile. First, it changes the initial total angular momentum of the system. To spin up the surface layer to the same surface angular velocity as in model A will therefore require more injection of angular momentum, independent from its source. The transferred orbital angular momentum cannot spin-up the outer layers of the envelope significantly and as a result the mass loss rate during the spiral-in is much smaller. The second outcome is that the relative velocity of the secondary to the envelope matter is increased. This increases such drag forces as the viscous and the gas friction. So the time of the spiral-in is decreased for all these models compared to model A. An interesting effect occurs for the model with the initially fast rotating core – as the spin-up of the inner zone is easier for this model, this is the only model for a CE system of $20 + 1 M_\odot$ which achieves corotation at the end of

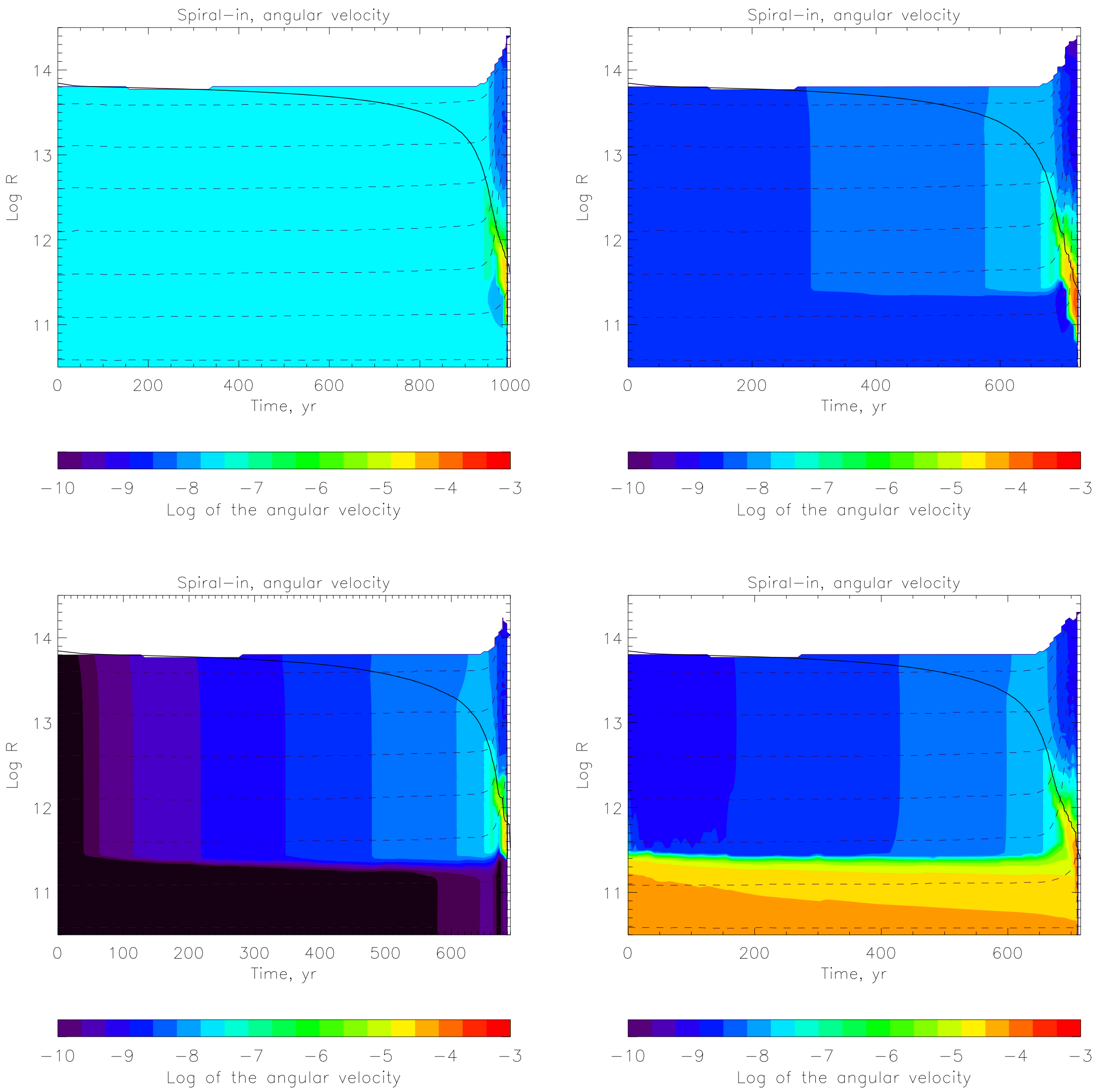

Figure 2.6: Angular velocities for models A, D, E and F. Mass lines as in Fig. 2.2.

the spiral-in (Fig. 2.6).

All the other models did not show up sufficient differences in their characteristic behavior, except for model K. The main effect here is that viscous and gas friction are more effective during the long phase of the fall and so the spiral-in ends up very fast. Hence secondary does not accumulate much mass and mass loss from the primary is small.

2.3.4 A CE system of $20\mathrm{M}_\odot$ and $5\mathrm{M}_\odot$.

The evolution of a CE system with a more massive secondary has principal differences from the previously discussed case. First of all, unlike the fast plunge-in of the low mass secondary, the more massive component deposits enough energy into the envelope to expand it and as a result to slowing down the spiral-in. Also, the dissipation of the orbital energy due to viscous and gas friction forces is relatively smaller than in the case of the CE $20 + 1M_\odot$ system. The second principal difference is that the zone within the secondary orbit achieves co-rotation with the binary at the end of the spiral-in. At the end of the spiral-in the primary has lost 6.7 $M_\odot$. It was estimated in section 2.1.2 that the viscous time for the binary containing of a more massive secondary is longer than for a system with low mass secondary. The calculation shows that viscosity does not affect the result much – model B is not strongly different from model A : corresponding spiral-in times are 613 yr and 603 yr. Again, as with a smaller viscosity less angular momentum could be transferred to the surface, the mass loss rate is smaller for model B – the primary loses about 5.4 $M_\odot$.

2.3.5 A CE system of a low mass red giant and a white dwarf.

Being simple, but relatively fast (compared to real hydro simulations), the described method can also be used for exploratory studies of CE systems in general. In particular, an interesting test site is a binary system consisting initially of a low mass red-giant and a low mass WD. Indeed, these systems provide a well defined channel for the formation of a short period binary with an OB subdwarf and a white dwarf as a product of the spiral-in and therefore provide a good opportunity to test the criterion for envelope ejection. It has been suggested that the common-envelope can be ejected in two different ways: one is at the end of the initial plunge-in phase (if it becomes dynamical), and one after a phase of self-regulated spiral-in when the compact star penetrates into the initially

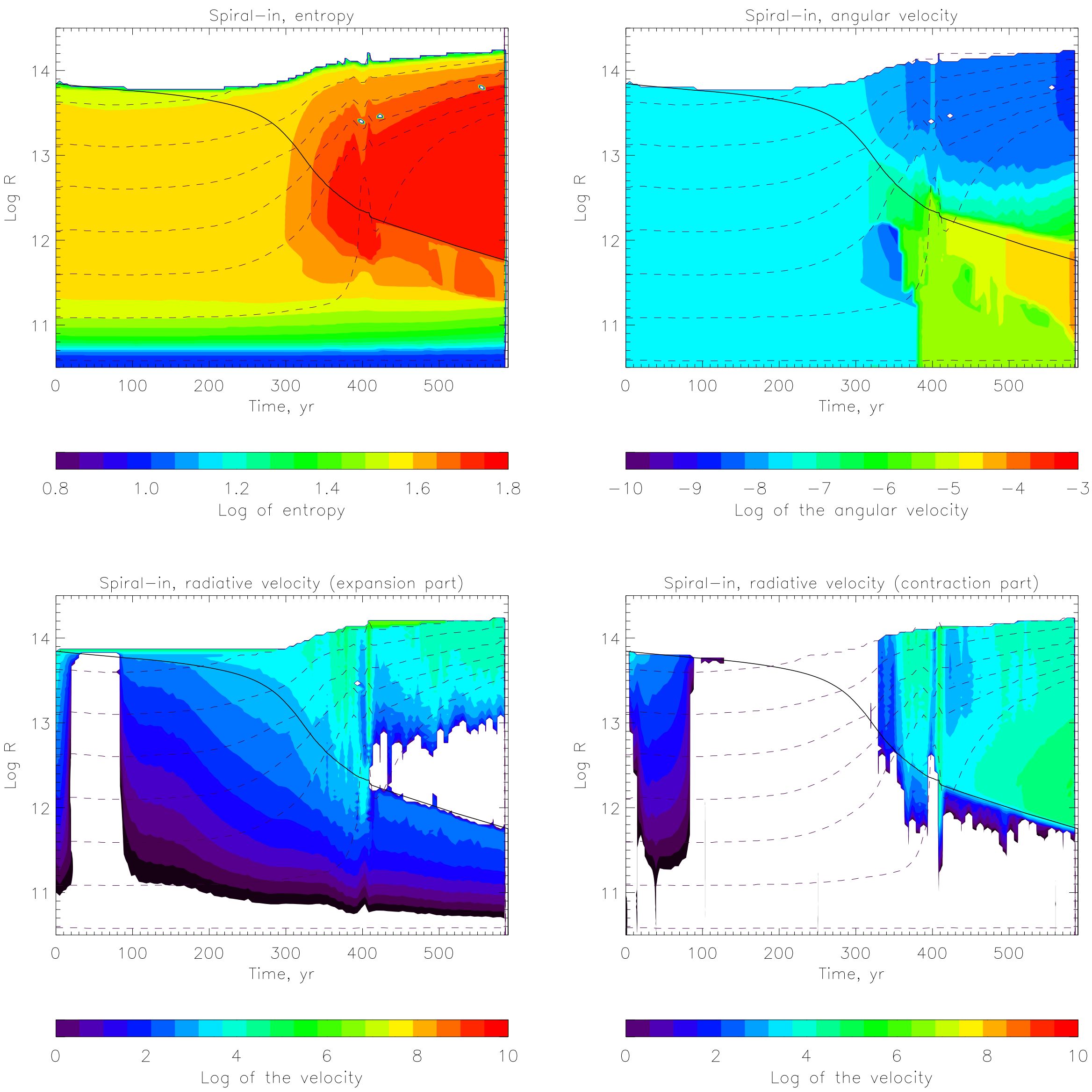

Figure 2.7: Common envelope system of 20 and 5 $M_\odot$ stars: entropy, $\Omega(r)$ and u_r evolution. Mass lines correspond to $M = 16.7, 9.61, 7.77, 7.315, 7.168, 7.101, 6.83$ (from the top).

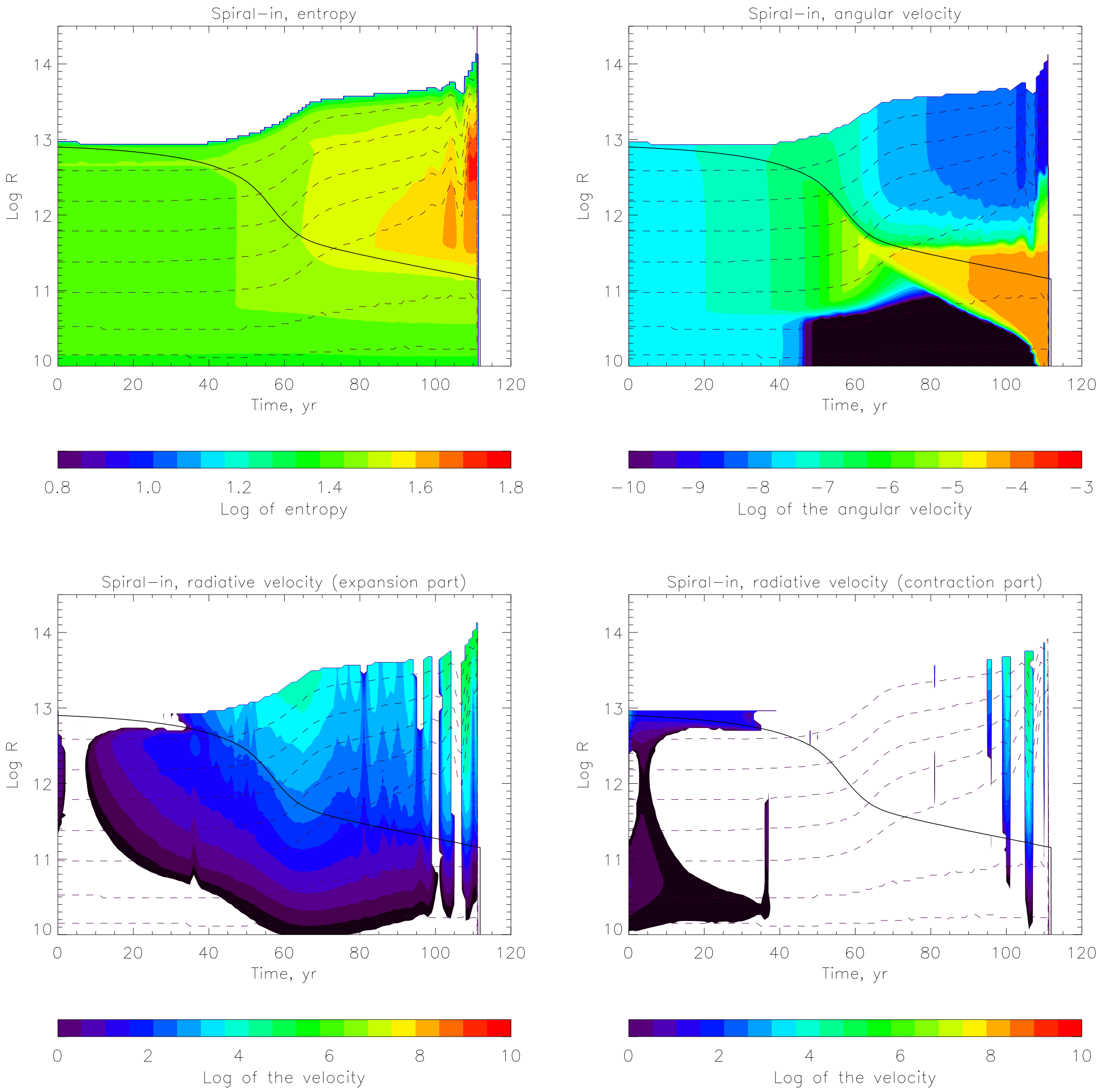

Figure 2.8: Common envelope system of a 1.6 $M_\odot$ red giant and a 0.3 $M_\odot$ WD. Mass lines are at the $1.113, 0.6054, 0.4923, 0.4697, 0.4644, 0.4628, 0.4622 M_\odot$.

radiative layer where the self-regulation process always breaks down (delayed dynamical ejection; Podsiadlowski 2000).

Of course, in real life the situation should be somewhat different from what can be predicted by our approach: e.g., 3d hydrodynamical simulations show that in some cases the mass outflow is not spherically symmetric, with the maximum outflow in the equatorial plane and with some inflow from the poles (Sandquist, Taam and Burkert 2000). For an evolved primary this happens for systems with a mass ratio more that about 0.35; but for a smaller mass ratio the picture is more spherically symmetric.

We performed a number of simulations for a binary consisting of a red-giant of 1.6 $M_{\odot}$ and a WD of 0.3 $M_{\odot}$. We were looking at the final separation at the moment when the envelope ejection starts, varying such initial parameters as viscosity, tidal efficiency and the initial angular velocity profile in the primary envelope. The only difference with the previous simulations was that here for the mass loss rates we did not use the enhancing due to the angular velocity - it gives a very unstable start for the calculations: the upper, low density layers, gain angular momentum too fast, the mass loss rate increased and due to the mass loss the star starts to expand very fast. This is a general property of convective envelopes investigated by Hjellming (1988), and since we can not be absolutely sure about the correctness of the angular velocity distribution at the outer layers at the start in this particular case, we assumed that it could be an artificially triggered effect.

All the results show that normally such a system survives the phase of the initial plunge-in, and after that during the slow spiral-in stage (see Fig. 2.8), the orbit shrinks at a constant rate. As it turns out, for these systems the final results (i.e. the final separation, not the spiral-in time) does not depend much on the initial parameters. They have a similar behavior, apart from the fact that since the tidal parameter leads to different luminosity from the orbital energy at the stage after the initial plunge-in, and this luminosity slowly increases, the envelope normally starts to be ejected after this luminosity achieved a certain value. At this point the envelope starts to eject, and the smaller the tidal efficiency is, the smaller the binary separation at this moment. Also, we can confirm that the envelope ejection starts when the secondary already came into the layers which were initially (at the start of the spiral-in) radiative (see Tabl. 2.3).

The final separation is normally more than $\log D = 11$, although it is known from obser-

$k_{\rm tid}$	α_ν	$\log D_{\rm fin}$	$\log R_{\rm rad}$
1	1	11.15	12.23
1	0.1	11.15	12.25
2	1	11.35	12.15
0.3	1	11.05	12.16

Table 2.3: Common envelope system of 1.6 $M_\odot$ red giant and 0.3 $M_\odot$ WD: the final separation $D_{\rm fin}$ and the position of the initial radiative zone $R_{\rm rad}$.

vations that such systems can have period as short as 0.1 day. This period corresponds to a final separation $\lg D = 10.8$ and in our model it can be achieved only in the case of the very weak tidal efficiency.

2.4 Conclusions

This chapter has been devoted to the construction of the initial conditions in the CE at the start of the merger process. To do this to a degree of acceptable approximation, we have considered different mechanisms affecting the primary star structure during the spiral-in. We analyzed effects of the initial conditions on the outcome and compared these to the results of numerical simulations. Mainly we can conclude the following:

- Corotation of matter within the binary orbit can normally be obtained for a secondary of the mass larger than 1 $M_\odot$. For a small mass ratio, when the secondary is 1 $M_\odot$, since there is no final slow spiral-in, the results normally do not show co-rotation at the end of the spiral-in. It can therefore be predicted that for a low mass secondary the merger process will be a very dynamical event and therefore not necessarily be handled well with the evolutionary code.

- For the considered CE systems the results of the calculations using the hydrostatic and the hydrodynamical versions of the code did not show qualitative differences in the CE structure apart from the amount of the mass lost by the primary.

- The efficiencies of tidal and the viscous friction affect the time of the spiral-in, but do not produce much difference in the structure of the CE at the end.

- The initial conditions for the angular velocity in the primary envelope is the main parameter (for an assumed mass loss law) which defines the mass of the primary at the end of the spiral-in.

The described method, being implemented into the evolutionary code, allow us to us construct the initial conditions in the primary envelope for the merger stage. Also, the method might be used for general simplified studies of CE systems.

Chapter 3

Stream: Leaving the Secondary. The ballistic phase

The spiral-in stage ends when the secondary starts to fill its Roche lobe. Since the secondary is still affected by drag forces caused by the common envelope, the orbit continues to shrink, driving mass transfer from the secondary to the core of the giant at very high rates. Apart from the high rate, there are a few other specific features which make this mass transfer different from the normal RLOF mass transfer. First of all, the stream of the secondary material forms and emerges from the secondary within the hot and opaque envelope, the effect of which can not be neglected considering the stream trajectory. Another issue is connected to the rotation of the secondary. The spiral-in lasts, as has been shown in the previous chapter, at most several hundred years. Secondaries with a radiative envelope and a convective core will not establish synchronous rotation during this time scale (for the synchronization due to dynamical tides see, e.g., Zahn 1975). On the other hand, during the spiral-in, the secondary accretes primary material, accumulating angular momentum and can therefore significantly spin up compared to its original rotation (see e.g. Packet 1981). As a result the secondary can be in asynchronous rotation with the binary orbital motion.

This chapter concentrates on the study of the mass transfer from the secondary at its initial stage, before the stream trajectory starts to be significantly affected by the ambient matter. In Section 1 we describe the model for the mass loss rates calculations. Section 2 is devoted to the stream at the L_1 point – we discuss general stream characteristics (the density and the width) for an adiabatic and an isothermal stream. We also introduce and discuss the physics of a stream formed in a synchronized secondary and we provide formulae for calculations of such a stream. Section 3 contains the description of the ballistic calculations for an adiabatic stream. In Section 4 we discuss results - the stream characteristics for different systems.

3.1 Mass loss rates

For high mass loss rates, occurring on the time-scale shorter than the nuclear or thermal time-scale of a main-sequence star, the radius responds adiabatically to mass loss, i.e.

$$\frac{\dot{R}_2}{R_2} = \left(\frac{\partial \ln R_2}{\partial \ln M_2}\right)_{\rm ad} \frac{\dot{M}_2}{M_2} = \zeta_{\rm ad} \frac{\dot{M}_2}{M_2}, \tag{3.1}$$

where R_2 and M_2 are the radius and the mass of the mass-losing secondary, respectively.
The Roche-lobe radius $R_{\rm RL}$ of the secondary changes according to

$$\frac{\dot{R}_{\rm RL}}{R_{\rm RL}} = \left(\frac{\partial \ln R_{\rm RL}}{\partial \ln M_2}\right)_{D={\rm const}} \frac{\dot{M}_2}{M_2} + \left(\frac{\partial \ln R_{\rm RL}}{\partial t}\right)_{\dot{M}_2=0} \equiv \zeta_{\rm RL} \frac{\dot{M}_2}{M_2} + \left(\frac{\partial \ln D}{\partial t}\right)_{\dot{M}_2=0} \tag{3.2}$$

where the Roche-lobe radius $R_{\rm RL}$ is given by Eggleton 1983.

$$R_{\rm RL} = \frac{0.49 q^{2/3}}{0.6 q^{2/3} + \ln(1+q^{1/3})} D. \tag{3.3}$$

Here $q = M_2/M_1$ is the mass ratio, and M_1 is the total mass of the primary core within the binary separation D.

Assuming that the radius of the star is equal to the Roche-lobe radius, we can equate equations 3.1 and 3.2 and obtain an estimate for the mass-loss rate from the secondary as

$$\frac{\dot{M}_2}{M_2} = \frac{1}{\zeta_{\rm ad} - \zeta_{\rm RL}} \left(\frac{\partial \ln D}{\partial t}\right)_{\dot{M}_2=0}, \tag{3.4}$$

where $\partial \ln D/\partial t$ is the change in the orbital separation due to tidal and viscous friction. The typical rate of the orbit dissipation due to tidal and viscous friction in the central region at the moment when the secondary stars the mass transfer is $\frac{\partial \ln D}{\partial t} \approx$ few$\cdot 10^{-8}$ sec^{-1}. The corresponding rate of the mass loss is in the range of 0.01 to $10\,{\rm M}_\odot\,{\rm yr}^{-1}$. To obtain values for $\zeta_{\rm ad}$, we performed separate stellar-evolution calculations where mass was taken off the assumed secondary on a time-scale much shorter than the thermal time-scale in its outer envelope. These calculations are performed for the

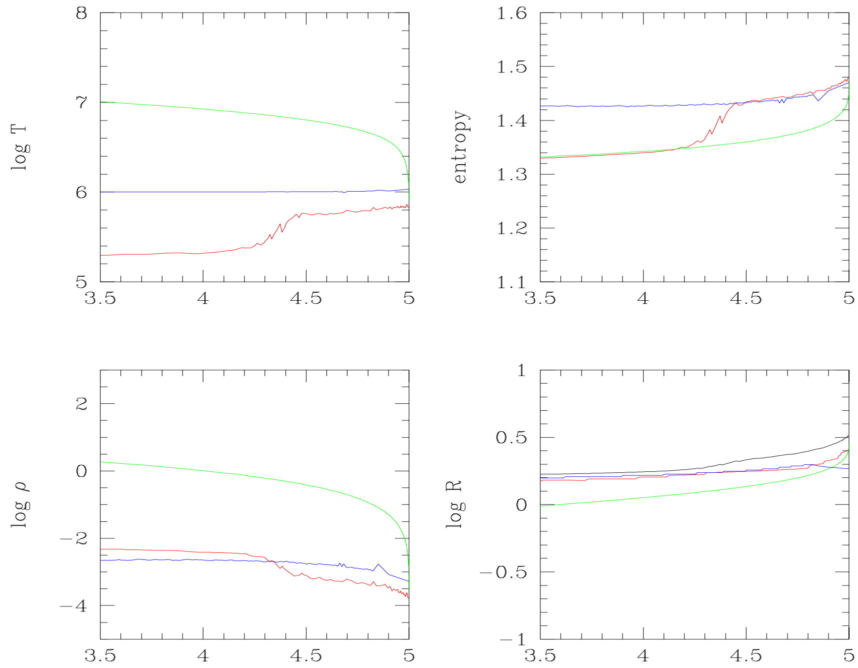

Figure 3.1: Evolution of the surface values for the radius, the entropy, the density and the temperature for a secondary of $5\,\mathrm{M}_\odot$ during the mass loss phase. The abscissa here corresponds to the mass of the secondary. Blue lines correspond to the surface values for the secondary inside the CE (with a mass loss rate $\dot{M} = 0.01\ \mathrm{M}_\odot\,\mathrm{yr}^{-1}$). Red lines show values for the secondary alone (with $\dot{M} = 1\ \mathrm{M}_\odot\,\mathrm{yr}^{-1}$). Green lines represent the initial profiles (as a function of mass).

secondary alone and with a boundary condition appropriate for the CE. The mass loss calculations for the secondary in the CE are less stable numerically and converged only for mass loss rates $\dot{M} \leq 0.01 M_\odot$. But we found that, after the removal of the surface entropy pike, the structure of the secondary in isolation and inside a CE change in the same way, becoming increasingly closer as we increase the mass loss rate for the secondary in the CE (see Fig. 3.1). Therefore for mass loss rates we decided to use a combined model, calculated with a CE at the start and at the faster mass loss rates without CE later ($\dot{M} \geq 1 M_\odot$).

3.2 The stream at L_1

In previous treatments of mass outflow from L_1, it was generally assumed that the stream was isothermal (see e.g. Lubow and Shu 1975; LS; Bisikalo *et al.* 1997). Because of the high expected mass-loss rates in our problem, it is more appropriate to assume that the stream behaves adiabatically – the radiative diffusion timescale is generally much longer than the characteristic flow timescale (for a stream with a radius of 10^{10} cm, the diffusion time is of order 10^6 s). For completeness we also provide consideration of the isothermal stream.

3.2.1 The stream density profile and width

In the case where the secondary's spin is aligned and synchronous with the orbit, we can determine the density distribution in the neighbourhood of the L_1 point by expanding the potential Φ around this point in a Taylor series (see e.g. LS), where we use Cartesian coordinates (x, y, z):

$$\begin{aligned}
\Phi &= -\frac{GM_1}{|\boldsymbol{r_1}|} - \frac{GM_2}{|\boldsymbol{r_1}|} - \frac{1}{2}\left(\Omega\, \boldsymbol{e_z} \times \boldsymbol{r}\right)^2 \ , \\
\Phi &= \Phi_{L1} + \left(\frac{\partial^2 \Phi}{\partial x^2}\right)\bigg|_{L1} \frac{(x - x_{L1})^2}{2} + \left(\frac{\partial^2 \Phi}{\partial y^2}\right)\bigg|_{L1} \frac{y^2}{2} + \left(\frac{\partial^2 \Phi}{\partial x^2}\right)\bigg|_{L1} \frac{x^2}{2} \ , \\
\left(\frac{\partial^2 \Phi}{\partial x^2}\right)\bigg|_{L1} / \ \Omega^2 &= -2\left(\frac{\mu}{|x_{L1}/D - 1 + \mu|^3} + \frac{1-\mu}{|x_{L1}/D - \mu|^3}\right) - 1 = -2A - 1 \ , \\
\left(\frac{\partial^2 \Phi}{\partial y^2}\right)\bigg|_{L1} / \ \Omega^2 &= A - 1 \ , \quad \left(\frac{\partial^2 \Phi}{\partial z^2}\right)\bigg|_{L1} = A \qquad \longrightarrow \\
\Phi &= \Phi_{L1} - (2A+1)\frac{(x - x_{L1})^2}{2}\Omega^2 + (A-1)\frac{y^2}{2}\Omega^2 + A\frac{z^2}{2}\Omega^2 \ . \qquad (3.5)
\end{aligned}$$

Here Ω is the angular speed of the binary and $\mu = M_1/(M_1 + M_2)$.

A natural assumption is that the energy distribution within the stream, consisting of kinetic and internal energies, follows the shape of the Roche potential and that the Bernoulli integral for the matter leaving the donor star is conserved (for an adiabatic stream)

$$B \equiv \Phi + \frac{u^2}{2} + \frac{c^2}{\gamma - 1} = \Phi_{L_1} + \frac{{u_{L_1}}^2}{2} + \frac{c_{L_1}^2}{\gamma - 1} \ . \qquad (3.6)$$

Here u_{L_1} and c_{L_1} are the velocity and the sound speed of the matter at L_1, and γ is the adiabatic index of the stream material. Let us assume that in the L_1 neighbourhood the stream is laterally in hydrostatic equilibrium. This is a good approximation, especially in the $Z-$direction (LS). Then, in the $YZ-$plane

$$\Phi - \Phi_{L1} = \left(\frac{A-1}{2}y^2 + \frac{A}{2}z^2\right)\Omega^2 \approx \frac{\alpha}{2}r^2\Omega^2, \qquad (3.7)$$

where r is the distance to the L_1 point and $\alpha \approx A$ is a unitless constant which depends on the shape of the potential in the neighbourhood of L_1. For binary systems with a mass ratio, q, between 0.006 and 1.0, it has a value of 6.16 to 8.0 (LS). Then the density distribution within an adiabatic stream can be obtained from the condition of lateral hydrostatic equilibrium as (see the derivation in appendix B)

$$\rho = \rho_c \left(1 - \frac{\alpha}{2}\frac{r^2}{\widetilde{W}^2}\right)^{1/(\gamma-1)} \tag{3.8}$$

where ρ_c is the density of the material in the core of the stream, and $\widetilde{W}$ is the characteristic width of the stream, which depends on the properties (e.g. entropy, temperature) of the matter in the secondary:

$$\widetilde{W} = \sqrt{\frac{\gamma}{\gamma-1}\frac{s^{\frac{1}{2}}\rho_c^{1/3}}{\Omega}}. \tag{3.9}$$

Here $s = P/\rho^\gamma$ is the adiabatic constant of the material from the secondary. An adiabatic stream cannot have a width larger than $W = \widetilde{W}\sqrt{2/\alpha}$ (as can be seen from equ. 3.8). Nevertheless, such a stream will not have sharp edges, as predicted by the adiabatic density profile, since the very outer part of the stream is likely to be more isothermal, smoothing the density profile. Since the density there will be small compared to the central density, this part of the stream will not significantly affect the properties of most of the stream material.

The analogous consideration for an isothermal stream shows that this kind of stream will have a Gaussian density distribution at the L_1

$$\rho = \rho_c \exp(-\frac{\alpha}{2}\frac{r^2}{\widehat{W}^2}), \tag{3.10}$$

with a corresponding characteristic width

$$\widehat{W} = \sqrt{\frac{1}{\gamma}\frac{c_{L_1}}{\Omega}}\ . \tag{3.11}$$

The analysis for an isothermal stream is very similar to the analysis given by LS. Bisikalo *et al.* (1997) have performed detailed numerical simulations of an isothermal stream in a common envelope in the vicinity of L_1. Using their results, we have confirmed that the density profile can be well fitted by a Gaussian with a value of $\alpha \approx 8$, consistent with the estimates obtained from an expansion of the potential ($\alpha \approx 6 - 8$).

We assume that the velocity of the material at L_1 is given by the local sound speed (see LS) and that this speed varies through the stream cross-section. Then, integrating the mass-flow rate across the stream cross section near L_1, we can relate the mass-loss rate $\dot{M}_2$ (in units of $\mathrm{M_\odot\,yr^{-1}}$) to the density in the stream core for an adiabatic stream (with $\gamma = 5/3$):

$$\rho_{\rm c} = 1.4 \times 10^{-3}\mathrm{g\,cm^{-3}}\dot{M}_2^{1/2}\Omega_4 s_{15}^{-3/4}\left(x_{\rm s}^2 - \frac{\alpha}{2}x_{\rm s}^4 + \frac{\alpha^2}{12}x_{\rm s}^6\right)^{-\frac{1}{2}}\ , \tag{3.12}$$

where $s_{15} = (P/\rho^\gamma)/(10^{15}\mathrm{cgs})$ is the scaled adiabatic constant of the material from the secondary, $\Omega_4 = \Omega/10^{-4}\mathrm{s^{-1}}$, $x_{\rm s} = W/\widetilde{W}$ is the unitless stream width. For an isothermal stream the connection between mass loss rate and the stream density is:

$$\rho_{\rm c} = 0.17\mathrm{g\,cm^{-3}}\ \dot{M}_2\Omega_4^2 c_6^{-3}\alpha\left(1 - e^{-\frac{\alpha}{2}x_{\rm s}^2}\right)^{-1}\ , \tag{3.13}$$

where $c_6 = c_{L_1} \cdot 10^{-6}$ [cm/s] is the scaled surface sonic velocity and $x_{\rm s} = W/\widehat{W}$ is the unitless width of an isothermal stream.

When mass loss occurs before the star overfills its Roche lobe, the stream width can be estimated by considering how far a particle on the surface of the star can be away from the L_1 point and escape from the critical Roche potential, assuming that the flow speed is the sound speed at the L_1 point itself. In the case when the surface of the secondary coincides with the secondary Roche lobe, the stream width is given by $W = \widehat{W}\sqrt{\gamma}/\sqrt{\alpha}$ for an isothermal stream and $W = \widetilde{W}\sqrt{\gamma - 1}/\sqrt{\alpha}$ for an adiabatic stream.

When the secondary overfills its Roche lobe, we can estimate the allowed width of the stream from the size of the zone (for simplicity considered in the orbital plane) which has the same or a smaller potential than the potential at the point on the stellar surface from which matter flows out. The maximum possible potential difference occurs when the amount of Roche lobe overfilling, ΔR, corresponds to the difference between the stellar radius and the Roche-lobe radius at the point with coordinates $(X_2, R_{\rm r}, 0)$, where X_2 is the position of the secondary and $R_{\rm r}$ is the y-coordinate, where the potential is equal to Φ_{L_1}. This leads to an estimate of the stream width of

$$W^2 = 2\Delta R \left. \frac{\partial \Phi}{\partial y} \right|_{R_\mathrm{r}} \Bigg/ \left. \frac{\partial^2 \Phi}{\partial y^2} \right|_{L_1}, \tag{3.14}$$

or, in more compact form,

$$W = \sqrt{\Delta r} D f(q), \tag{3.15}$$

where $r = \Delta R/D$ gives the dimensionless fraction by which the secondary overfills its Roche lobe and f is a function that depends only on the mass ratio q and can be determined numerically (e.g. for $q = 1$, $f(q) = 0.96$ and for $q = 0.1$, $f(q) = 0.06$).

Using equation (3.12) and assuming that the stream has maximum width, i.e. $x_s = \sqrt{2/\alpha}$), it is easy to show that, for a mass-loss rate of order $1\,\mathrm{M}_\odot\,\mathrm{yr}^{-1}$, the pressure at the centre of the stream could not exceed $\sim 10^{10}$ $\mathrm{dyn\,cm}^{-2}$. This value is generally lower than the pressure found in the hot, high-pressure environment of a common envelope, where the pressure is typically in the range of $10^{10} - 10^{12}$ $\mathrm{dyn\,cm}^{-2}$. This implies that the stream will generally be compressed by the pressure in the ambient envelope. We can estimate its initial width by assuming that the outer edge of the stream is in pressure balance with the common envelope. The stream density at the edge cannot be less than

$$\rho_\mathrm{out} = (P_\mathrm{CE}/s)^{1/\gamma}\ , \tag{3.16}$$

where P_CE is the ambient pressure in the common envelope. The stream width for the current mass loss rate then can be found from the equ. (3.12) in combination with

$$\rho_\mathrm{c} = (P_\mathrm{CE}/s)^{1/\gamma} \left(1 - \frac{\alpha}{2} x_\mathrm{s}^2\right)^{-1/(\gamma-1)} \tag{3.17}$$

(from equ. (3.8)). For an isothermal stream

$$\rho_\mathrm{c} = \gamma P_{CE}/c_{L_1}^2 \exp\left(\frac{\alpha}{2} x_\mathrm{s}^2\right)\ . \tag{3.18}$$

3.2.2 The effect of non-synchronous rotation

Since the secondary's spin may not be synchronous with the orbit (in fact, it may be rotating faster or more slowly depending on the circumstances), we also need to consider the case of non-synchronous rotation. For this purpose we adopt a coordinate system that rotates with the secondary. At the equipotential surface which determines the surface of the secondary (the donor), there is an area where matter is being accelerated outwards from the stellar surface. From this zone matter may flow out. In the case of a synchronized secondary, the physical situation is a close analogue of a Laval nozzle[1], where the equipotential surfaces take over the role of a nozzle. In the standard case, when a thin flow is considered, L_1 can be taken as a point. Then, as for the case of the standard Laval nozzle, matter is almost completely unaffected by external acceleration at the nozzle mouth (at the sonic point), but experiences negative acceleration before and positive acceleration after passing though the nozzle.

For an asynchronously rotating secondary, the position of the positive acceleration zone with respect to the secondary changes with time. To parameterise the degree of a-synchronicity, we introduce a parameter f,

$$f = \frac{\Omega_{\rm sec}}{\Omega} - 1, \tag{3.19}$$

where $\Omega_{\rm sec}$ is the angular velocity of the secondary. The parameter f is zero if the secondary rotates synchronously. The position of the point where the acceleration experienced by matter on the stellar surface becomes non-negative can be found similarly to the L_1 point (in order to avoid confusion with the standard L_1 point, we refer to this point as the 'leaving point', LP), considering the generalised Roche potential, Ψ, for the frame with the origin at the center of the secondary, which rotates with the secondary (see e.g. Kruszewski 1963 , Limber 1963):

$$\Psi = \Phi - \frac{\zeta^2 + \eta^2}{2} f(f+2)\Omega^2 \, . \tag{3.20}$$

Here and (ζ, η) are Cartesian coordinates in the frame rotating with the secondary. For a secondary

[1]A Laval nozzle is a nozzle that first narrows and then widens. In such a nozzle matter is initially moving with subsonic speed and becomes supersonic after it has passed through the nozzle (see e.g. Landau and Lifshitz 1959). In the standard model of a Laval nozzle, there is no external acceleration

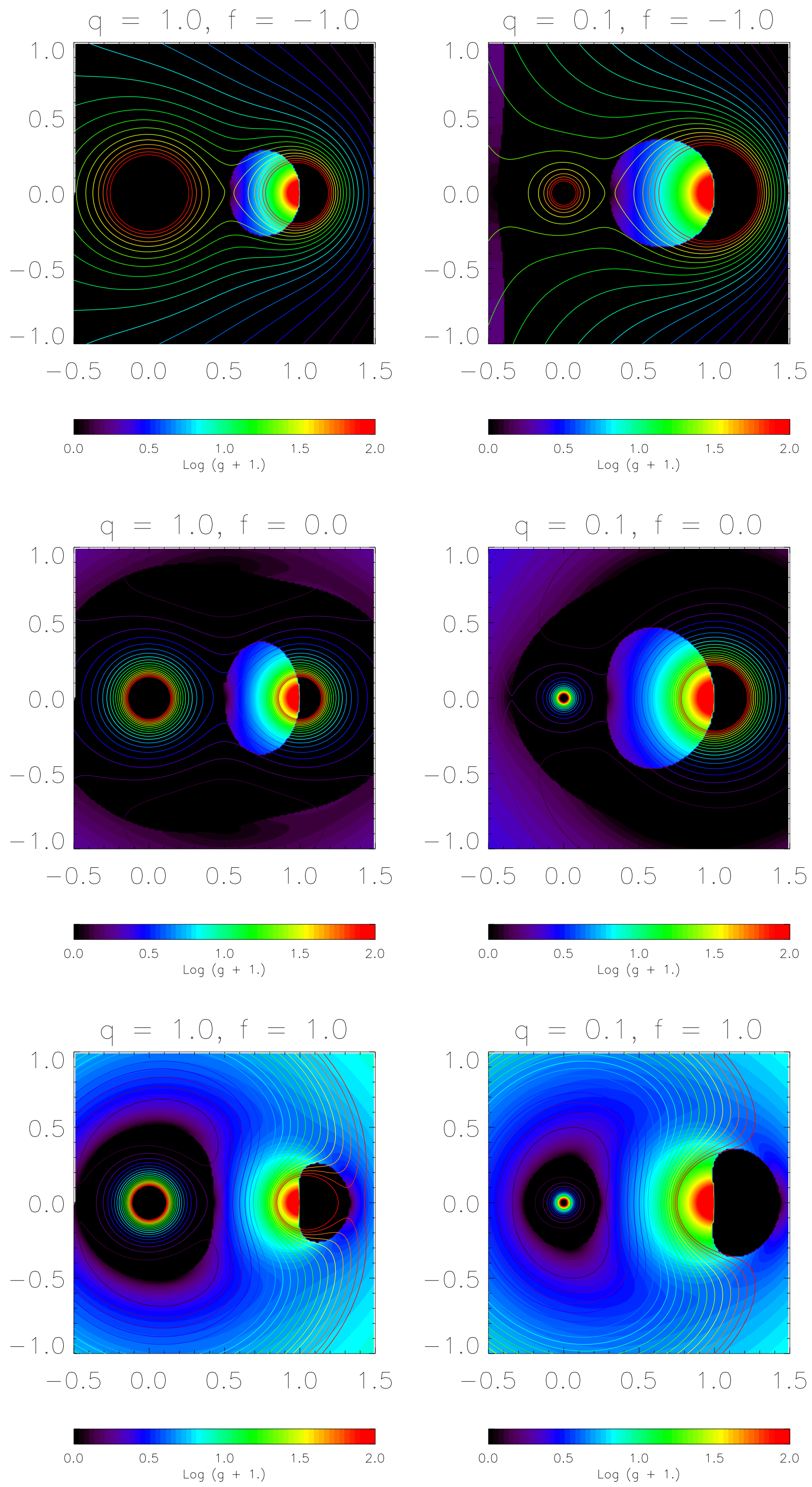

Figure 3.2: Equipotential lines and areas of positive acceleration in the binary (at the orbital plane, distances in the units of the binary separation). The secondary is on the left. From top to bottom - synchronisation parameters $f = -1; 0; 1$. From left to right - mass ratios $q = 1, 0.1$. The acceleration g is unitless. Color bars show colors only for acceleration.

which rotates faster than the binary itself, LP will normally be shifted from L_1 towards the donor; and for a secondary which rotates more slowly than the binary this point will be shifted towards the primary (see Fig. 3.2). A rough estimate of the linear speed with which the zone of positive acceleration travels across the secondary surface, $v_{\rm zone} = f\Omega_{\rm sec}r_{\rm sec}$, shows that it is typically twice the local sound speed of the secondary (for the case of $f = 1$ and considering parameters characteristic for a system at the point where the secondary starts to overfill its Roche lobe). In this case, we do not have a normal nozzle (as for a synchronized secondary), as matter at a particular position on the secondary's surface (in the frame rotating with the secondary) is not affected by any matter that has escaped from the secondary before it enters the zone of non-negative acceleration. Therefore we may consider what happens to a fluid element on the secondary independently from any matter that has flowed out previously. A physical analogue of this situation is a ball, containing the (secondary) matter, that is separated from the outside by negative acceleration. At the surface of the ball there is a hole which travels with supersonic speed. As far as the matter in the ball is concerned, the surface of the ball acts like a wall that is suddenly being removed (for some period of time) and then placed back again. Matter will escape from the ball through the hole only if the duration of the interval of positive acceleration is long enough for matter to be able to escape before it is pulled back by the negative acceleration. Another analogue of the problem is the sudden expansion of a gas sphere into a vacuum. In this case, the speed with which matter expands can be as high as 3 times the sonic speed (see e.g. Zeldovich and Raizer 1966). In a real situation, we may expect a combination of these and other effects that cannot be easily treated analytically. As this discussion shows, for an a-synchronously rotating secondary, the range of the possible initial flow velocities includes significantly supersonic speeds. Fortunately, our ballistic calculations in § 3 show that the stream properties close to the primary core are not strongly dependent on the initial flow velocity in the stream.

3.2.3 The escape angle - generalization of the LS formalism

In the case where the secondary's spin is not synchronous with the orbit, the angle at which matter leaves the secondary will be different from the synchronous case analyzed by LS. To obtain this angle in our problem, we generally follow the LS formalism with the following changes: we place the origin of the coordinate system not at L_1 but at LP, and we use a coordinate frame which rotates with the secondary. Using cylindrical coordinates, the potential (3.20) in the neighbourhood of LP can be expanded in a Taylor series around LP (in the $Z = 0$ plane) as

$$\Phi = \Phi_{LP} - \left[1 + f(f+2) + \frac{A_{LP}}{2}(3\cos 2\theta + 1)\right]\frac{r^2}{2}\Omega^2, \tag{3.21}$$

where A_{LP} is the positive unitless constant for a binary with asynchronously rotating secondary:

$$A_{LP} = \frac{\mu}{|x_{LP}/D - 1 + \mu|^3} + \frac{1-\mu}{|x_{LP}/D + \mu|^3}, \tag{3.22}$$

where x_{LP} is the distance between the center of mass and LP and θ is the angle between the flow direction of the stream and the direction of the primary.

Similar to the derivation in LS, we use this expansion of the potential in the neighborhood of LP in the hydrodynamical equations (analogously to eqs. (14a)–(14c) in LS) and obtain a system of equations for the modified radial velocity ($U(\theta_s) = u_r/cD/r$ and the escape angle θ_s (analogoulsly to eqs. (23a) and (23b) in LS):

$$\begin{aligned} U^2(\theta_s) &= 1 + \frac{A_{LP}}{2}(3\cos 2\theta_s + 1) + f(f+2), \\ U(\theta_s) &= -\frac{3}{4}A_{LP}\sin 2\theta_s \end{aligned} \tag{3.23}$$

After the elimination of $U(\theta_s)$, the escape angle of the stream in the frame rotating with the secondary can be found from the equation

$$\cos^2 2\theta_s + \frac{8}{3}\cos 2\theta_s + \frac{16}{9A_{LP}^2}\left(\frac{A_{LP}}{2} + 1 + f(f+2) - \frac{9A_{LP}^2}{16}\right) = 0. \tag{3.24}$$

For the case of a synchronously rotating secondary (f=0), this equation reduces to the solution for θ_s obtained by LS. The angle with which the stream will escape from LP in the frame co-rotating with the binary is given by the transformation

$$\tan\theta = \frac{f\Omega D(1 - \mu + x_{LP}/D) + v_e \sin\theta_s}{v_e\cos\theta_s}, \tag{3.25}$$

where v_e is the velocity of the stream at the nozzle (sonic for a synchronously rotating secondary).

3.3 The ballistic phase

The motion of the stream can be naturally divided into two phases, a (quasi-)ballistic phase where the stream trajectory is not strongly affected by the interaction with the ambient matter, which can be treated more or less ballistically, and a hydrodynamical phase where the dynamics of the stream is dominated by the hydrodynamical interaction with the core. Considering these two phases separately helps to avoid numerical problems (due to the complexities near the L_1 point) at the start of the hydrodynamical calculation. However, it also introduces some uncertainty since matter in the inner region surrounding the primary core may not be in complete co-rotation with the orbit and will have a backward motion with respect to the co-rotating frame. Such relative rotation causes a force which reduces the interception angle between the falling stream and the normal direction to the core relative to the predictions from a purely ballistic trajectory.

Unlike the isothermal case, considered by LS and Lubow and Shu (1976) where the stream has a constant sonic speed, for an adiabatic stream, the stream trajectory is not purely ballistic, as this would not conserve the Bernoulli integral (equ. 3.6) along a streamline. Therefore a pressure term has to be taken into account in the calculation of the flow trajectory. As first approximation, we assume that the stream is in hydrostatic equilibrium with the envelope in the direction normal to the flow and that, during this ballistic stage, the structure of the stream is isomorphic (in a sense that it follows the shape of the potential field). We can then apply for the mass conservation equation the same approach for the density profile as used before. It implies also that, in the stream center, the only density derivative is in the direction of the stream trajectory, $\boldsymbol{l}$, and that there is no derivative normal to the direction of the flow $\boldsymbol{n}$ (here we do not consider higher-order terms in the density expansion). The curvature of the trajectory in the rotating system is determined by the work done on the stream material by the potential (gravity and rotation), while the gradient of the pressure along the stream trajectory, $(1/\rho)\,\partial P/\partial l$, only affects the change in the velocity component along the trajectory. This term is generally small, since the Mach number of the flow is large except near the nozzle, but ensures conservation of the Bernoulli integral and kept for completeness and consistency in the calculations. These considerations lead to a reduced set of equations for the central stream trajectory, which in Cartesian coordinates (with the origin at the center of mass) can be written as:

$$u_x \frac{\partial u_x}{\partial x} + u_y \frac{\partial u_x}{\partial y} = -\frac{\partial \Phi}{\partial x} + 2u_y \Omega - \frac{1}{\rho}\frac{\partial P}{\partial \boldsymbol{l}}\frac{u_x}{u} \,,$$
$$u_x \frac{\partial u_y}{\partial x} + u_y \frac{\partial u_y}{\partial y} = -\frac{\partial \Phi}{\partial y} - 2u_x \Omega - \frac{1}{\rho}\frac{\partial P}{\partial \boldsymbol{l}}\frac{u_y}{u} \,. \tag{3.26}$$

Here $u = \sqrt{u_x^2 + u_y^2}$ is the magnitude of the central stream velocity, and u_x, u_y are its components. The structure of the common envelope enters into these equations through the pressure boundary condition at the stream edge, which is set equal to the ambient pressure in the envelope. The density within the stream is related to the pressure by the adiabatic constant of the secondary material $s = P/\rho^\gamma =$ const. Together with a specified mass-flow rate, this set of equations provides a complete set that completely describes the dynamics of the stream in this phase.

The initial conditions for the hydrodynamical simulations are taken directly from the parameters obtained from the ballistic calculations for a range of binary parameters. Specifically, we consider parameters representing the spiral-in and subsequent merger of a secondary of 1 and 5 $\mathrm{M}_\odot$ inside a 20 $\mathrm{M}_\odot$ evolved supergiant which has completed helium burning in the core and has a core mass of $\sim 7\,\mathrm{M}_\odot$. To model the secondaries, we first followed their evolution to the same age as the primary and then evolved them further, subjecting them to very fast mass loss to model their adiabatic response to mass loss. These calculations give the radii of the stars and their surface entropies as a function of current stellar mass. Fig. 3.3 presents examples of the ballistic trajectories.

Tables 3.1 and 3.2 illustrate the evolution of the stream properties during the ballistic phase as the secondary mass decreases. Here, the initial parameters for the ballistic calculations, such as the entropy and separation, were determined from the current mass of the secondary (note that these calculations did not take into account any changes in the properties of the core and the surrounding envelope during the merging phase; these will be treated self-consistently in Chapter 5). The mass-flow rate does not strongly affect the results apart from the stream width. In Table 3.3 and 3.4 we present the results of calculations for the same CE systems, but where we set the asynchronicity parameter to $f = 1$ (i.e. where the secondary rotates twice as fast as the binary).

Table 3.5 shows for comparison the results for calculations with decreased compression from the ambient pressure (more ballistic calculations, where the ambient pressure has been taken as 5%

Table 3.1: Stream properties at the end of the ballistic calculation representative for a 20 + 1 $\mathrm{M}_\odot$ CE simulation

M_2	$\log s$	D [10^{11}cm]	$M_{\rm int}$	$M_{\rm ext}$	$v_{\rm fin}[10^8\ {\rm cm\,s^{-1}}]$	η_ρ	Θ	$R_{\rm str}[\pi]$
1.0	14.88	2.6	5.6/5.0	1.8/2.1	0.73/1.02	11.3/6.9	41° /47°	0.024/0.014
0.9	14.87	2.4	5.2/4.8	1.7/2.0	0.68/0.98	11.6/7.0	41° /47°	0.024/0.014
0.8	14.70	2.2	5.2/5.1	1.5/1.9	0.60/0.93	14.6/8.8	39° /45°	0.023/0.013
0.7	14.49	2.0	5.6/5.8	1.4/1.8	0.56/0.90	19.8/11.9	38° /44°	0.021/0.011
0.6	14.32	2.1	6.6/6.7	1.4/1.9	0.58/0.93	24.8/15.0	39° /46°	0.018/0.010
0.5	14.22	2.2	7.9/7.6	1.6/2.0	0.66/0.98	28.6/17.3	43° /50°	0.016/0.009
0.4	14.14	2.3	9.3/8.5	1.8/2.1	0.73/1.05	31.5/19.1	47° /56°	0.014/0.008
0.3	14.09	2.8	11.5/9.7	2.2/2.3	0.87/1.15	33.7/20.5	57° /69°	0.013/0.007

Note. – M_2: mass of the secondary, the mass donor, $\log s$: logarithm of the adiabatic constant (p/ρ^γ in cgs units), D: binary separation. In all cases, the initial stream velocity was assumed to be the local sound speed. Stream parameters (at two different radii from the primary core, 10^{11} and 7.5×10^{10} cm, respectively): $M_{\rm int}$, $M_{\rm ext}$: internal and external Mach numbers of the stream material (i.e. relative to the stream sonic velocity and relative to the ambient sonic velocity); $v_{\rm fin}$, stream velocity; η_ρ: ratio of the central stream density to the ambient density; Θ: stream angle relative to the primary core center, $R_{\rm str}$: angular radius of the stream. The values are representative for CE systems consisting initially of a giant of 20 $\mathrm{M}_\odot$ (with a 7 $\mathrm{M}_\odot$ core) and a 1 $\mathrm{M}_\odot$ secondary, where the secondary is assumed to lose mass at a rate $\dot{M} = \mathrm{M}_\odot\,\mathrm{yr}^{-1}$. The ambient temperatures and densities at the radii given in the table are ($T = 6\times10^6$ K, $\rho = 5\times10^{-3}\ {\rm g\,cm^{-3}}$) and ($T = 10^7$ K, $\rho = 2.5\times10^{-2}\ {\rm g\,cm^{-3}}$), respectively.

Table 3.2: Stream properties at the end of the ballistic calculation representing a 20 + 5 $\mathrm{M}_\odot$ CE simulation

M_2	$\log s$	D [10^{11}cm]	$M_{\rm int}$	$M_{\rm ext}$	$v_{\rm fin}[10^8\ {\rm cm\,s^{-1}}]$	η_ρ	θ	$R_{\rm str}[\pi]$
5.0	16.50	5.1	1.3/0.8	1.4/1.1	0.64/0.53	1.1/0.6	29° /15°	0.098/0.076
4.5	15.96	3.6	2.6/2.2	1.6/1.8	0.70/0.90	3.3/1.8	32° /32°	0.052/0.034
4.0	15.05	3.4	5.1/4.8	1.6/2.1	0.74/1.03	11.8/6.4	33° /36°	0.027/0.017
3.5	14.96	3.2	5.3/5.1	1.6/2.1	0.73/1.02	13.5/7.2	33° /37°	0.025/0.016
3.0	14.90	3.4	6.1/5.6	1.8/2.2	0.80/1.08	14.5/7.7	35° /40°	0.023/0.015
2.5	14.87	3.5	6.5/5.9	1.9/2.3	0.84/1.12	15.1/8.1	38° /42°	0.022/0.014
2.0	14.85	3.7	7.0/6.2	2.0/2.3	0.89/1.16	15.6/8.4	41° /46°	0.021/0.014
1.5	14.83	3.9	7.5/6.5	2.1/2.4	0.93/1.19	16.1/8.6	45° /51°	0.021/0.013

Note. – Similar simulations as in Table 3.1 for a CE systems consisting initially of a 20 $\mathrm{M}_\odot$ giant (as before) and a 5 $\mathrm{M}_\odot$ secondary. The stream parameters are given at radii of 10^{11} and 7.5×10^{10} cm, respectively. The ambient temperatures and densities at these radii are ($T = 7\times10^6$ K, $\rho = 7\times10^{-3}$g/cm^3) and ($T = 10^7$ K, $\rho = 3\times10^{-2}$ g/cm^3), respectively.

Table 3.3: Stream properties at the end of the ballistic calculation representative for a 20 + 1 $M_\odot$ CE simulation, where the secondary rotates with twice the orbital angular velocity.

$M_{\rm sec}$	$\log s$	D [10^{11}cm]	$M_{\rm int}$	$M_{\rm ext}$	$v_{\rm fin}[10^8 \,{\rm cm\,s^{-1}}]$	η_ρ	θ	$R_{\rm str}[\pi]$
1.0	14.88	2.6	5.0/4.5	1.8/2.0	0.73/1.01	15.7/9.2	45° /51°	0.020/0.012
0.9	14.87	2.4	4.7/4.3	1.7/2.0	0.68/0.97	15.9/9.4	44° /50°	0.021/0.012
0.8	14.70	2.2	4.7/4.6	1.5/1.9	0.60/0.92	19.6/11.6	44° /50°	0.020/0.011
0.7	14.49	2.0	5.2/5.3	1.4/1.8	0.56/0.90	25.9/15.3	46° /51°	0.018/0.010
0.6	14.32	2.1	6.1/6.1	1.5/1.9	0.59/0.92	32.1/19.0	48° /54°	0.016/0.009
0.5	14.22	2.2	7.3/7.0	1.6/2.0	0.66/0.98	36.6/21.7	50° /58°	0.014/0.008
0.4	14.14	2.3	8.7/7.9	1.8/2.1	0.74/1.04	39.7/23.7	53° /63°	0.013/0.007
0.3	14.09	2.8	10.7/9.2	2.1/2.3	0.86/1.15	40.6/24.4	48° /41°	0.012/0.007

Note. – Similar simulations as in Table 3.1 but for an asynchronous secondary with $f = 1$ (equ. 17).

Table 3.4: Stream properties at the end of the ballistic calculation representing a 20 + 5 $M_\odot$ CE simulation, where the secondary rotates with twice the orbital angular velocity.

$M_{\rm sec}$	$\log s$	D [10^{11}cm]	$M_{\rm int}$	$M_{\rm ext}$	$v_{\rm fin}[10^8 \,{\rm cm\,s^{-1}}]$	η_ρ	θ	$R_{\rm str}[\pi]$
5.0	16.50	5.1	1.0/0.6	1.1/0.9	0.50/0.45	1.5/0.9	17° /7°	0.093/0.069
4.5	15.96	3.6	2.2/1.8	1.5/1.7	0.67/0.84	4.6/2.5	34° /32°	0.045/0.030
4.0	15.05	3.4	4.6/4.3	1.6/2.1	0.74/1.02	15.7/8.5	45° /47°	0.023/0.015
3.5	14.96	3.2	4.9/4.6	1.6/2.1	0.73/1.02	17.4/9.4	46° /49°	0.022/0.014
3.0	14.90	3.4	5.6/5.0	1.8/2.2	0.80/1.08	19.2/10.4	21° /25°	0.020/0.013
2.5	14.87	3.5	6.0/5.4	1.8/2.2	0.84/1.11	19.6/10.7	46° /50°	0.020/0.013
2.0	14.85	3.7	6.5/5.7	2.0/2.3	0.89/1.15	19.7/10.7	53° /60°	0.019/0.012
1.5	14.83	3.9	7.0/6.0	2.1/2.4	0.93/1.19	19.6/10.7	56° /64°	0.019/0.012

Note. – Similar simulations as in Tabl. 3.2 for an asynchronous secondary with $f = 1$.

Table 3.5: Stream properties at the end of the ballistic calculation representing a 20 + 5 $M_\odot$ CE simulation.

$M_{\rm sec}$	$\log s$	D [10^{11}cm]	$M_{\rm int}$	$M_{\rm ext}$	$v_{\rm fin}[10^8 \,{\rm cm\,s^{-1}}]$	η_ρ	θ	$R_{\rm str}[\pi]$
5.0	16.50	5.1	2.9/2.7	2.1/2.2	0.93/1.11	0.2/0.1	48° /52°	0.071/0.050
4.5	15.96	3.6	4.6/4.7	1.8/2.2	0.80/1.08	0.8/0.3	39° /43°	0.039/0.027
4.0	15.05	3.4	8.4/8.8	1.7/2.2	0.77/1.08	3.0/1.2	35° /39°	0.020/0.014
3.5	14.96	3.2	8.7/9.3	1.7/2.1	0.76/1.06	3.5/1.3	35° /40°	0.019/0.014
3.0	14.90	3.4	10.2/10.2	1.8/2.3	0.82/1.12	3.4/1.4	37° /42°	0.018/0.013
2.5	14.87	3.5	11.0/10.8	1.9/2.3	0.86/1.15	3.4/1.5	39° /45°	0.018/0.012
2.0	14.85	3.7	11.9/11.3	2.0/2.4	0.91/1.19	3.4/1.5	42° /49°	0.017/0.012
1.5	14.83	3.9	12.8/11.9	2.1/2.5	0.95/1.23	3.4/1.5	47° /54°	0.017/0.012

Note. – Similar simulations as in Tabl. 3.2 but with less compression from the ambient matter.

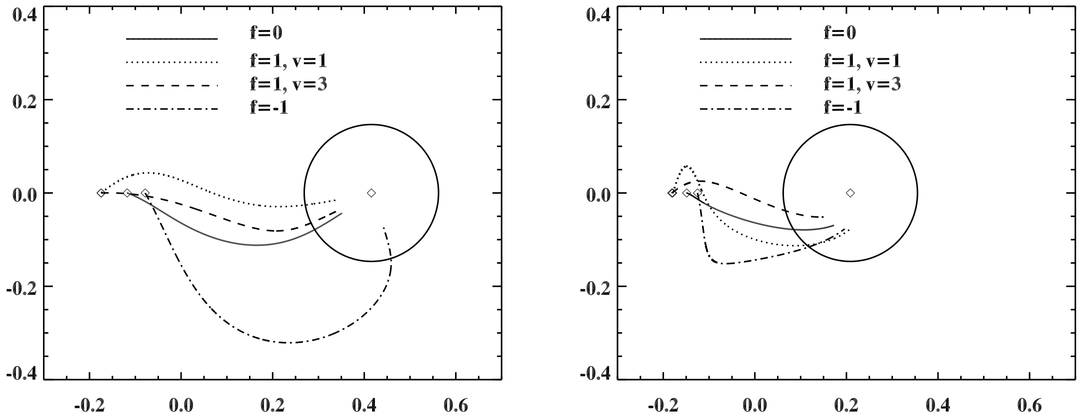

Figure 3.3: Ballistic trajectories for a stream from a massive secondary falling onto the 7 M$_\odot$ core of a red supergiant inside a common envelope (in dimensionless units). The left panel shows the trajectories at the beginning of mass transfer (when the secondary has a mass of 5 M$_\odot$); the right panel shows the trajectories for the same system at a later stage when the secondary's mass has been reduced to 3.5 M$_\odot$. The different labelled trajectories assume different rotation rates for the secondary ($f = 0$: co-rotation with the orbit, $f = 1$: rotating with twice the angular velocity of the binary, $f = -1$: non-rotating). For the case $f = 1$, the trajectories with $v = 1$ and $v = 3$ assume that the initial velocity of the stream material is the local sound speed and 3 times the local sound speed, respectively (in all other cases, the initial speed is taken to be the local sound speed). The large circles indicate a radius of 7.5×10^{10} cm, which we usually choose as the outer boundary for the hydrodynamical calculations.

of the actual ambient pressure). We performed a few hydrodynamical simulations (as described in the next chapter) for this early ballistic stage of the inflow, describing the envelope structure as having a certain pressure gradient and with the primary core of 7 M$_\odot$ and compared the results with the ballistic calculations with the same structure of the CE and with the same gravitational field (no secondary). This comparison shows that the initial parameters are closer to those produced for a stream with full compression, though this effect decreases when the stream is initially more radially directed.

3.4 Conclusions

In this chapter we have discussed different aspects of the physics of a stream formed within the common envelope at the L_1 neighborhood. The main objective of this discussion was to gain a better understanding of the variety of the initial stream parameters, the dependence on such deviations from a standard case as the thickness of the stream, the formation of the stream within the hot ambient matter, the presence of relative rotation of the mass donor and the effect of the ambient matter on the stream trajectory. The stream parameters, such as the velocity, the angle and the density are required for later calculations, aimed to determine of the eventual stream penetration depth. The main results of this chapter are the following:

- We derived formulae which connect the mass loss rate with the stream density at the L_1 point for an adiabatic and an isothermal streams, including the case of a stream formed within a CE.

- The effect of the secondary's asynchronous rotation on the stream outflow physics has been considered and a formula for the angle with which the stream escapes the L_1 point in general case of asynchronous secondary rotation is provided.

- We discussed the possible difference in the physics of the outflow in the case of asynchronous rotation compared to the case of normal RLOF. It has been shown that the initial escape velocity can be as high as three sonic velocities compared to the standard case with one sonic velocity; but it has also been found that it does not affect the final results of ballistic calculations much.

- Ballistic calculations for the specific case of an adiabatic stream in the presence of ambient matter have been done and have been compared with approximate analogs obtained using the hydro-code. The comparison shows that the hydro simulations tends to be rather well matched with the results of calculations where the external pressure taken into account. It means, that compared to the pure ballistic calculations, the resulting stream parameters will be characterized by lower velocity and higher density.

The integrator for the ballistic trajectory has been included into the evolutionary code. It uses as the input the mass loss rates, the binary separation, the secondary's entropy and the effect of the secondary's asynchronousity and produces as output the stream velocity, the angle and the density (with the entropy assumed to be constant) at a certain distance to the primary core.

Chapter 4

Stream: Stream-Core interaction. The hydrodynamic phase

The spiral-in ends when the secondary starts to lose its matter through the L_1 into the common envelope. The stream that forms encounters a medium with increasing pressure, density and temperature. There are several consequences to such an interaction. One is due to the change of the local specific entropy: apart from the injection of high entropy material, the impact of the stream with the core also leads to the generation of entropy at the core neighborhood, possible leading to subsequent mixing in the post-impact region. It may lead to the dredge-up of helium and subsequently to a change of the surface composition. Another effect is the initiation nuclear burning through the hot-CNO in the zone where previously hydrogen has been exhausted. This nuclear burning, taking place in a zone as hot as $10^8 K$, acts as a neutron source for s-processing. The efficiency of these events depends not only on the mass loss rate, but also on how deep the stream can penetrate into the core. For a stream travelling without shocks one can determine the depth to which a stream penetrates using the Bernoulli integral for energy conservation. But due to the interaction with the CE material, material of the stream is shocked, and its entropy changes, therefore the simple analytical estimation is not appropriate.

This chapter is devoted to the study of the stream behavior during the early stages of merging from a hydrodynamical point of view. The main aim of the study is to estimate how deep the stream can penetrate depending on its initial parameters and on the structure of the ambient medium. In order to obtain an estimate for the entropy change of the stream matter, we performed numerical hydrodynamical simulations. In the first section of this chapter we describe the method we use for the hydrodynamical calculations and the stream model. In the second section different physical processes affecting the stream dissipation are considered. The third section is devoted to the parametrization of the results of the numerical simulations.

4.1 The numerical method

4.1.1 The hydrodynamics code

The method for the hydrodynamical simulations which will be suitable for solving the problem of the stream-core interactions has to be first of all well adapted to resolve shocks, or, more generally, to solve Euler equations in the presence of shocks. We refer here to Euler equations instead of considered before for the spiral-in stage Navier-Stokes equations since the viscosity in the radiative region where the stream-core interactions take the place can be neglected, and while the medium is characterized by high opacity, radiative losses also generally not very important. The full system of Euler equations, except the momentum conservation equation and the mass conservation equation contains another hyperbolic equation - the energy conservation equation, and the full system in one spatial dimension is:

$$\begin{aligned} \rho_t + (\rho u)_x &= 0 && \text{conservation of mass} \\ (\rho u)_t + (\rho u^2 + p)_x &= 0 && \text{conservation of momentum} \\ (E)_t + (u(E+p))_x &= 0 && \text{conservation of energy} \end{aligned} \tag{4.1}$$

Here ρ is the density, u is the velocity, p is the pressure and E is the energy. These conservation laws can be written in general terms as

$$q_t(t,x) + f(q(t,x))_x = 0 \; , \tag{4.2}$$

where q is some function (representing physical variables – density, velocity or energy) which depends on the time variable t and the space variable x. $f(q(t,x))_x = \frac{\partial f(q(t,x))}{\partial x}$ and $f(q(t,x))$ is the flux function. If this equation were linear, a solution would be constant along rays $x - ut = x_0$ (characteristics of the equation). But because of the nonlinearity the equation may not have an unique solution – it may happen that characteristics cross and the function $q(x,t)$ has an infinite slope – a shock forms.

Quite a few methods have been developed to numerically solve a hyperbolic equation, and a number of them are based on different approaches of finite difference schemes (with different orders of accuracy). But one of the best methods developed to solve Euler equations for compressible fluid dynamics in the presence of shock waves is the approach proposed by Godunov in (1959). He suggested to synthesize the general velocity field by piecing together the exact solution of the Euler equations for each local region. This exact solution of the local region of the flow is the solution of a so-called Riemann problem (also known as the “shock tube problem” and for certain initial conditions the Sod problem).

A Riemann problem is the conservation law together with a special form of initial conditions, which have a single discontinuity, like

$$q(x,0) = \begin{cases} q_l & \text{if } x < 0 \, , \\ q_r & \text{if } x > 0 \, . \end{cases} \tag{4.3}$$

The solution of a Riemann problem may consist of rarefaction waves, discontinuity and shock. Since the Godunov method is based on the solution of a Riemann problem for each cell interface (considering values at the left and right of the interface as initial data for a Riemann problem), it captures a coming shock and provides as exact a solution as possible with a Riemann solver at any moment. The obvious stability condition of this method will be the requirement that these solutions to Riemann problems should not interact during a time step. Therefore, we have the condition on the integration time-step Δt – the Courant-Lewy-Friedrichs (CFL) condition – that a numerical domain has to contain the true domain of dependences, and so

$$\Delta t \leq N_{\mathrm{CFL}} \frac{\Delta x}{\max|u + c_s|} \, , \tag{4.4}$$

where Δx is the cell size and c_s is the sound speed. The scheme will remain stable with a Courant number $N_{\mathrm{CFL}} \leq 0.9$.

The conservation laws do not always satisfy Equ. (4.2) – there could be some sources or sinks of the quantity considered [for conservation]. Examples are radiative heat transfer (energy can be transferred much faster than it could be done by fluid motion), nuclear burning, external forces like the gravitational field. Generally, these effects are considered as source terms for the conservation equations and the equation can be written in the form:

$$q_t(t,x) + f(q(t,x))_x = \psi(q,x) \ , \tag{4.5}$$

where $\psi(q,x)$ is the source function. E.g., gravity leads to a source term in the momentum conservation and in the energy conservation equations.The usual way to solve conservation laws with source term in the Godunov approach is the operator splitting method, where the homogeneous conservation law (4.2) and the ordinary differential equation

$$q_t = \psi(q,x) \tag{4.6}$$

are solved separately.

If the flux gradients $f(q(t,x))_x$ are nonzero but exactly balanced with the source terms, we have a case of steady state for the conservation laws. Gas dynamics with a gravitational field, either constant or with self-gravity is a good example for such a steady state. The numerical simulations of steady states experience difficulties (LeVeque 1998). Since for both steps we use different numerical methods(a Riemann solver for a homogeneous conservation law and e.g. a finite difference method for the differential equation with a source term), it is unlikely to lead to exact cancellation. For such a case of a steady-state problem a special method for balancing source term and flux gradients has been developed by LeVeque (LeVeque 1998). The basic idea is to modify the initial data for a Riemann problem according to the given term source.

Since of the basic idea Godunov's method is a shock-capturing method, being first order, it will correspondingly only give first order of accuracy for smooth solutions and smeared approximations to discontinuities. Higher-order Godunov-type methods have been used successfully for many years to solve different problems in compressible fluid dynamics. The best representative of this class of schemes is the one developed by Colella and Woodward (1984), the Piecewise Parabolic Method (PPM). This method is a second-order accurate method (in space and in time). The principal difference is that left and right states, which are used for the Riemann problem, are constructed by interpolation using data from 4 neighboring zones on each side of the cell edge. The PPM method has been widely used to study different astrophysical gas dynamics problems, like supersonic compressible convection (Malagoli *et al.* 1990; Porter and Woodward 1994; burning convective shells (Arnett, 1994); thermonuclear burning in novae (Kercek, Hillebrandt and Truran 1998 (KHT)), Kelvin-Helmholtz instabilities in jets (e.g. Rossi *et al.*, 1997), galactic cooling flows (Kritsuk, Bohringer and Müller 1998) e.t.c. To perform our hydrodynamical simulations of the stream-core interactions we use as basis the Munich PPM hydro-code PROMETHEUS (Fryxell, Müller and Arnett 1989). This code has been already widely used by different groups (see, e.g. KHT; Kritsuk, Bohringer and Müller 1998; Nelson *et al.* 1994; Ruffert, Rampp and Janka 1997; Ruffert and Janka 1998, 1999). The code has been verified for most the classical tests (the Sod problem, interactive blast waves, double Mach reflection), therefore we do not provide the results of tests here.

To make the code applicable to our problem, we made a number of modifications to the original code, in particular to the treatment of the gravity field, the boundary conditions, to the equation of state and the hydrodynamical equations themselves (to take into account the effects of a frame co-rotating with the binary).

In the presence of a large pressure gradient at the core–envelope interface and a correspondingly strong gravitational field, Godunov-type schemes produce intrinsic accelerations, which during a few dynamical timescales $t_{\rm d}$ create significant outward motion (KHT). For a first-order Godunov method it is possible to find an analytical formula to modify the interface states. Then source terms (the gravitational field in our case) will be balanced by flux differences (LeVeque 1998). This is not possible for higher-order Godunov-type schemes, where each problem requires a separate treatment (KHT). To reduce the artificial acceleration in our case, we assume that the gravitational field can be considered as constant in time and that there is no self-gravity. Then, in each time step, we modify the interface values before applying the Riemann solver, by reducing them from both (left and right) interfaces by a pressure flux caused by gravity. Furthermore, we enforce the condition of hydrostatic equilibrium at the boundary (for ghost cells[1]) in the direction of the gravity

[1]Ghost cells are a few additional cells (four in the case of a PPM code) at each boundary of the computational domain, where the values at these cells are determined by the boundary conditions.

field. These modifications ensure that any initial model remains stable for arbitrarily long time.

The original equation of state (EOS) was for the case of constant adiabatic index γ. The EOS in the code now is for the mixing of the fully ionized ideal gas and radiation. Also, the EOS in the case of a degenerate gas can be used optionally, but since calculations where the degeneracy is taken into account are costly, we normally did not use it.

In calculations where nuclear burning is included, we use a nuclear reactions network with 35 isotopes, which includes all important reactions up to ^{25}Mg, in particular all α reactions and the complete hot (β-limited) CNO cycle. The reaction rates were taken from the Thielemann nuclear reactions library (provided by R. C. Cannon) The changes in chemical composition and the energy density due to the nuclear burning are updated after each time step in the hydrodynamical calculation.

4.1.2 The model set-up

We performed 2-dimensional calculations in polar cylindrical coordinates, where we usually used 300×300 grid points. In the case of very narrow streams, we increased the resolution to 600×600 grid points. We also carried out test calculations with grids of higher resolution to satisfy ourselves that further increasing the number of grid points does not significantly affect the results. As a general rule, we ensure that the inflowing stream contains at least 20 grid points in the azimuthal direction. We also carried out a few 3-dimensional calculations (in spherical coordinates) for the case of a symmetrical (non-inclined) stream in a non-rotating frame. The results of these calculations showed that there were no significant differences between the 2- and 3-dimensional calculations with the same initial parameters. In particular, the penetration depths of the stream were very similar in both cases.

Ambient matter

To model the region of interest for the stream–core interaction inside the common envelope, we adopt power-law distributions for the temperature and the pressure, i.e $T(r) = T(r_0)\,(r_0/r)^{\alpha_T}$ and $P(r) = P(r_0)\,(r_0/r)^{\alpha_P}$. We fitted these power laws to the structure in actual CE calculations. Typical values for α_T and α_P are in the range $(1.3; 5.2) \div (0.8; 3.2)$, but can be as high as $(1.7; 7)$ (corresponding to a structure with an adiabatic index $\gamma_{\rm amb} \approx 1.44$) and reasonably describe the regions of the stellar models at the the evolutionary stage of interest (see Fig.4.1). For our calculations here, we adopted parameters $(\alpha_T; \alpha_P) = (1.3; 5.2)$ and $(0.8; 3.2)$ for models representing a 20+1 and a 20+5 CE simulation, respectively. Throughout the domain of our calculations, we assume that the ambient matter has a constant composition, similar to the composition in the core region of the primary, mainly helium. In the full stellar models, hydrogen is exhausted below a radius of 4×10^{10} cm, and the hydrogen mass fraction increases to ~ 0.1 at the outer edge of the domain (at 7.5×10^{10} cm). We have tested that these differences do not affect the results appreciably. In this parametrized model, we assume that the ambient matter is initially in (quasi-)hydrostatic equilibrium; as the model is parametrized by the pressure and temperature gradient, the gravitational field is then defined implicitly by the initial pressure gradient of the frame and the initial density distribution. In calculations with nuclear burning, to prevent nuclear burning in the ambient medium, we assumed that the ambient medium contained neither H nor He in these particular calculations.

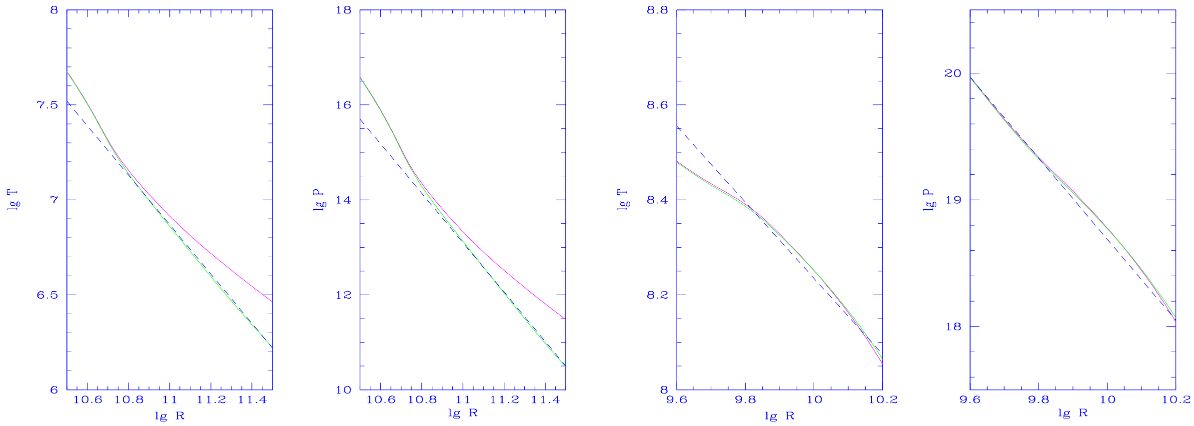

Figure 4.1: The temperature and pressure profiles in the region of the interest for the primary of $20M_\odot$ (before spiral-in and after spiral-in of a secondary of $5M_\odot$). Left figure : $(\alpha_T; \alpha_P) = (1.3; 5.2)$ and at the right figure $(\alpha_T; \alpha_P) = (0.8; 3.2)$.

Boundary conditions

The boundary conditions in the code, which describe the characteristics of the inflowing stream, are the internal and external Mach numbers, $M_{\rm int}$ and $M_{\rm ext}$; the ratio between the central density in the stream and the ambient density at the outer boundary η_ρ; the initial inclination angle of the stream θ (i.e. the angle between the initial flow direction and the direction of the primary). For the chemical composition of the gas in the stream we use the abundances of the secondary.

The boundary conditions for the rest of the box in the radial direction are outflow boundaries (except in the gas inflow zone) where the condition of hydrostatic equilibrium has been imposed for ghost cells. The boundary condition in the azimuthal direction also assumes outflow conditions (we used a grid which normally covers an angle π). As Courant number we used $N_{\rm CFL} = 0.6 \div 0.8$. A further parameter is the angular velocity with which the coordinate system rotates (most calculations were performed in the frame rotating with the primary core).

4.2 Interaction between the stream and the ambient matter

4.2.1 The initial stream-core interaction: establishing a steady stream

Figure 4.2 shows the initial interaction of a stream with a massive core and illustrates the development of a stationary stream. The parameters for this simulation are characteristic for a $1\,\mathrm{M}_\odot$ star filling its Roche lobe inside the envelope of a very evolved $20\,\mathrm{M}_\odot$ red supergiant (after helium core burning). The panels on the left show the hydrogen abundance, while the panels on the right show the divergence of the velocity field. The latter was chosen because it shows shock structures particularly clearly.

The top panels show the stream just before its 'impact' with the core (569 s after the beginning of the simulation), while the second set of panels is close to the point of impact (at 778 s; note the bow shock in the right panels). Immediately after the impact, stream matter bounces off the core, where most of it is just reflected by the core and continues to move in the forward direction (i.e. counter-clockwise), but some of it is pushed backwards, attaining an angular velocity component opposite to the rotation of the core. As material that has been stopped by the core is pushed by material in the stream following from behind, it starts to flow up again, driving two powerful shocks on the front and back side of the stream into the envelopes. These shocks compress the stream significantly. Once they have left the domain of the calculation, the stream has attained essentially a stationary configuration, where the point of deepest penetration ($R \simeq 2 \times 10^{10}$ cm) and the stream shape no longer change significantly. The overall flow pattern also becomes more-or-less stationary, where all the matter leaving the stream in the core impact region flows up again, being vigorously mixed with helium from the core in the process. For more details see Appendix E and the CD-ROM.

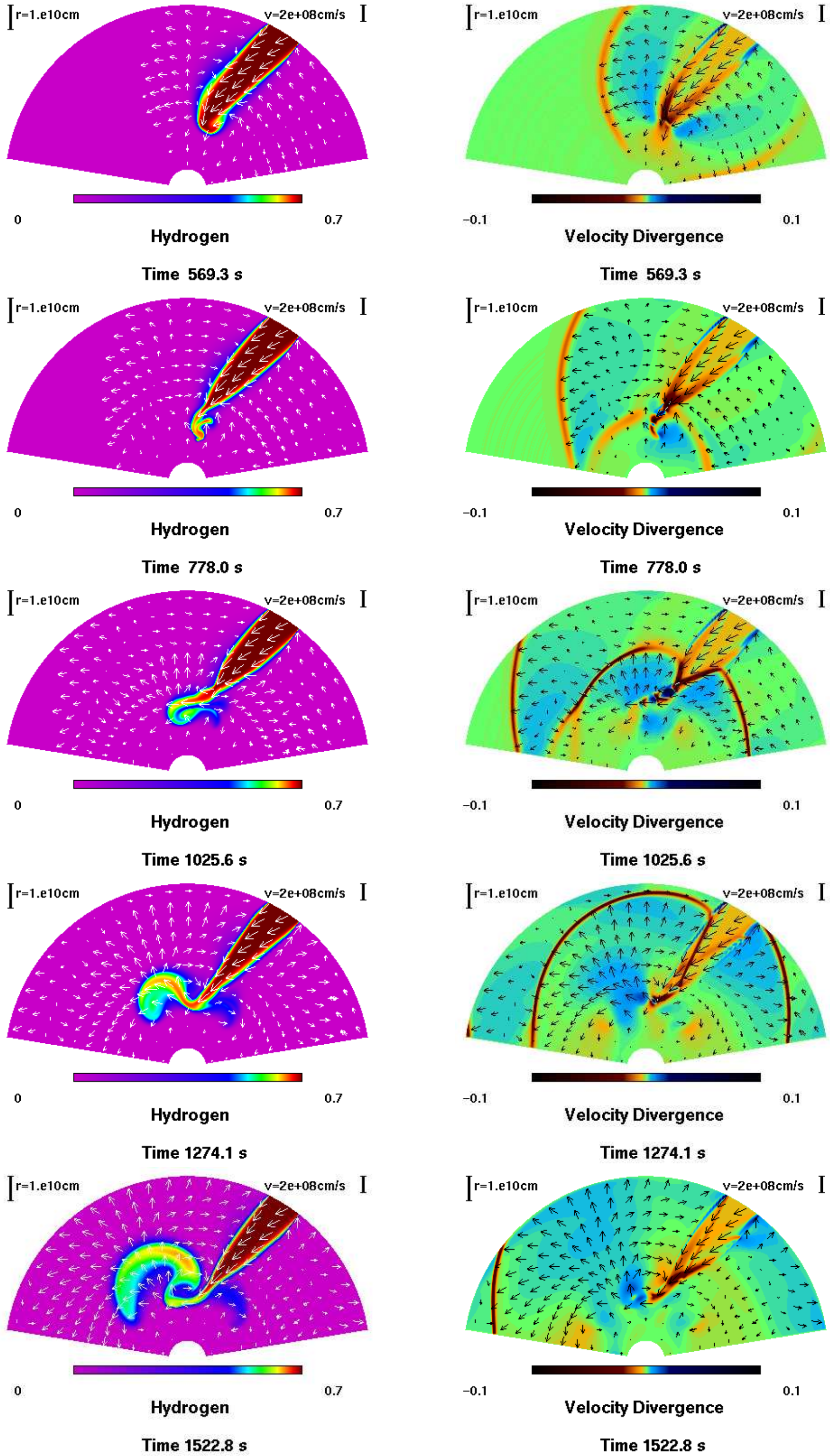

Figure 4.2: The initial stream-core interaction and the establishment of a steady stream in a frame rotating with the core (with an angular velocity $\Omega_{\rm frame} = 4 \times 10^{-4}\,{\rm rad\,s^{-1}}$). The left panels show the distribution of hydrogen, the right panels the distribution of $\boldsymbol{\nabla} \cdot \boldsymbol{v}$. The initial Mach numbers in the stream, $M_{\rm int}$, and ambient medium, $M_{\rm ext}$ are 8.5 and 3.2, respectively, the density ratio between the stream and the ambient medium, $\eta_\rho = 8$, the outer radius $R_{\rm T} = 7.5 \times 10^{10}$ cm, the angular radius of the stream $R_{\rm s} = 0.03\pi$ and the initial stream inclination with respect to the radial direction $\Theta = 13.5^{\rm o}$. The velocity field is scaled according to $\log(v/10^6\,{\rm cm\,s^{-1}})$.

4.2.2 Mechanisms for stream dissipation

The main objective of our calculation is to determine how deep the stream can penetrate into the core of a massive star rather than the initial transient behaviour. In the quasi-stationary situation this depends mainly on the entropy that is generated in the stream-core interaction.

Pressure discontinuity and entropy generation

While the stream is in lateral pressure balance with the ambient matter at an early stage of infall, it becomes increasingly unbalanced as the velocity increases and becomes significantly supersonic relative to the ambient medium. The interaction between the stream and the ambient matter due to the jump in pressure can be treated in a simplified way as a Riemann problem, a solution of which is a combination of shock and rarefaction waves. In the case where the stream expands, the rarefaction wave, propagating into the stream material, does not change the stream entropy. However, compression of the stream by the ambient matter, in the form of shocks moving into the stream, generates entropy inside the shocks.

For a strong shock, where the pressure jump $P_{\rm amb}/P_{\rm s} \gg 4$, the coefficient of entropy change, i.e. the ratio of the entropy of the shocked stream material, $S_{\rm ss}$, to the initial entropy in the stream, $S_{\rm s}$, can be estimated as

$$K_{\rm S} = \exp((S_{\rm ss} - S_{\rm s})/c_V) = \frac{P_{\rm ss}}{P_{\rm s}} \left(\frac{\rho_{\rm ss}}{\rho_{\rm s}}\right)^{\gamma} \approx \text{const} \cdot P_{\rm amb}/P_{\rm s} \tag{4.7}$$

(Zeldovich and Raizer 1966).

In our case, we rather expect the development of weak shocks. Then an estimate for $K_{\rm S}$ can be written as

$$K_{\rm S} \approx 1 + \text{const} \cdot \eta_\rho^{\gamma-1} \left(\frac{M_{\rm int}}{M_{\rm ext}}\right)^2 (P_{\rm amb}/P_{\rm s} - 1)^3 \, , \tag{4.8}$$

The pressure jump $P_{\rm amb}/P_{\rm s}$ changes with the distance to the primary core. In the case of a power-law parametrisation of the ambient pressure, equation (4.8) predicts that models with smaller power-law indices will result in smaller pressure jumps for the same initial stream properties and hence smaller values for $K_{\rm S}$ and that this coefficient increases as the power-law index increases.

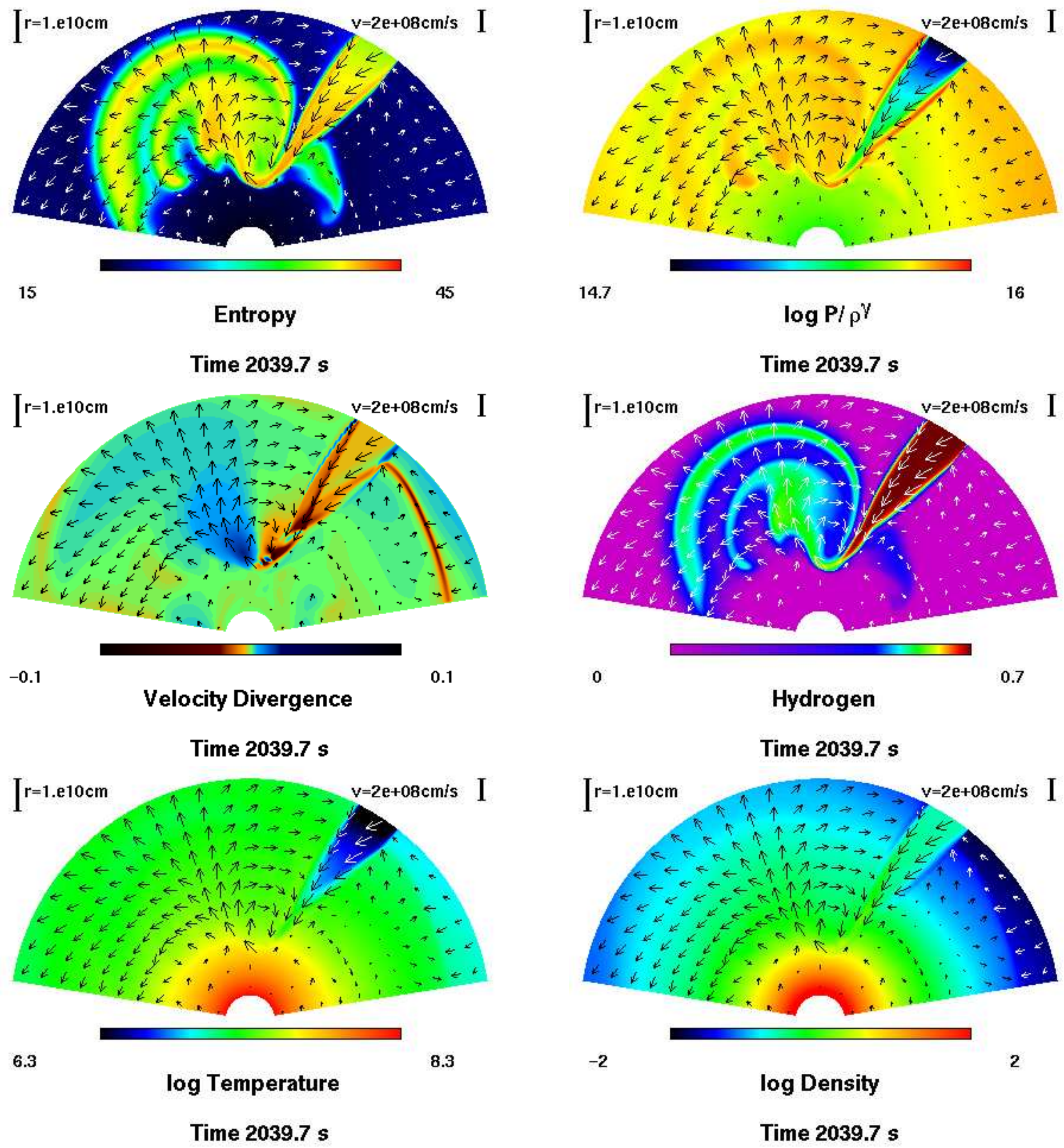

Figure 4.3: Characteristic properties (entropy, $\log P/\rho^{\gamma}$, divergence of velocity, hydrogen mass fraction, density and temperature) for a stationary inclined stream (with the same parameters as in Fig. 4.2). The radius of deepest penetration is 2.0×10^{10} cm in the simulation. At that depth the temperature in the stream is 6×10^{7} K and the density $3\,\mathrm{g\,cm^{-3}}$.

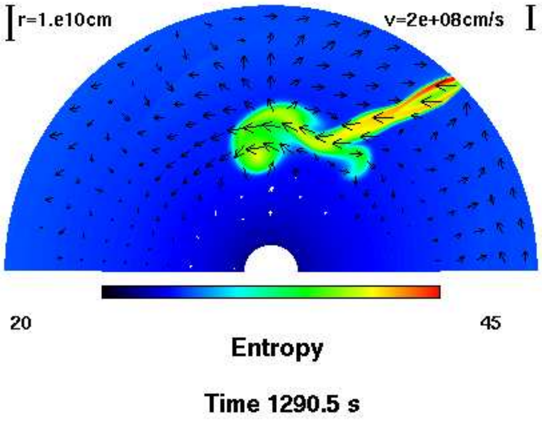

Figure 4.4: Example of a Kelvin-Helmholtz instability experienced by a narrow stream with $R_{\rm s} = 0.005\pi$. ($M_{\rm int} = 8$, $M_{\rm ext} = 3.25$, $\eta_\rho = 8$, $R_{\rm T} = 7.5 \times 10^{10}$cm, $\Omega_{\rm frame} = 4 \times 10^{-4}\,{\rm rad\,s^{-1}}$, $\Theta = 18^{\rm o}$.) The stream penetrates to a depth of 2.7×10^{10} cm.

In Figure 4.3 we present some of the key characteristics of a stream with the same parameters as in Figure 4.2, once a more-or-less stationary flow pattern has been established. Note in the top two panels that the entropy in the core of the stream is initially constant and that all the entropy generation takes places in two strong shocks at the stream boundaries (clearly seen in the $\boldsymbol{\nabla} \cdot \boldsymbol{v}$ panel). All of the stream matter has to pass through the intersection of these shock structures, where it essentially attains its final entropy and becomes comparable to the entropy of the ambient material, at least in the case of the $\log P/\rho^\gamma$. For the entropy the difference between ambient and stream matter is largely caused by the difference in molecular weights and its subsequent change is due to mixing of these two media rather than dissipation. At the point of deepest penetration ($\sim 2 \times 10^{10}$ cm), the stream matter has a temperature of 6×10^7 K and a density of $\sim 3\,{\rm g\,cm^{-3}}$, high enough for nuclear burning (see § 5.4).

Kelvin-Helmholtz instabilities and the stream width

The boundary between the jet material and the ambient matter is subject to a tangential discontinuity which is generally unstable for compressible fluids for any relative velocity (Landau and Lifshitz 1959). In the case, where two horizontal parallel streams with densities ρ_1 and ρ_2 move relative to each other with relative velocity $v_{\rm r}$, the growth rate of this Kelvin-Helmholtz (K-H) instability for wavenumber k is given by

$$\mathrm{Im}\,\omega = k v_{\mathrm{r}} \frac{\sqrt{\rho_1 \rho_2}}{\rho_1 + \rho_2} \tag{4.9}$$

(Landau and Lifshitz 1959).

In the case where gravity is included, the condition for instability becomes

$$k > \frac{|\rho_2^2 - \rho_1^2| g \sin\theta}{\rho_2 \rho_1 v_{\mathrm{r}}^2}\,, \tag{4.10}$$

where g is the gravitational acceleration and θ is the angle between the relative velocity and gravity. A simple estimate shows that, even for an inclined stream, the stabilizing effect of gravity is small and that the stream is unstable to this instability on all length scales of interest. The K-H instability affects both the stream shape and the stream width. For small relative velocities, the stream is "sausage"-shaped and becomes increasingly "snake"-shaped as the relative velocity increases (see Fig. 4.4). The Kelvin-Helmholtz instability implies that perturbations on a length scale smaller than some critical wavelength become non-linear. It becomes more important as the stream narrows, since perturbations of a given wavelength are more important for a narrower flow. It therefore determines the minimum stream width and thus limits the depth of penetration. In particular, a stream that is very narrow initially will penetrate less deep than a stream with a similar parameters like velocity, density and pressure, but with a larger mass-flow rate and hence larger initial stream width.

4.2.3 The effects of rotation

A rotating medium

In some cases, in particular near the end of the merging process, the envelope surrounding the spiraling-in components may no longer remain in co-rotation with the binary (either because the spiral-in timescale becomes too short or the region surrounding the primary core expands rapidly). Then the stream feels an additional force due to the moving external medium. This affects the stream's trajectory, in particular the angle of incidence, and thereby the penetration depth. This is illustrated in Figure 4.5 which shows two stream calculations with the same parameters as in Figure 4.3 but where the medium is assumed to rotate with an angular velocity $\Omega_{\mathrm{shift}} = 10^{-4}\,\mathrm{rad\,s^{-1}}$ relative to the frame of the binary (rotating with angular velocity Ω) either in the forward or in

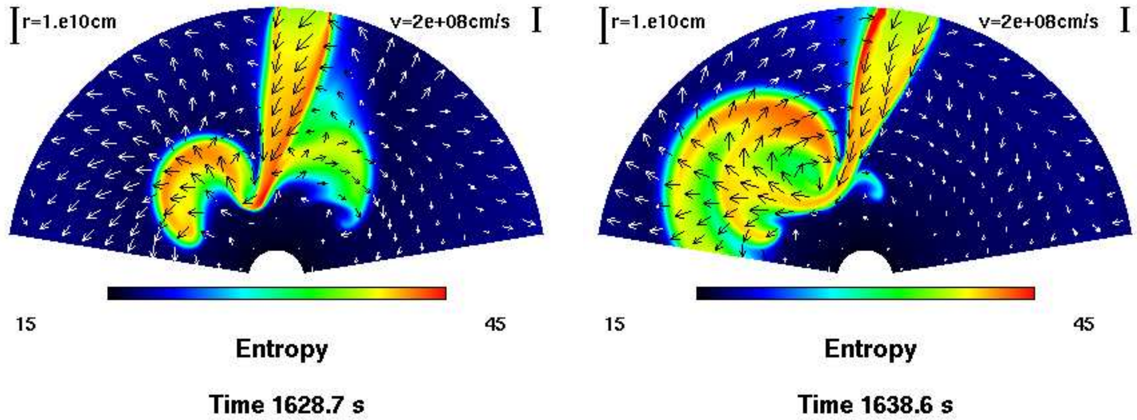

Figure 4.5: Examples for streams penetrating into a medium rotating relative to the binary. The stream rotates in an anti-clockwise and a clockwise direction relative to the medium in the left and right panels, respectively, with a relative velocity $\Omega_{\rm shift} = 10^{-4}\,{\rm rad\,s^{-1}}$. The initial positions of the stream centre in the azimuthal direction were taken to be 0.3π and 0.6π in the two cases, respectively. The other stream parameters are the same as in Figure 4.3 ($M_{\rm int} = 8.5$, $M_{\rm ext} = 3.2$, $\eta_\rho = 8$, $R_{\rm T} = 7.5 \times 10^{10}\,{\rm cm}$, $R_{\rm s} = 0.03\pi$, $\Omega_{\rm amb} = 4 \times 10^{-4}\,{\rm rad\,s^{-1}}$, $\Theta = 13.5^{\rm o}$). The radii at the point of deepest penetration are 1.75 and 2.25×10^{10} cm, respectively.

the backward direction. The frame of the medium (in which the calculation is performed) then rotates with a velocity $\Omega_{\rm amb} = \Omega \pm \Omega_{\rm shift}$. In this frame, the stream itself rotates either anti-clockwise (top panel) or clockwise (bottom panel). As the stream is being pushed backwards by ambient matter moving against its direction of rotation, its trajectory steepens and consequently the penetration depth increases (top panel), while the opposite happens when the stream is pushed from behind (bottom panel). As a consequence the stream penetrates deeper to a radius of $\sim 1.75 \times 10^{10}$ cm instead of $\sim 2 \times 10^{10}$ cm in the standard case (Fig. 4.3), while it only reaches a depth of $\sim 2.25 \times 10^{10}$ cm in the opposite case. The corresponding change in the stream temperature at the deepest point is only a few per cent. Note also that for the stream rotating anti-clockwise, the entropy generation at the back side of the stream, where the dynamical pressure is smaller than at the front side (and hence has a larger jump in pressure), is larger than for stationary inclined stream.

Core rotation

As the stream interacts with the core, it injects not only matter but also angular momentum into the core, spinning it up in the process. Since the core only has to accrete a small fraction of the angular momentum available from the secondary to be spun up to critical rotation, we may expect that this itself will affect the dynamics of the interaction. To demonstrate this, we performed four

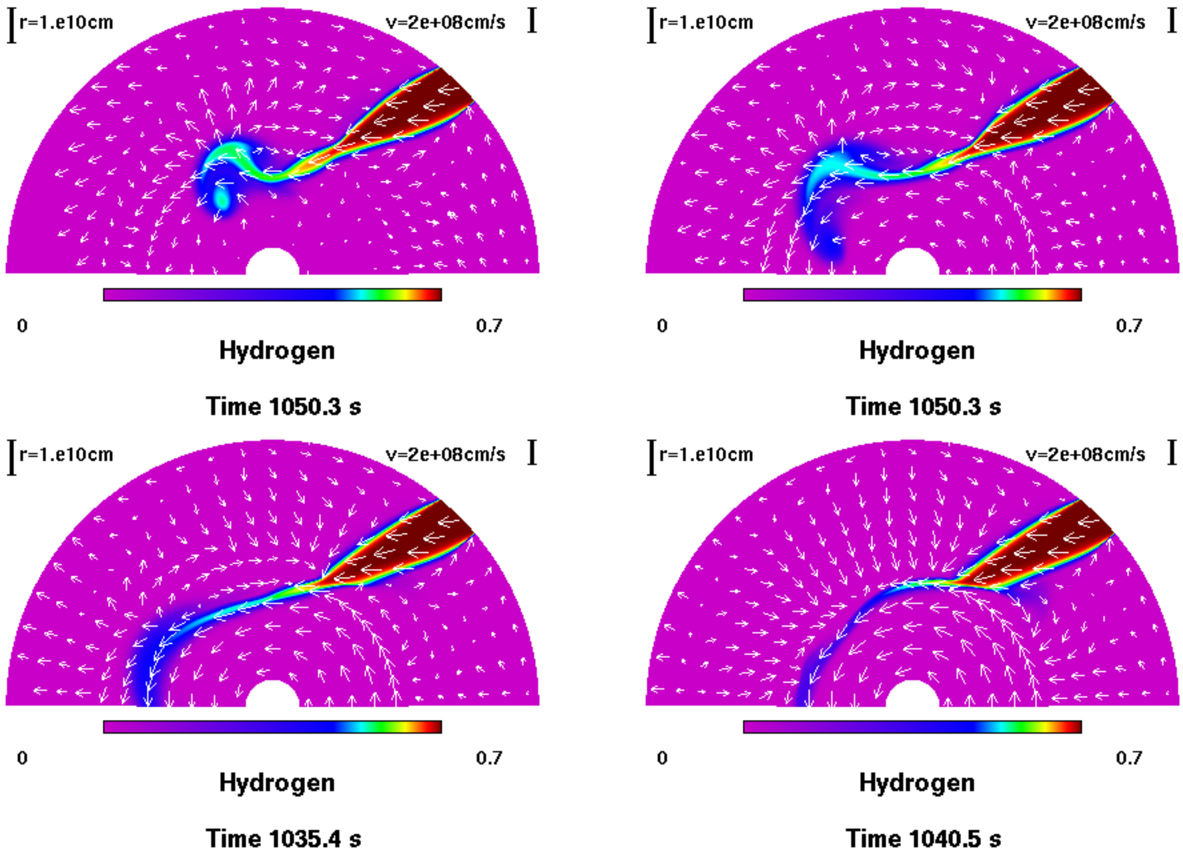

Figure 4.6: Stream simulations illustrating the effects of rotation of the primary core (in a frame rotating with the binary). In the four calculations, the core is assumed to rotate with constant angular velocities of $\Omega_{\rm core} = 0$ (top left), 0.001 (top right), 0.0025 (bottom left) and $0.005\,{\rm rad\,s}^{-1}$ (bottom right), respectively, up to a radius 4×10^{10} cm. The other stream parameters are $M_{\rm int} = 9.8$, $M_{\rm ext} = 3.7$, $\eta_\rho = 8.4$, $R_{\rm T} = 7.5^{10}$ cm, $R_{\rm s} = 0.025\pi$, $\Theta = 18^{\rm o}$.

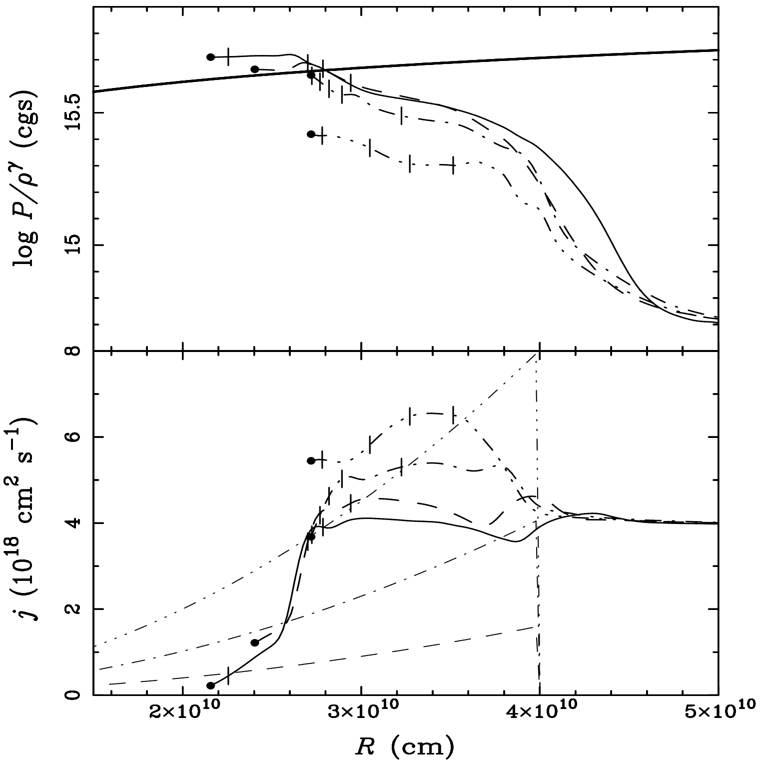

Figure 4.7: The logarithm of the adiabatic constant ($s = P/\rho^{\gamma}$, top panel) and specific angular momentum (bottom panel) near the centre of the streams as a function of penetration depth for the simulations in Figure 4.6 with angular velocities $\Omega = 0$ (solid curves), 0.001 (dashed curves), 0.0025 (dot-dashed curves) and $0.005\,\mathrm{rad\,s^{-1}}$ (dot-dot-dot-dashed curves). The corresponding angular-velocity profiles for the ambient core matter are shown in the bottom panel as lighter curves with the same line style. The thick solid curve in the top panel refers of $\log s$ in the ambient matter. The filled circles at the end of individual curves mark the points of deepest penetration. The ticks along each curve indicate particular values of the central stream hydrogen abundance by mass (0.6, 0.5, 0.4, 0.3 from right to left).

simulations for streams with the same initial parameters and similar core properties except that we varied the rotation of the core from 0 to $0.005\,\mathrm{rad\,s^{-1}}$ within a core radius of $4 \times 10^{10}\,\mathrm{cm}^2$. The results of these simulations are shown in Figures 4.6 and 4.7.

As Figure 4.6 shows, the core–stream interaction changes qualitatively and quantitatively, where the penetration depth decreases with increasing core rotation. In the case of a rapidly rotating core, the penetration depth is centrifugally limited (i.e. by the angular momentum in the stream). In Figure 4.7 we show the logarithm of the adiabatic constant and the specific angular momentum near the center of the streams in the four simulations as a function of radius. In the two

[2] Note that these cores are not completely comparable, since we assumed that the ambient core matter was in quasi-static dynamical equilibrium and had the same pressure and temperature distributions in all cases. This implies slightly different gravitational accelerations (and hence different core masses).

simulations with no or slow core rotation (solid and dashed curves), the stream's angular velocity is efficiently being braked below a radius 2.6×10^{10} cm by its interaction with the core and reaches the deepest point of penetration (marked as filled circles) where the adiabatic constant is comparable to the ambient one. The specific angular momentum is always substantially less than the local critical angular momentum for centrifugal support, given by $\sqrt{gR^3}$, where g is the gravitational acceleration at radius R. On the other hand, in the two cases with rapid core rotation (dot-dashed and dot-dot-dot-dashed curves), the stream is first accelerated in the azimuthal direction by the interaction with the core, in fact reaching an angular velocity that is larger than the local velocity of the core (even though the initial angular velocity at the core boundary was less). At the point of deepest penetration, the specific angular momentum is close to the critical angular momentum, and hence the stream becomes centrifugally supported. Note also that, in this case, the stream does not bounce but starts to form a ring orbiting the core and gradually mixing with it. This demonstrates that the main effect of rapid core rotation is to *prevent/reduce* the azimuthal braking of the stream. While this leads to less entropy generation in the stream (see the top panel in Fig. 4.7), which ordinarily would mean that the stream should be able to penetrate deeper, it makes the angular momentum of the stream itself a key factor in limiting the penetration depth. In the simulation with the fastest core, the stream matter is still substantially denser than the ambient matter at the final point shown in the simulations. Since it is also rotating faster than the local core material, it is reasonable to expect that the stream will continue to spiral in as it is being braked by the ambient medium and will penetrate somewhat deeper than is shown in the figures. (We were unable to follow the subsequent evolution since the stream matter was leaving the domain of the calculation at this point.)

Even in the case where the core is non-rotating, the specific angular momentum in the stream increases during a portion of its trajectory (see the solid curve in the bottom panel between 3 and 3.8×10^{10} cm). This is a direct consequence of the stream splitting into two components in the impact region, a forward and a backward component (this can be seen more clearly in Fig. 4.5). As matter in the forward component is pushed by matter following from behind, it is being accelerated and gains angular momentum, while matter flowing backwards attains negative angular momentum.

Finally, note that because of the narrower stream in the post-impact region of the more rapidly rotating core, stream material mixes more efficiently with the core material (Fig. 4.6 and 4.7). This

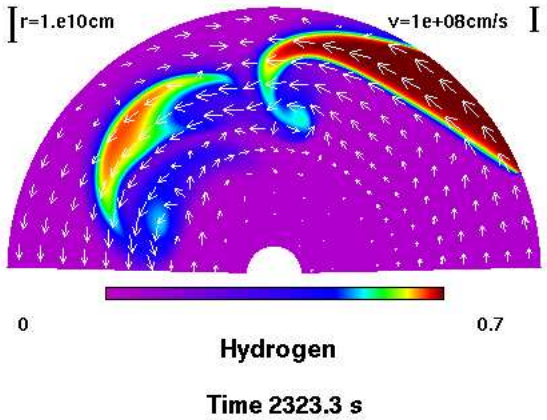

Figure 4.8: Stream simulation illustrating the effects of a large, initial inclination angle with $\Theta = 45°$. ($M_{\rm int} = 5.6$, $M_{\rm ext} = 2.2$, $\eta_\rho = 8.$, $R_{\rm T} = 7.5 \times 10^{10}$ cm, $R_{\rm s} = 0.03\pi$.)

Table 4.1: Dependence of penetration depth on initial inclination angle.

Θ	$X = 0.2$	$X = 0.4$	$X = 0.5$	$X = 0.6$
9	2.0×10^{10}	2.3×10^{10}	2.5×10^{10}	3.2×10^{10}
18	2.0×10^{10}	2.3×10^{10}	2.5×10^{10}	3.3×10^{10}
27	2.5×10^{10}	2.6×10^{10}	2.9×10^{10}	3.5×10^{10}
36	2.5×10^{10}	2.8×10^{10}	3.3×10^{10}	3.7×10^{10}
45	2.7×10^{10}	2.7×10^{10}	3.3×10^{10}	4.2×10^{10}
54	2.8×10^{10}	2.8×10^{10}	3.2×10^{10}	5.0×10^{10}

Note. – Θ: initial stream inclination. The different columns show the depth of deepest penetration (in cm) for material in the stream with different hydrogen mass fractions X, as the stream penetrates into the core and mixes with core material.

may have important consequences for the nucleosynthesis in this region (see § 4.2.4).

4.2.4 The inclination angle and the penetration depth

The penetration depth also depends on the inclination angle of the stream, which in turn is determined by the initial stream angular momentum and the ballistic trajectory of the stream before its impact with the core (see Fig. 3.3). To investigate this dependence, we performed a set of simulations for streams with parameters $M_{\rm int} = 5.6$, $M_{\rm ext} = 2.2$, $\eta_\rho = 8.$, $R_{\rm T} = 7.5^{10}$ cm, $R_{\rm s} = 0.03\pi$, where we varied the initial inclination angle systematically: $\Theta = 9°$, 18°, 27°, 36°, 45°, 54°, respectively. In the first two cases, the initial specific angular momentum, j_0, is smaller than the local critical angular momentum j_c, for which a stream could be centrifugally supported, for most of the domain of the calculation, while in the other cases j_0 becomes larger than j_c at radii $r_{\rm centr} = 1.2 \times 10^{10}, 2.6 \times 10^{10}, 4.1 \times 10^{10}, 6.0 \times 10^{10}\,$cm, respectively.

As soon as the stream starts to interact strongly with the core, it also begins to mix with core material. Hence, as the stream penetrates deeper, its hydrogen mass fraction decreases. In Table 4.1 we present the depth of deepest penetrations in these simulations for stream material with different hydrogen mass fractions ($X = 0.2, 0.4, 0.5, 0.6$), once a steady-state stream has been established. In the two cases with the largest inclinations (i.e. $\Theta = 45^{\rm o}, 54^{\rm o}$), a true steady state is never properly established since the mixing process exhibits a burst-like behaviour (see Fig. 4.8) after the stream has lost most of its specific angular momentum.

The most important result of these simulations is that the streams can efficiently lose their angular momentum once they interact strongly with the core. Figure 4.8 shows a typical example for a large initial inclination ($\Theta = 45^{\rm o}$). The stream loses most of its angular momentum by the time it reaches a radius of 4×10^{10} cm. Since it is still denser and has a lower adiabatic constant than the ambient medium, it continues to sink, increasingly mixing with the ambient material. In general, the point of deepest penetration is determined by the condition that the adiabatic constant of the mixed stream material becomes comparable to the ambient adiabatic constant. However, in practice only a small amount of stream material reaches the deepest point (i.e. regions where $X = 0.2$, 0.4). Most of the stream material is mixed with the ambient medium at a larger radius (the detailed behavious depends strongly on the initial inclination).

Overall, we can conclude that the dependence on the inclination angle is rather weak and that in general the penetration depth is mainly a function of the stream entropy and the initial velocity, unless the angular momentum in the stream is so large that it becomes centrifugally supported before it can strongly interact with the core.

4.2.5 The effects of nuclear burning

One of the objectives of our study is to investigate the nucleosynthesis in the stream material after it has been heated by its impact with the core of the primary. The associated heating by nuclear burning itself may then affect the hydrodynamics of the stream. As can already be seen from the

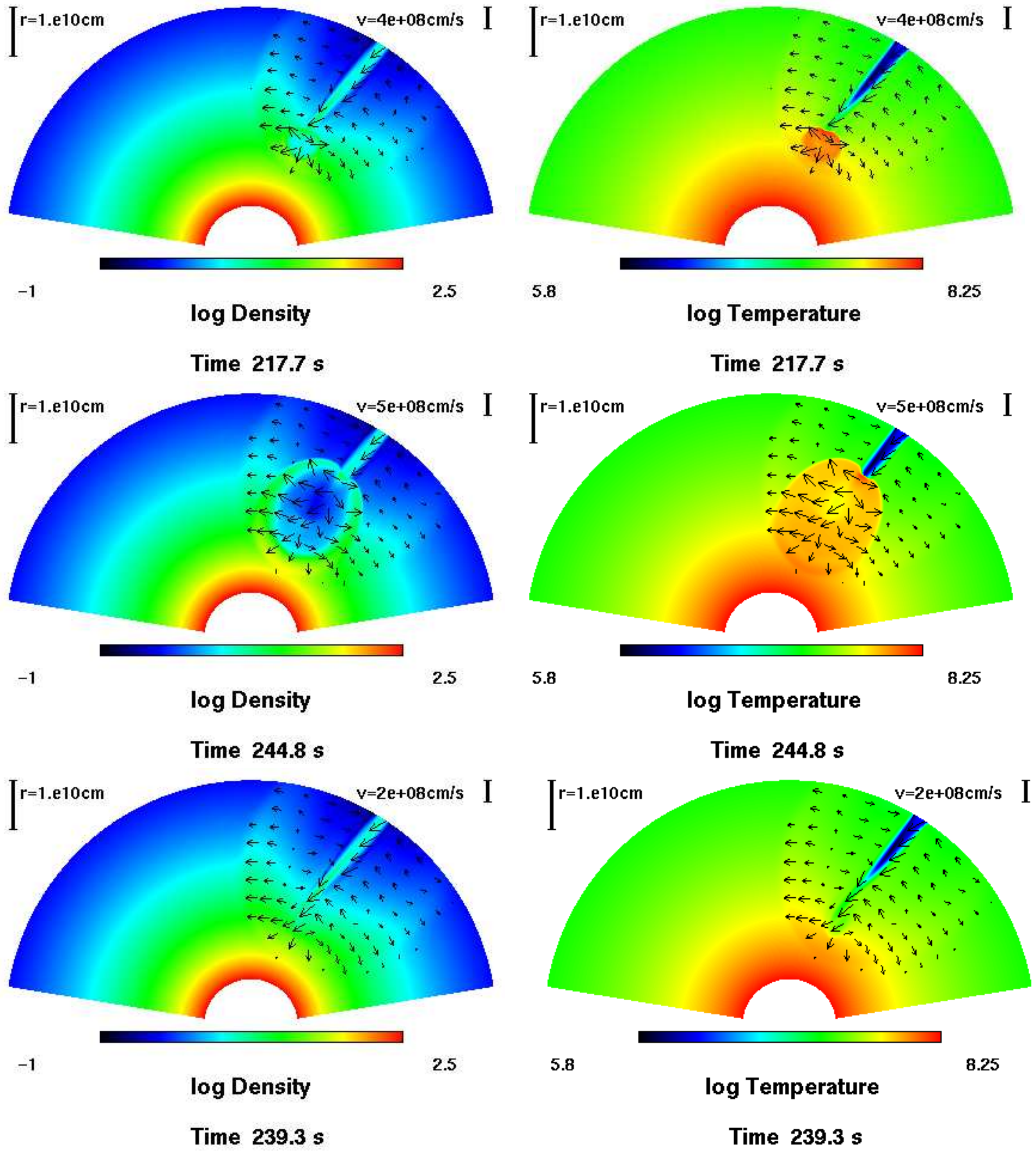

Figure 4.9: Density and temperature distributions for stream simulations illustrating the effect of violent nuclear ignition. The top two panels show the stream just before impact with the core and the point of nuclear ignition. The middle two panels show the detonation wave that develops shortly after nuclear ignition that disrupts the inflowing stream. The bottom two panels show a stream at the same time if nuclear burning is not included for comparison. The stream parameters are $M_{\rm int} = 9.9$, $M_{\rm ext} = 4.$, $\eta_\rho = 7$, $R_{\rm T} = 5 \times 10^{10}$ cm, $R_{\rm s} = 0.03\pi$, $\Theta = 10^{\rm o}$.

simulations presented so far, the characteristic timescale for the stream infall is of order $1000\,\mathrm{s}$, where the stream material typically spends no more than $50 - 100\,\mathrm{s}$ near the impact region before it bounces or forms a ring orbiting the core (in the case of a fast rotating core). Nuclear burning can only affect the stream motion if the characteristic timescale for nuclear burning is of order or shorter than the stream dynamical timescale. For the largest part of the stream trajectory, the stream material is relatively cold (for the range of stream models considered).

Nuclear burning only starts to increase dramatically after it has been heated to a temperature comparable to the ambient temperature, which occurs suddenly in the region of impact. However, since the characteristic nuclear timescale is generally longer than the local dynamical timescale, stream material will have already moved far away from the region of impact and hence have little effect on the stream dynamics (in the pre-impact region) and the stream trajectory. It mainly affects the properties of the ambient matter (its composition and temperature) and hence the background conditions for the stream on a timescale that is long compared to the stream infall timescale, so these effects and the associated nucleosynthesis can be followed with a standard stellar evolution code.

The situation can be different when the stream impacts the core more-or-less radially and when the core has a very steep density gradient, causing a very strong shock and hence very high post-shock temperatures. This can cause a nuclear runaway as illustrated in Figure 4.9. As the middle panels in this figure show, it triggers a detonation wave that propagates up into the stream, almost completely disrupting it in the process. The expansion wave propagating into the ambient medium causes a dramatic expansion of the envelope material. Once all of the matter burning in this runaway has been consumed, one may expect that the stream re-establishes itself and that the process repeats, leading to pulsed nuclear burning. For more details see Appendix E and the CD-ROM.

4.3 The penetration depth

4.3.1 The entropy change

In the idealized case of a stream of constant entropy, the depth of penetration can easily be estimated from the balancing of the stream ram pressure with the ambient pressure. In our case, the pressure of the stream material becomes comparable to the ambient pressure well before the stream reaches its deepest point. In this case it is better to use an estimate based on the conservation of the Bernoulli integral for matter along a streamline (though both estimates would give similar results). However, since the stream entropy changes because of the compression by shock waves propagating into the stream from the sides, one has to use a modified Bernoulli integral to estimate the penetration depth. This is possible as long as the stream is wide enough that it is not strongly affected by the K-H instability and that core rotation plays a minor role.

For this purpose, we rewrite the Bernoulli integral for stream material in the form:

$$\Phi_{\rm T} + \frac{u_{\rm S,T}^2}{2} + \frac{c_{\rm S,T}^2}{\gamma_{\rm S,T} - 1} = \Phi_{\rm B} + \frac{u_{\rm S,B}^2}{2} + \frac{c_{\rm S,B}^2}{\gamma_{\rm S,B} - 1} \;, \tag{4.11}$$

where u is the velocity of stream material, c the sonic speed of the stream material and Φ the potential. The subscript S corresponds to matter in the stream, the subscript T refers to the initial conditions and the subscript B to the conditions at the point of deepest penetration. The point of deepest penetration can then be determined by the condition that the pressure of the stream is equal to the pressure in the ambient matter and that the final stream velocity is zero (consistent with the results of our hydrodynamical calculations).

For the stellar structure parametrized by the pressure gradient the corresponding potential can be written as

$$\Phi(r) = -\alpha_{\rm P}\frac{P(r)}{\rho(r)} = -\alpha_{\rm P}\frac{c_{\rm A}^2(r)}{\gamma_{\rm A}(r)} \;, \tag{4.12}$$

where the subscript A corresponds to the ambient matter at the initial point of the stream. Assuming that the entropy of the stream changes according to

$$\left(\frac{P}{\rho^{\gamma}}\right)_{\rm S,B} = K_{\rm S}\left(\frac{P}{\rho^{\gamma}}\right)_{\rm S,T} \;, \tag{4.13}$$

one can rewrite the Bernoulli integral to find $K_{\rm S}$ as a function of relative penetration depth, $\delta = r/r_{\rm T}$, and the initial conditions for the stream and ambient matter:

$$-\frac{\alpha_{\rm P}}{\gamma_{\rm A}} + \frac{M_{\rm ext}^2}{2} + \frac{M_{\rm ext}^2}{M_{\rm int}^2}\frac{1}{\gamma_{\rm S,T} - 1} \quad = \quad -\frac{\alpha_{\rm P}}{\gamma_{\rm A}}\frac{\beta_{\rm T}}{\beta(\delta)}\delta^{-\alpha_{\rm T}} + \tag{4.14}$$

$$\frac{1}{\gamma_{\rm A}}\frac{\gamma_{\rm S,B}}{\gamma_{\rm S,B}-1}\left(K_{\rm s}\eta_\rho^{1-\gamma_{\rm S,T}}\rho_{\rm A}^{-\gamma_{\rm S,T}}\frac{M_{\rm ext}^2}{M_{\rm int}^2}\frac{\gamma_{\rm A}}{\gamma_{\rm S,B}}\right)^{\frac{1}{\gamma_{\rm S,B}}}\rho_{\rm A}\delta^{\frac{1}{\gamma_{\rm S,B}}-\alpha_{\rm P}}.$$

Here $\rho_{\rm A}$ is the density of the ambient material at the initial radius of the steam, and β is the ratio of gas pressure to total pressure for the ambient matter.

4.3.2 Numerical fits

To determine the entropy change factor, $K_{\rm s}$, we performed sets of hydrodynamical simulations for two parametrized structures of the ambient medium, $(\alpha_{\rm P};\alpha_{\rm T}) = (5.2.1.3)$ and $(4.2;0.9)$, representing typical profiles in massive CE systems. We then calculated the stream penetration depth for 3 values of density ratios, $\eta_\rho = 2$, 10 and 30, and for a number of models with different Mach number ratios, $M_{\rm int}/M_{\rm ext}$ (where we varied $M_{\rm int}$, keeping $M_{\rm ext}$ fixed). All streams were calculated with an initial stream inclination of $18^{\rm o}$.

Using the expression for a weak shock (equ. 4.8), we fit the results to

$$K_{\rm s} = 1 + k(\alpha_{\rm P},\alpha_{\rm T})\cdot\eta_\rho^{\gamma-1}\left(\frac{M_{\rm int}}{M_{\rm ext}}\right)^2 . \qquad (4.15)$$

For an ambient medium, characterized by $\alpha_{\rm P} = 5.2;\ \alpha_{\rm T} = 1.3$, these results are well fitted by a constant $k = 0.45$ and for a structure with $\alpha_{\rm P} = 4.2;\ \alpha_{\rm T} = 0.9$ by $k = 0.1$ (see Fig. 4.10).

4.4 Conclusions

The purpose of this chapter was to study the physics of the stream interaction with the ambient matter (the core) at the stage when the secondary immersed in a common envelope starts to merge with the primary core. Our eventual aim was to find an easy way of obtaining the penetration depth of the stream for certain parameters to use in the evolutionary code.

We have systematically investigated how the penetration depth of a stream depends on the stream initial properties and on the core structure. The physical analog of the domain we used for calculations are an evolved 20 $\rm M_\odot$ supergiant and secondaries from 1 to 5 $\rm M_\odot$. Mainly we can conclude the following:

- The typical penetration depth is about few $\cdot 10^{10}$ cm, it is subsequently mixed over this region and heated up to the temperature $\geq 10^8$ K.

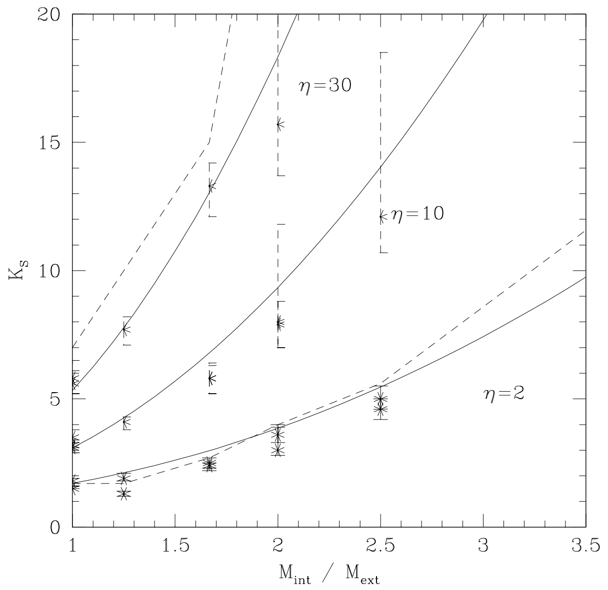

Figure 4.10: The entropy change as the function of the Mach numbers ratio for a parametrized ambient structure with $\alpha_{\rm P} = 5.2$ and $\alpha_{\rm T} = 1.3$. Asterisks correspond to values of $K_{\rm S}$ obtained from the hydrodynamical simulations by determining the appropriate value for $K_{\rm s}$ that would give the same penetration depth when using the Bernoulli integral as in the actual hydrodynamical simulation. The error bars are obtained by assuming an error in the determination of the penetration depth of 3 per cent. Solid curves correspond to the theoretical fit with $k = 0.45$, while the dashed curves show the change in entropy of the stream material in the hydrodynamical simulations.

- The entropy generation in the stream can be understood in terms of weak shocks developed due to the pressure discontinuity between the stream side and the ambient matter.
- Mass transfer rate do not affect on the entropy generation within the stream, but since narrow streams are unstable to a Kelvin-Helmholtz instability, for low mass loss rates the penetration depth is different.
- Slow asynchronous rotation of the primary core neighborhood respect to the binary orbital motion causes that in the weak non-corotating the penetration depth of the stream can be deeper.
- The case of a slowly rotating core is close to the no-rotating core, and the penetration depth mainly depends on the initial entropy and the entropy generated during in the interaction. In the result stream bounces off the core, expands and mostly mixes over the large region, higher than the penetration depth.
- A fast rotating core gives additional angular momentum to the stream and the stream penetration became centrifugal limited. As the result, the stream does not bounce off the core and forms centrifugically supported ring, slowly going down due to the mixing with the core material.
- In most cases the nuclear burning in the stream does not affect the structure and dynamics of the stream itself; it modifies the ambient matter at the time scale which is longer than the dynamical time for stream-core interactions. However, in the case of a very strong shock the shock-triggered nucleosynthesis can initiate a detonation wave. Models which have experienced this event normally have strong density gradient in the core and have approximately normal incidence. In this case not only the stream structure is disrupted, but also envelope expands dramatically.

As the result, using a simple model for the dissipation in a weak shock, we provided the empirical formula that allows the determination of a stream penetration depth for a wide range of conditions.

Chapter 5

CE: Stream-Core Interaction

This chapter is devoted to the study of the processes which take place during (and after) the merging with respect to the primary structure, the mixing and the nucleosynthesis. In Section 1 the method used to calculate the nucleosynthesis in the regions affected by efficient mixing is described. In Section 2 the model for calculating the nucleosynthesis in the core region and in the common envelope is briefly specified. Finally, Section 3 contains results of numerical simulations and the discussion.

5.1 Mixing and nucleosynthesis

In a single star, during its evolution, nuclear burning normally proceeds in regions which are either not mixed or, on the contrary, are mixed very effectively. For a zone stable against mixing the calculation of the chemical composition transformation due to thermonuclear reactions simply requires to solve a nuclear reaction network locally. An effectively mixed zone (convective region) is a zone where the characteristic time-scale of the nuclear burning is much longer than the convective turnover time-scale. Then the gradient of the chemical composition across such a region can be neglected. The chemical composition change can then be calculated by solving the nuclear reaction network with the assumption that during each evolutionary step the change of the composition in each layer will be same as the average in the whole region. However, the nuclear burning which occurs as a result of the merging occurs in an environment where the nucleosynthesis and mixing take place on comparable time scales. It means that the change of the chemical composition in each layer due to the nuclear transformation and due to the mixing with other layers are of the same order and that they therefore should be considered together when solving the nuclear reaction network. An example of an astrophysical objects where this kind of nucleosynthesis takes place are Thorne-Żytkow Objects (red supergiants with neutron cores see Thorne andŻytkow, 1975). In these objects the nucleosynthesis of interest occurs in convective envelopes where the ratio between the convective turnover time and the reaction time varies by several orders of magnitude across the convective region (Cannon 1993).

Let us consider a mixing region where the mixing is provided by convection. In this region the convective eddies are moving up and down, carrying the material from the place where it has been processed by nuclear reactions. A convective bubble will be destroyed after it has moved a characteristic distance (the mixing length). When dissolved, the convective bubble mixes its chemical composition with the layer where it is stopped, changing the composition of that layer. During its movement (up or down), a convective bubble also experiences a composition change within the bubble due to the nuclear burning of the material contained in it. Therefore the situation can be modeled by considering that the change of the composition for a species j in each layer i is the combination of the change due to the nuclear burning, due to the inflow and outflow of the material and due to the dissolving of convective eddies in this layer i. For cells with up-flow and down-flow, the composition variable h_i changes according to

$$\begin{aligned}\frac{dh^j_{i,\mathrm{up}}}{dt} &= \sum R^j_{i,\mathrm{up}} + \alpha_{i,\mathrm{up}}(h^j_{i-1,\mathrm{up}} - h^j_{i,\mathrm{up}}) + \beta_{i,\mathrm{up}}(h^j_{i,\mathrm{down}} - h^j_{i,\mathrm{up}}) \ , \qquad (5.1)\\ \frac{dh^j_{i,\mathrm{down}}}{dt} &= \sum R^j_{i,\mathrm{down}} + \alpha_{i,\mathrm{down}}(h^j_{i+1,\mathrm{down}} - h^j_{i,\mathrm{down}}) + \beta_{i,\mathrm{down}}(h^j_{i,\mathrm{up}} - h^j_{i,\mathrm{down}}) \ .\end{aligned}$$

with the boundary conditions for cells at the edge of the mixing region

$$\frac{dh^j_{\mathrm{top}}}{dt} = \sum R^j_{\mathrm{top}} + \alpha_{\mathrm{top,up}}(h^j_{\mathrm{top}-1,\mathrm{up}} - h^j_{\mathrm{top,up}}), \qquad (5.2)$$

$$\frac{dh^j_{\mathrm{bot}}}{dt} = \sum R^j_{\mathrm{bot}} + \alpha_{\mathrm{bot,down}}(h^j_{\mathrm{bot}-1,\mathrm{down}} - h^j_{\mathrm{bot,down}}) \ . \qquad (5.3)$$

Here $h^j = X^j/Z^j$ is the composition variable for the species j (X^j is the mass fraction of the species j and Z^j is the atomic weight of this species). The quantities R^j_i are the total rate of change of the species j due to the nuclear burning. $\alpha_{i,\mathrm{up}}$ and $\alpha_{i,\mathrm{down}}$ are the fractional changes of the material in the up or down boxes in layer i which can be replaced, due to the vertical flows, by

$$\begin{aligned} \alpha_{i,\mathrm{up}} &= \frac{1}{2m_i}\dot{m}_{\mathrm{up}} \ , \qquad & \dot{m}_{\mathrm{up}} = 4\pi r_{\mathrm{bot}}^2 \rho_{\mathrm{bot}} v_{\mathrm{up}} \\ \alpha_{i,\mathrm{down}} &= \frac{1}{2m_i}\dot{m}_{\mathrm{down}} \ , \qquad & \dot{m}_{\mathrm{down}} = 4\pi r_{\mathrm{top}}^2 \rho_{\mathrm{top}} v_{\mathrm{up}} \ . \end{aligned} \tag{5.4}$$

Here r_{bot} and r_{top} are the sizes of the cell at the bottom of the cell and at the top, ρ_{bot} and ρ_{top} are the densities of the material in the mass flux through the boundary between cells and v_{bot} and v_{top} are (convective) velocities of the flow. $\beta_{i,\mathrm{up}}$ and $\beta_{i,\mathrm{down}}$ are the fractions of the material in the up or down cells which has been replaced due to the mixing between cells at the same level. They take into account the difference in the inflow and outflow mass fluxes and the diffusion with the convective elements, which will be dissolved after they travel a distance l:

$$\begin{aligned} \beta_{i,\mathrm{up}} &= \frac{v_{i\mathrm{c}}}{l_{i,\mathrm{c}}} + \max(0, \alpha_{i,\mathrm{up}} - \alpha_{i,\mathrm{down}}) \\ \beta_{i,\mathrm{down}} &= \frac{v_{i\mathrm{c}}}{l_{i\mathrm{c}}} + \max(0, \alpha_{i,\mathrm{down}} - \alpha_{i,\mathrm{up}}) \ , \end{aligned} \tag{5.5}$$

where $v_{i\mathrm{c}}$ is the logarithmic mean of the top and the bottom values for the convective velocity and $l_{i,\mathrm{c}}$ is the same for the mixing length.

The method described has been developed by R. Cannon for the nucleosynthesis calculations in the convective envelopes of Thorne-Żytkow Objects (Cannon 1992, 1993). For our calculations we used this method in a slightly modified form. One of the modifications is connected to the fact that in our case we have a mixture of radiative and convective regions which could arise and dissolve rapidly. In radiative zones the nucleosynthesis network can be solved for each layer separately, without solving a 3d matrix as is required for the method described above for a zone with mixing. So we modified the code that it solves the composition changes separately for convective and radiative zones and then links them together.

5.2 Nuclear processes

There are several important aspects connected to the nucleosynthesis which involves hydrogen burning in a well mixed zone at high temperature. First of all is the rate of hydrogen burning – as the energy source, it plays an important role for the structure of the merging star, and as a provider of species which provide potential neutron sources it may be a reason for the subsequent formation of s-process elements.

5.2.1 Hydrogen burning

After the interaction of the secondary material with the primary core, the hydrogen rich material will settle in a zone with a temperature of about and more then 10^8K. In this environment the CNO-cycle takes place. The rate of the CN cycle

$$^{12}\mathrm{C}(p,\gamma)^{13}\mathrm{N}(e^+\nu)^{13}\mathrm{C}(p,\gamma)^{14}\mathrm{N}(p,\gamma)^{15}\mathrm{O}(e^+\nu)^{15}\mathrm{N}(p,\alpha)^{12}\mathrm{C}$$

at $T \leq 2 \cdot 10\ ^8$K is limited by the beta-decay

$$^{13}\mathrm{N} \rightarrow ^{13}\mathrm{C} + e^+ + \nu\ ,$$

which has a half-life time of 10 minutes. At higher temperatures, $T \geq 2 \cdot 10^8$K, another loop of the CN cycle dominates (hot CNO cycle)

$$^{12}\mathrm{C}(p,\gamma)^{13}\mathrm{N}(p,\gamma)^{14}\mathrm{O}(e^+\nu)^{14}\mathrm{N}(p,\gamma)^{15}\mathrm{O}(e^+\nu)^{15}\mathrm{N}(p,\alpha)^{12}\mathrm{C}$$

and its rate is limited by the reaction

$$^{14}\mathrm{O} \rightarrow ^{14}\mathrm{N} + e^+ + \nu$$

with $\tau_{1/2} = 72$ seconds.

If the mixing time-scale provided by convection (which can easily be as short as about 50 sec in our case) is shorter than the limiting hot-CNO cycle beta-decay time, then the common rate of the cycle would be slowed down. Let us consider the intermediate zone, or the zone between the hydrogen rich zone and the hot zone. This zone which was not enrich with hydrogen originally. If convection is not fast enough to make s convective bubble pass this intermediate zone without sufficient burning, then the composition gained by the zone with high temperature is reduced in hydrogen. Therefore the energy rates could be smaller than in the case of extremely fast convection.

5.2.2 Neutron sources

Suess and Urey (1956) suggested, and Burbidge *et al.* (1957) have shown in details that the synthesis of heavy elements can be achieved by capturing free neutrons in 2 ways, the $s-$ and the $r-$ process, depending on the density of the neutron flux. In order to produce solar abundances for heavy elements by the s-process, it is necessary to have a neutron flux $f_n \approx 10^{15} - 10^{16}[\mathrm{neutron\,cm^{-2}\ s^{-1}}]$ (it corresponds to a neutron concentration $n_n \approx 5 \cdot 10^5 - 10^6[\mathrm{neutron\,cm^{-3}}]$ with a characteristic Maxwellian velocity $v_n \approx 5 \cdot 10^8$) during the exposure time $\geq 10^3$[years] (see e.g. Chechev and Kramarovskii 1981). Clayton in 1961, investigating the "canonical" s-process (known in literature as CFHZ), which does not take into account the branching of the s-process, has shown that for observed s-process abundances of advanced s-elements like $^{206}\mathrm{Pb}$, one requires a neutron exposure (neutron flux integrated over time) of about $10^{26} - 10^{27}[\mathrm{neutron\,cm^{-2}}]$ and a corresponding neutron capture number of $n_c \approx 100$ [neutrons] per Fe nucleus.

Several possible neutron-source mechanisms have been identified. If hydrogen can penetrate from the outer parts of a star to the region rich in He then it could take place through the following chain of reactions:

$$p +^{12}\mathrm{C} \rightarrow^{13}\mathrm{N} + \gamma\ ,^{13}\mathrm{N} \rightarrow^{13}\mathrm{C} + e^+ + \nu\ ,^{13}\mathrm{C} +^{4}\mathrm{He} \rightarrow^{16}\mathrm{O} + n\ .$$

The reaction $^{13}\mathrm{C}(\alpha, n)^{16}\mathrm{O}$ operates at $T \approx 10^8$K. At higher temperature ($T > 10^9$K) the (α, n) reactions at the nucleus with mass number $A = 4n+1 > 13$ ($^{17}\mathrm{O},^{21}\mathrm{Ne},^{25}\mathrm{Mg}$) become efficient (see Fig. 5.1). Even though (α, n) reactions look very promising, only traces of $^{13}\mathrm{C},^{17}\mathrm{O},^{21}\mathrm{Ne},^{25}\mathrm{Mg}$ normally remain after hydrogen burning in the CNO-cycle (e.g. $^{13}\mathrm{C}/^{56}\mathrm{Fe} \approx 0.2$).

The burning of carbon $^{12}\mathrm{C}(^{12}\mathrm{C}, n)^{23}\mathrm{Mg}$ at the same temperature produces about 5-25 neutrons per Fe nucleus, and oxygen burning produces $^{16}\mathrm{O}(^{16}\mathrm{O}, n)^{31}\mathrm{Si}$ about 100 neutrons per Fe nucleus, but products of these reactions are not going to play an important role for the envelope abundance of s-process elements.

Cameron (1960) showed that an additional neutron source can be provided by the chain

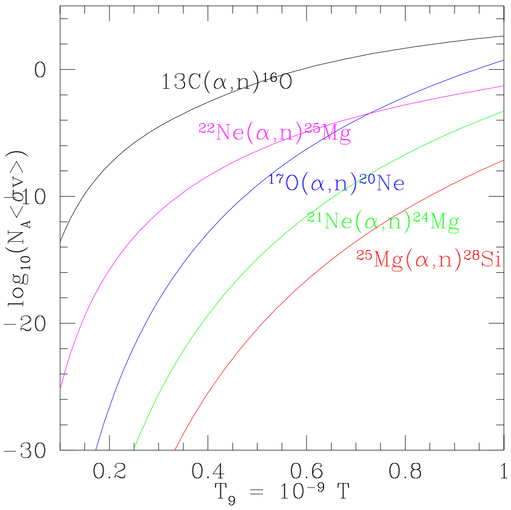

Figure 5.1: Reaction rates for neutron production for (α, n) reactions. The temperature is scaled as $T_9 = T/10^9$K.

$$^{14}\mathrm{N}(\alpha,\gamma)^{18}\mathrm{F}(e^+,\nu)^{18}\mathrm{O}(\alpha,\gamma)^{22}\mathrm{Ne}(\alpha,n)^{25}\mathrm{Mg}\ .$$

The temperature at which this reaction starts to be intensive is $T \geq 3 \times 10^8$ K. Such a high temperature can be achieved e.g. during the peak burning phase of the He-shell flash in red giants or during He core burning in massive stars with the production of about 40 neutrons per Fe nucleus (see also e.g. Truran 1981).

Harrison & Edwards in 1974 showed that there can be a neutron-source mechanism working on the low-temperature photo-neutron reactions (γ, n), which follow after (p, n) reactions: $^{13}\mathrm{C}(\gamma,n)^{12}\mathrm{C}$, $^{13}\mathrm{N}(\gamma,n)^{13}\mathrm{N}$. These processes produce sufficient neutron fluxes (10^9 – 10^{11}[neutron $\cdot\,\mathrm{cm}^{-2}\cdot\mathrm{s}^{-1}$]), but are still insufficient to support advanced s-nucleosynthesis.

The most plausible mechanisms in our case will be discussed in subsection 5.3.8.

5.2.3 Nuclear reactions network

For the calculations of nuclear reactions, which can provide s-processing, we need detailed nucleosynthesis reaction rates both for the hot-CNO cycle and for the s-processing. For the nuclear burning calculations all possible reactions were taken from the Friedel Thielemann Reactions Library (FTRL) (data from 1991, the library has been provided by R. Cannon). This library provides

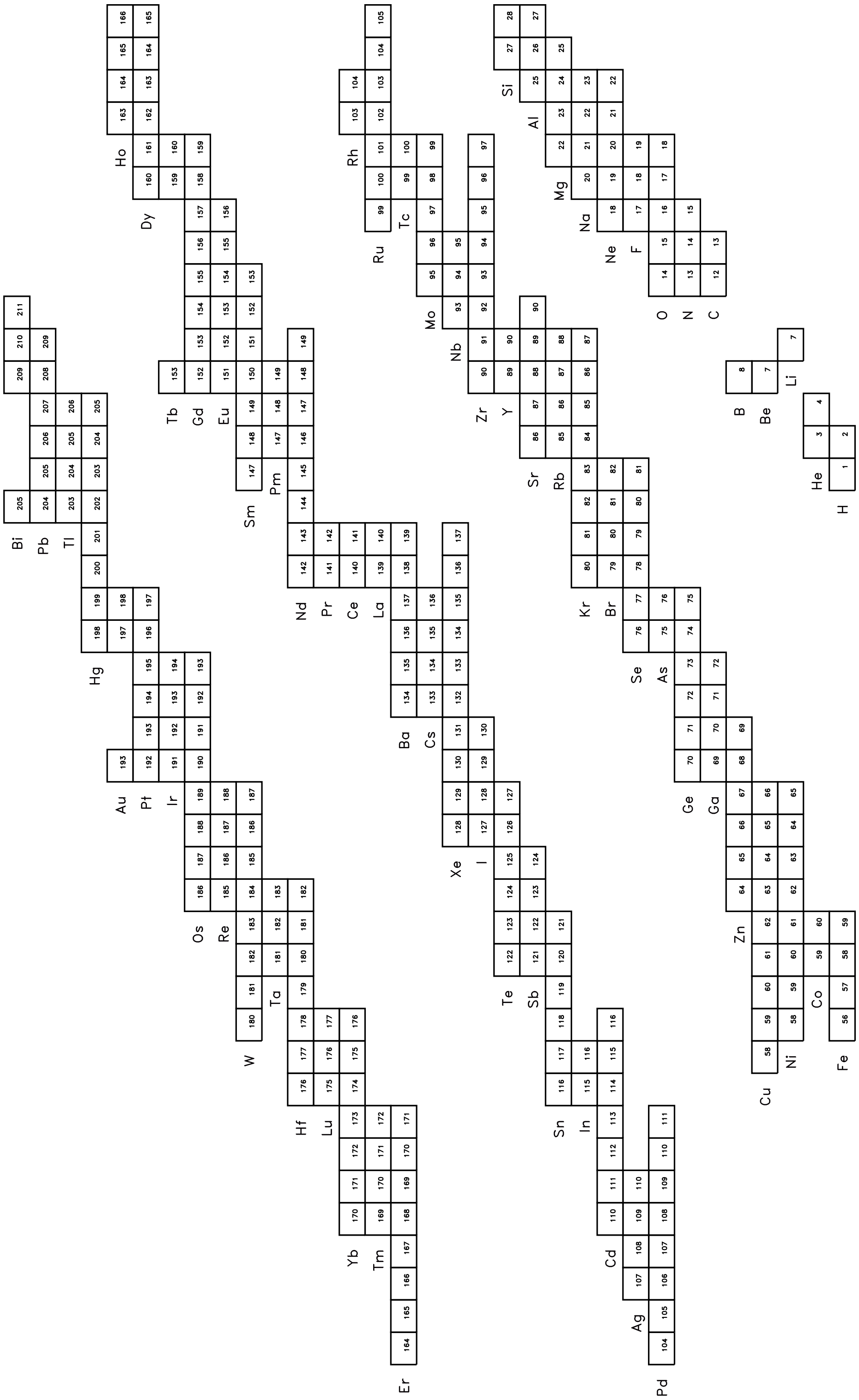

Figure 5.2: Elements of the full Nuclear Reactions Network

the data for reaction rates which can be applied for a wide range of temperatures ($T = 10^7 - 10^{10}$) K for all elements up to ^{84}Kr. For heavier elements the library has been updated for neutron-capture cross-sections and half-lifes of beta-decays for the s-elements from ^{85}Rb up to ^{209}Bi. The data for the cross-sections were taken from the work of Beer, Voss and Winters (1992) and have been interpolated using the method of minimal squares to fit the formulae for reaction rates used in FTRL. The data for $\tau_{1/2}$ of beta-decay have been taken from Newman (1978). In Fig. 5.2 we show all the elements of the full NRN which we can take into account. But it is important to mention that unfortunately so far it has not been found possible to solve the whole network simultaneously with the merger using the available computing resources, and in actual calculation the shorter network (for heavy elements) has been considered.

5.3 Numerical simulations

5.3.1 Model description

As a starting point for the merger calculations we use a binary consisting of a 18 $M_{\odot}$primary and a 2 $M_{\odot}$secondary. The primary at the start of the spiral-in has been evolved to the stage where it has a core of about 6.8 $M_{\odot}$ (and a He-exhausted core of about 4.1 $M_{\odot}$). The secondary is then assumed to spiral-in inside the envelope of the primary, and the merger phase starts when the immersed secondary begins to overfill its Roche lobe. At this moment the secondary almost reached helium rich layers (but not the helium burning shell). Since a primary application for this scenario is modelling the progenitor of SN 1987A, we adopted a chemical composition consistent with the composition of young stars in the LMC, with $X = 0.71$ and $Z = 0.01$. This model has been evolved to the point just before the carbon core ignition with a chosen mixing-length parameter $\alpha = 2$ and where convective overshooting by 0.25 pressure scale heights was included. For this model we used Schwarshild criterium for convective instbaility. The model we calculated is slightly different from the one which has been calculated with the original code given by Podsiadlowski code (see Fig. 5.3). The main reason for the small difference has not been identified, but is probably attributable to the different nuclear reactions network (see Appendix C). Here we just want to point out that the behavior of the stellar luminosity before the star became a red giant depends very sensitively on the initial CNO composition, e.g. the decrease in the carbon abundance causes stronger decrease in the

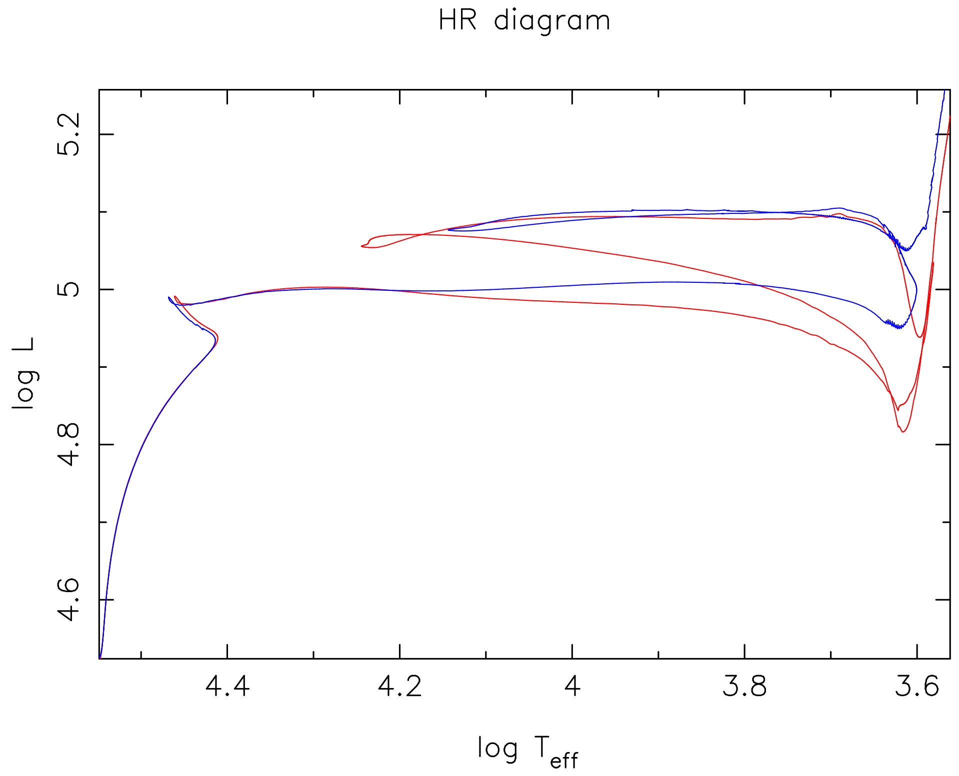

Figure 5.3: Evolution of a 18 $M_{\odot}$ star, with composition LMC. Red color represents the model in the original code, blue color in the modified code.

stellar luminosity.

There are several of parameters which can be varied for the model under investigation. First of all, the parameter affecting the *penetration efficiency*: the entropy change coefficient. The structure of the star considered can be characterized by $\alpha_{\rm P} = 5.2$ and $\alpha_{\rm T} = 1.3$ and a favourable value for $k(\alpha_{\rm P}, \alpha_{\rm T})$ is about 0.4 (for this particular model). But this parameter changes during the merging (due to the changes in the primary structure) and can be as small as 0.1.

The next important parameter of the problem is how wide the *stream can spread out* its material above the point of deepest penetration. As it was shown in Chapter 4, if the primary star contains a core which rotates faster than the ambient medium (e.g., due to the angular momentum of the accreted secondary material), the stream will spread out its material in a narrower zone.

During the merger the binary continues to shrink its orbit. The corresponding release in orbital energy is transferred to the common envelope, partially as heat and partially in the form of kinetic energy of the rotating envelope. The *energy balance*, or balance between the amount of the energy released as heat and as kinetic energy might be important. To check this, apart from the model using the energy distribution as it was described in Chapter 2, we ran a number of models where either the whole energy released was converted to heat or with the assumption that 95% of the orbital energy went into kinetic energy of the rotating envelope. In these calculations it was assumed that matter within the binary orbit was in corotation with the binary to at least 0.95%.

One uncertainty which cannot be neglected in the modelling of the merger is the *description for convection*, in particular - how far convective elements can penetrate out of the convective zones and therefore provide additional mixing, or overshooting and undershooting parameters, [1]. therefore we included as one of the parameters an undershooting parameter, which is not necessarily equal to the overshooting parameter.

Additionally we want to mention that some differences in the results can be caused by the *age of the model* we want to consider. E.g., the basic model we have for the merger modelling is well evolved and close to the point of carbon core ignition with the core of about 6.8 $M_\odot$ where the mass in the helium *burning convective* zone is about one solar mass. The younger model, taken as about 1500 years younger, has a radius smaller by only 4% and with the difference in the central temperature of the carbon-oxygen core as only $\log T_c = 8.78$ compared to $\log T_c = 8.83$. But the mass contained in the helium burning convective shell is smaller by the factor of 2 – it is only half of a solar mass. Also, in the younger model this zone is spatially placed closer to the core and this zone itself might be more difficult to reach by the hydrogen injection.

As long as we aim to construct a model which might closely describe the progenitor of SN1987A, in analysing the results we pay special attention to the composition in the envelope and the resulting He and CNO abundances. The easiest way to understand how mixing has been processed in the envelope during the merger is to study the time evolution of the location of convective regions.

Therefore we will describe each model discussed below in terms of the penetration depth efficiency, the stream spreading, the energy source efficiency, the model of convection, how well

[1]As the undershooting we mean the additional mixing below the boundary of the convective zones, in the direction toward the core. In the literature this is also known as the overshooting, here we use undershooting to distinguish these cases.

the star is evolved to the supergiant stage and will discuss these using a convective regions evolution scheme. Also, we do not provide here a separate description for the chosen merger, since we do not have a favorable standard model, but discuss the behavior during (and for some models after) the merger, comparing discrepancies in the behavior depending on the input parameters.

5.3.2 Case: age of the model

Scenario: energy reduced, wide stream spreading, no undershooting

In this subsection we compare the results of the merger calculations made for merger progenitors of different ages. As has been mentioned before, our standard model is taken before the carbon core burning starts. This star has a core of about 6.8 $M_\odot$, where helium-rich shell is between 4.6 $M_\odot$ and 6.8 $M_\odot$; the helium convective zone is between 4.9 $M_\odot$ and 6.0 $M_\odot$[2] (its width is 10^{10}cm). The younger star have developed helium convective zone only between 4.9 $M_\odot$ and 5.5 $M_\odot$ (its width is $5 \cdot 10^9$cm)

The reduction of the energy for this scenario means that part of the orbital energy released goes into kinetic energy of the rotating envelope and does not play any further role as heating energy. Since this model does not take into account the viscous friction energy, the reduced energy is lost from the stellar model for the rest of calculations (no energy conservation).

It has been found that for this scenario of the merger the time-scale of the merger for the young star (or, in other words, the time required for the secondary to complete its destruction, this time depends on the mass loss rates from the secondary) is very long, about a few hundred years. In Fig. 5.4 we present the time evolution of the convective regions, by radius and by mass (to see better details, the mass coordinates only show half of the star). The first feature which has to be explained in this picture is the time evolution of the bottom of the outer convective zone: as you can see from the right panel, after the shift up in the first few years of the merger, it goes up continuously. This is only an artificial effect: in reality the bottom of the convective zone (after the shifting initially) stays convective, but its mass coordinate, during the merger, increases. On the other hand, during the second part of the merger, when most of the secondary has already been dissolved, the

[2]Before the start of the spiral-in these convective zones contained smaller masses and have grown till the end of the spiral-in to the cited values due to its own evolution and due to the spiral-in effects. The size of the convective zones has not been found to be dependent much on the spiral-in input parameters.

convective zone starts to expand *downwards*. This behavior is common for all the models which will be discussed later (except of the initial shift of the convective zone). As you also can see, during the interaction of the stream with the core, at the place where the stream falls an additional convective zone forms. Being not very effective, this zone touches the initially helium-rich layer very gently and as a result the final helium abundances in the envelope is not increased much - by only 4% compared with the abundances before the merger. Closer to the end of the merger, another convective zone is created near the secondary orbit. As you can see on the left panel of the Fig. 5.4, the second and the first additional convective zones never spatially intersect with each other, but at the end of the merger the outer zone comes to the place where the first additional convective zone previously worked . After the completion of the merger, the primary proceeds its evolutionary part not much differently as from a normal evolved star, since it keep its internal structure (He shell and the core) almost unchanged.

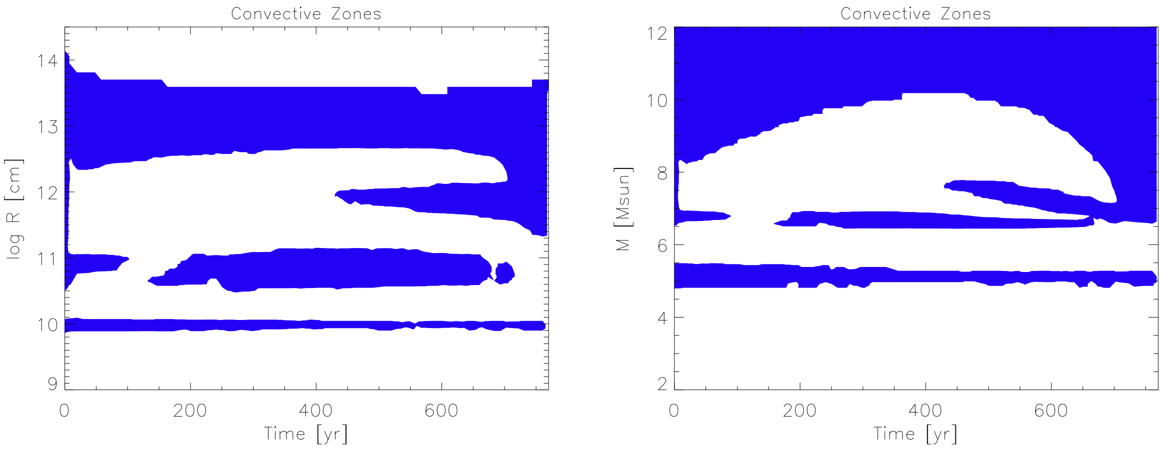

Figure 5.4: Locations of convective regions (by radius and by mass) for the merger scenario with reduced energy for the younger model (see Subsection 5.3.2 for details).

For the older star the situation in this scenario is almost the same, except for the fact that it managed to get slightly more helium and increased its helium abundances by about 8% compare to the pre-merger one. We can conclude that this scenario is unlikely to lead to interesting results, such as significant changes in the envelope composition, but it shows that not all experienced merger stars should necessarily have an overabundant helium composition in the envelope. The additional issue to this case is the consideration of rotation of the star and its effect on the mixing; we will discuss it some more details in subsection 5.3.9

In subsequent subsections, if not specified, we concentrate only on the models with the older star as the merger progenitor.

5.3.3 Case: the stream spreading

Scenario: whole energy installed, no undershooting

The advantage of this scenario compared to the previous one is that it takes into account the whole of the released energy and conserves it, even though the rate of the transfer of this energy into the envelope as heat is higher than it would be in a real case, which falls somewhere between this scenario and the previously considered one. For this scenario we consider two models: with wide spreading of the stream material (taken as 2 pressure scale $H_{\rm P}$ above the point of the stream's deepest penetration) and a narrower stream ($0.5 H_{\rm P}$).

Before considering differences caused by the different stream width, we want to point out differences caused by the different treatment of the released orbital energy. The characteristic time-scale of the merger is significantly shorter, about 30 years (see Fig. 5.5). The peak period in the mass loss rates occurs about 21 years after the start of the merger and lasts for about 5 years, with the average mass loss rate 0.25 $M_\odot$ per year. Before this intensive period starts, not many changes happen in the primary structure. At the end of this intensive period the secondary has only left about 0.25 $M_\odot$ and the secondary's orbit is slightly wider than at the start of the merger; the secondary temporarily stops its mass loss. The final mass loss works in the exponentially increasing regime, and once started, dissolves the rest of the secondary in less than a year.

The amount of the disturbance by stream injection of helium rich material at the end of the merger is almost the same for the model with the wide stream as in the previous scenario (about 0.1 $M_\odot$) and larger for the narrower stream (about 0.3 $M_\odot$). Since the merger time is shorter but the amount of the released potential energy from the stream is almost the same, and therefore the energy generation at the stream penetration depth is about one order of magnitude higher, it affects significantly the subsequent evolution of the post-merger star. The key factor are growing

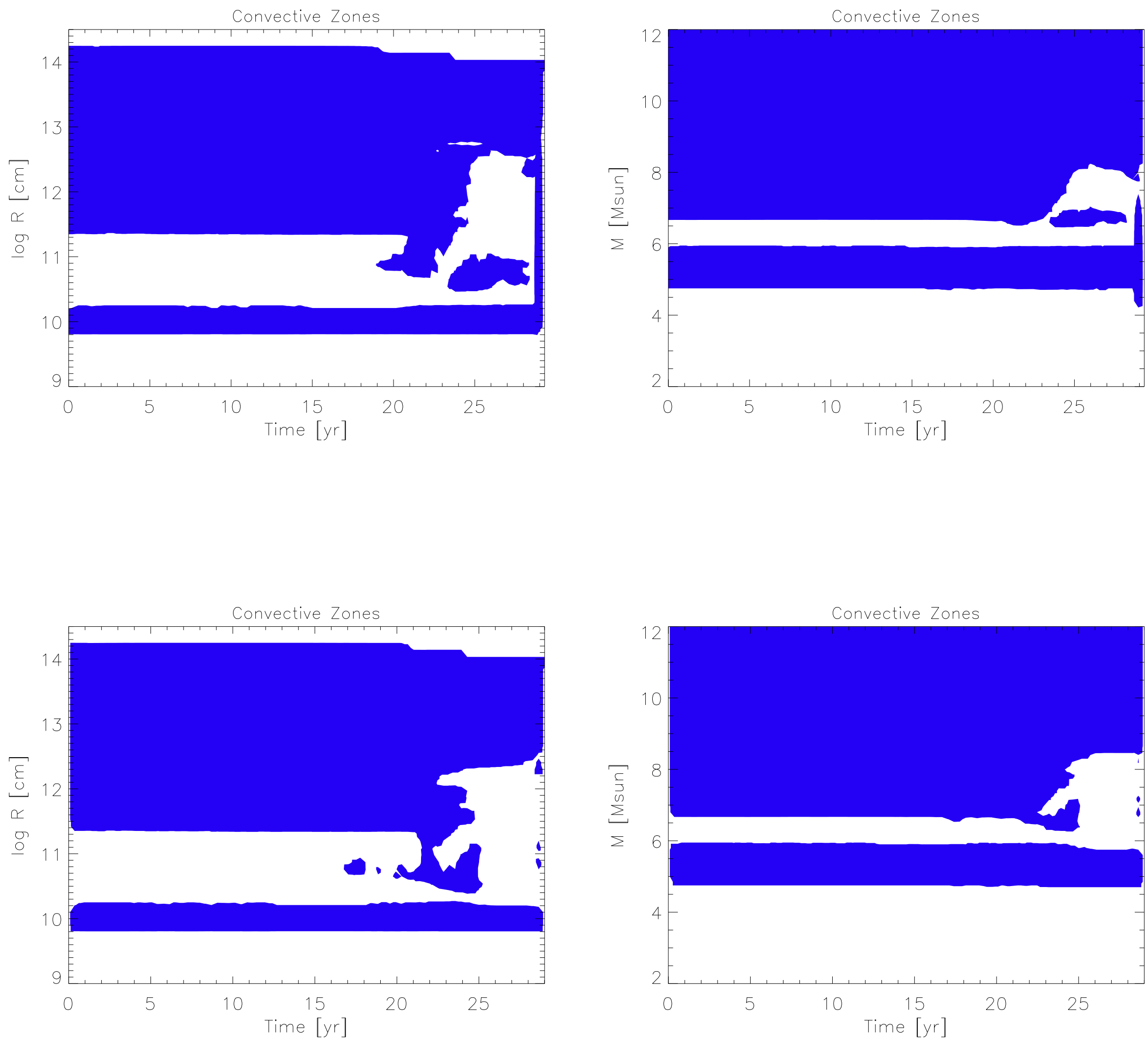

Figure 5.5: Locations of convective regions (by radius and by mass) for the merger scenario with different stream spread widths (see Subsection 5.3.3).

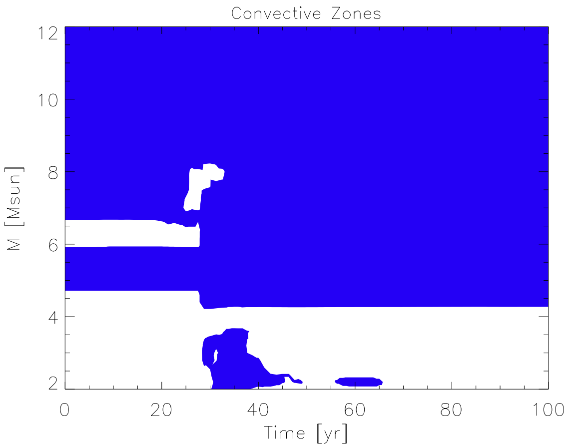

Figure 5.6: Locations of convective regions (by radius and by mass) for the merger scenario with wide stream spread widths, including the post-merger epoch (see Subsection 5.3.3).

convective zones. At the latest stages of the secondary's destruction, the bottom of the helium convective zone expands toward layers poor in helium (the carbon core) and toward layers rich with hydrogen (see Fig. 5.5, the top right panel). As a result, the model of the star after the merger will have envelope abundances 0.393 (mass fraction) of the helium and 0.00723 of carbon (for more details how mixing with the envelope proceeds after the merger see Fig. 5.6, where convective regions are shown for the post-merger period too). We should mention that the development of this covering all the helium shell convective zone is not absolutely clear, and pretty much dependent on the way how the released orbital energy is installed into the star, but is mandatory in the case if the rest of orbital energy at the end of the merger will be released locally as heating energy. As you can see in Fig. 5.6, the outer convective zone merges with the expanding convective zone in a few years after the merger and this large outer convective zone exists for the next few thousand years. During this time the star evolves down the supergiant branch, where the stellar luminosity slowly decreases as radius contracts with time.

5.3.4 Case: the energy treatment

Scenario: wide stream spreading, no undershooting

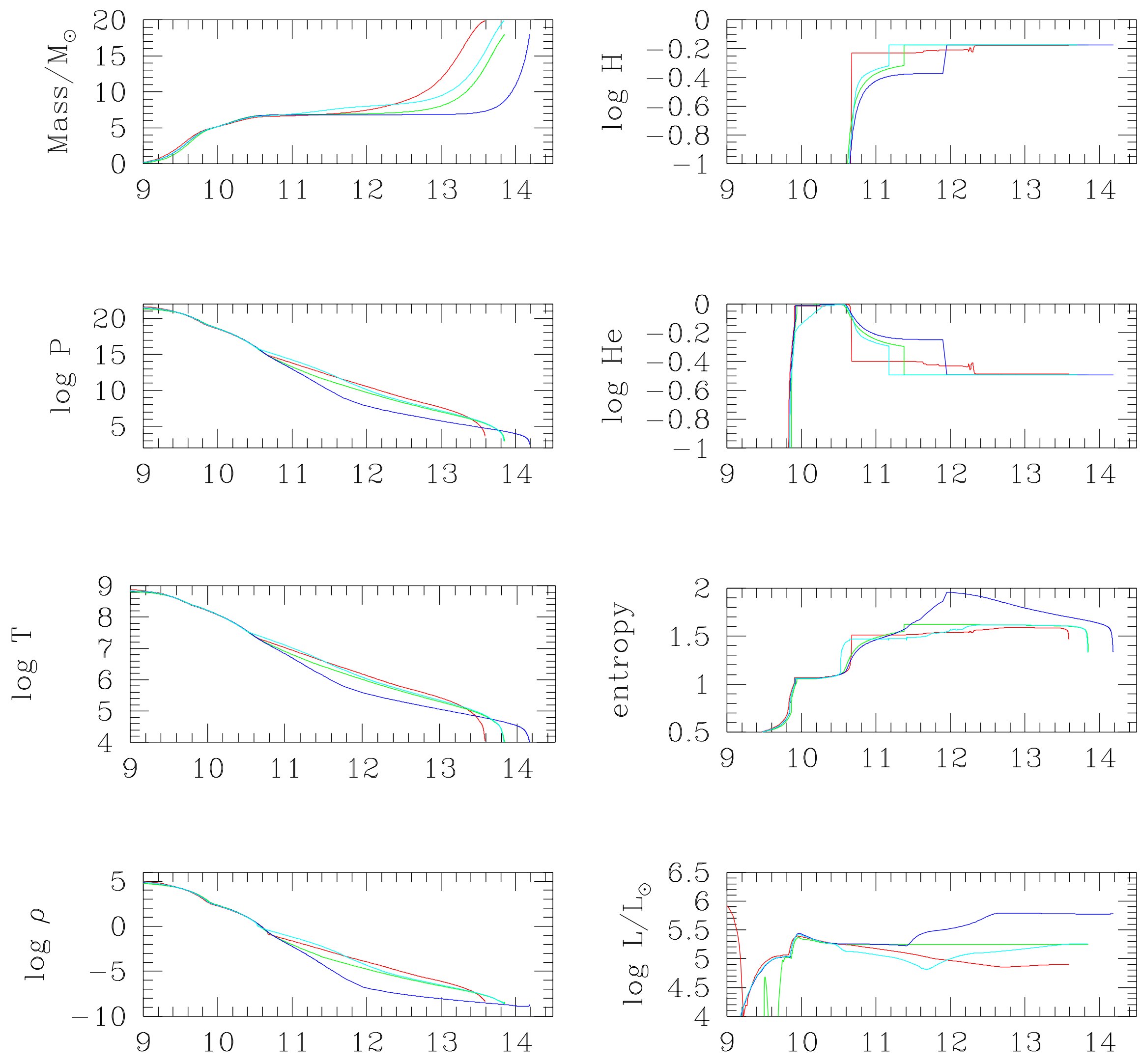

Figure 5.7: Structure of the primary star at four different stages: at the start of the spiral-in (green), at the end of the spiral-in – start of the merger (blue), at the end of the merger (cyan) and 500 years after the merger finished (red). X-axis is the log of the radius of the star.

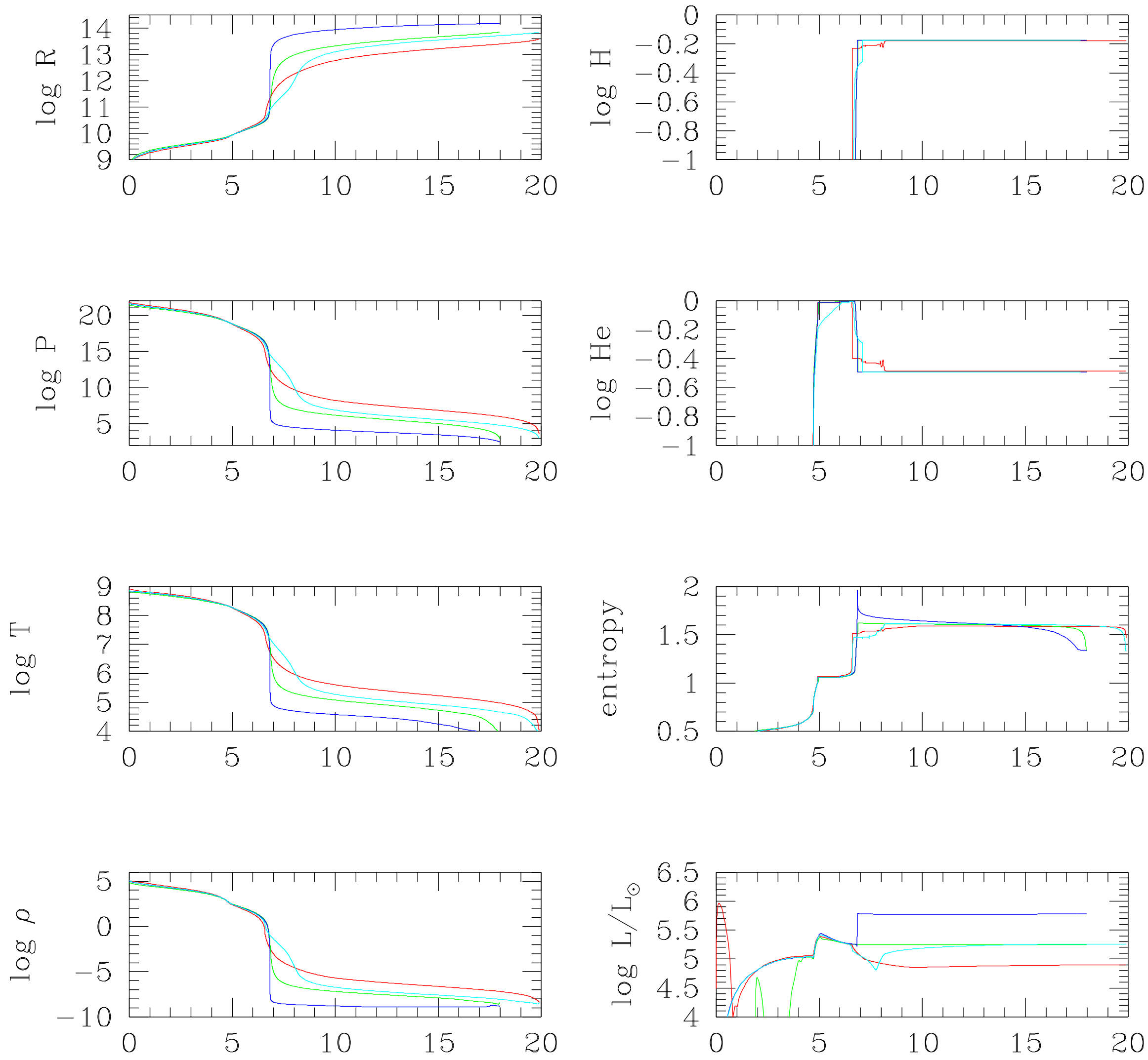

Figure 5.8: Structure of the primary star at four different stages: at the start of the spiral-in (green), at the end of the spiral-in – start of the merger (blue), at the end of the merger (cyan) and 500 years after the merger finished (red). X-axis is the mass of the star.

Once we have considered two limiting cases and know the tends of behavior in both cases, we want to know results for a model which approaches the real situation as close as possible in the framework of our approximated model, which takes into account the angular velocity profile in the primary envelope. For this model we artificially reduced the deposition of the orbital energy at the latest stages of the merger (when the secondary has left less that 0.1 $M_{\odot}$). This should not affect the merger stage, but should make differences in the post-merger stages.

The calculations have shown that the time-scale for the merger in this model is about 60 years and the amount of the touched by the stream helium rich material during the merger is to order of magnitude the same as in the previously calculated models with different energy treatments (about 0.1 $M_{\odot}$). The main difference is that this helium does not get mixed with the outer convective zone immediately: e.g., the model of the star 500 years after the merger still has an intermediate helium rich shell, where the mass fraction of the helium is 0.4 (see Fig. 5.7 and Fig. 5.8, where the internal structure for the primary star at the different stages of its evolution is shown: before the spiral-in, at the end of the spiral-in, at the end of the merger and 500 years later, when the model already has started the carbon core burning). This layer finally get mixed with the outer envelope only about 700 years after the merger. This model contracts after the merging faster than the model where the whole binary energy is installed at the end of the merger, achieving a radius in about 500 years 1.6 times less than at the start of the spiral-in. After the mixing is completed, the star starts to expand and goes up on the supergiant branch.

The main conclusions from this calculation are: the models are almost independent of how energy is deposited during the merger but the end of the merger is important. The increase in helium abundances, if does not develop an intensive helium convective zone, is the same, even if the surface dredge-up can be delayed by a few hundred years.

5.3.5 Case: the penetration depth

Scenario: "proper energy treatment", wide stream spreading, no undershooting

For these calculations we considered models with assumed entropy change coefficients of $k = 0.2$ and $k = 0.1$. The main feature of these models is that the intermediate convective zone, created due to the stream fall, a zone rich in hydrogen, connects with the main helium burning

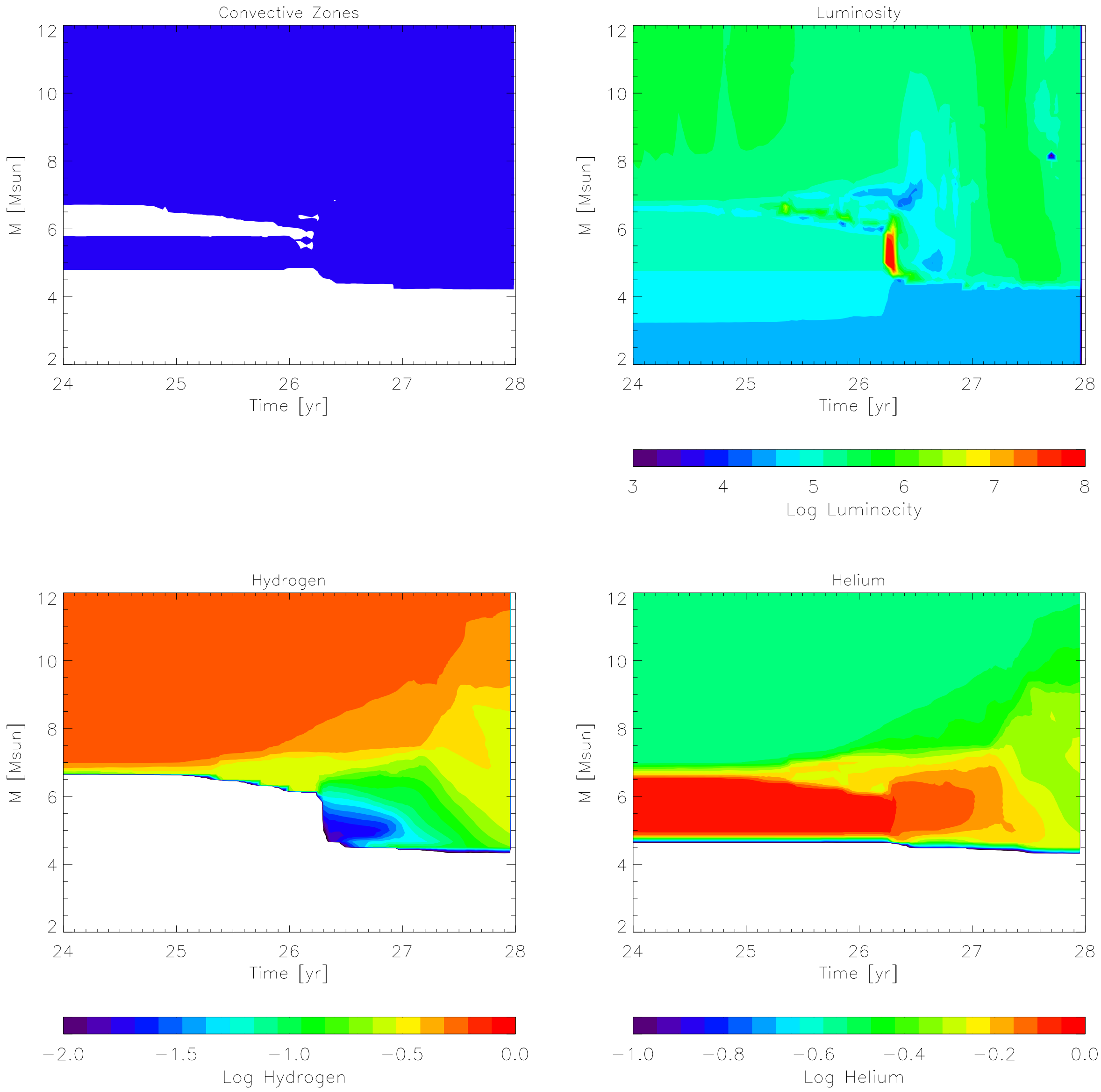

Figure 5.9: Locations (by mass) of convective regions, luminosity, hydrogen and helium abundances for the merger scenario with $k = 0.2$, near the He shell explosion event.

convective zone during the merger. As a result, intensive nuclear burning proceeds within the helium convective zone and the He shell expands fast, in less than year (see Fig. 5.9, where we show the evolution of the convective zone locations, He and H abundances and luminosities at the time near this event and Fig. 5.10, where the evolution of the temperature profile and of the radius are shown). The only difference between models of different k is that the explosion event happens earlier for the model with $k = 0.1$, when the secondary has lost about $0.65\ \mathrm{M}_{\odot}$, and in the case of $k = 0.2$, where the additional convective zone is created initially slightly further from the core, the event happens when the secondary has lost about $0.9\ \mathrm{M}_{\odot}$. At the moment when the two convective zones touch each other, the mass in the hydrogen-rich convective zone (the zone which at this moment has accumulated most of the transferred from the secondary material) is larger. Therefore the expansion should be more effective in this case. As indicator of the explosion efficiency one can consider the amount of the mass stripped out from the (carbon) core. Indeed, at the end of the explosion the mass of the core-remnant in this case is $4.47\,\mathrm{M}_{\odot}$, when in the case of $k = 0.1$ the mass of the core-remnant is $4.56\,\mathrm{M}_{\odot}$. The mass of the carbon-rich core in the progenitor (or the mass of the core where the mass fraction of the carbon is at least 0.1) is $4.95\,\mathrm{M}_{\odot}$. That means that at this stage the star has ripped-off about $0.5\,\mathrm{M}_{\odot}$of carbon rich material which will be later mixed with the envelope. Therefore a simple estimation shows that the final carbon abundance in the envelope will be at least 0.004 (by mass fraction), which is approximately 3.3 times higher than LMC carbon abundances. It is important to point out that the timescale of the He shell explosion event is about 0.25 year, and therefore is not a dynamical event.

Two possible sequels to the explosion can happen. First is that the secondary may not survive the explosion phase and therefore will be completely destroyed by the end of the He shell explosion. We can not model this solution with our model for the mass loss rates from the secondary, since the event is intrinsically dynamical and affects the secondary structure. To consider this case we enforced the secondary destruction and continued the evolution. In this case the star consists of a carbon core and the convective envelope (initially very underdensed). The profile keeps the same shape as is shown in Fig. 5.10, but slowly increasing in temperature and density. In a few hundred years the envelope is mixed entirely and the surface abundances became (by mass fractions): He = 0.4, C= 0.009, N = 0.0083, O = 0.00055. The convective envelope comes close to the hot carbon core. During the first thousand years the merger product contracts (very fast at the beginning) and becomes less luminous and smaller in radius than at the start of the spiral-in and subsequently starts to go up again on the giant branch, increasing slowly in luminosity and expanding. We followed to its evolution for a few thousand years, till the moment when the carbon core already became exhausted of carbon. More details of the possible s-processing in this scenario are discussed in subsection 5.3.8

In the case where the secondary survived the explosion event and the CE evolution with the mass transfer from the secondary continues, the profile as shown in Fig. 5.10 stays for a few years, where the secondary orbits in the very underdensed region. Since the region near the carbon core in this case is already rich in hydrogen, this case should provide a perfect site for the producing of neutrons (see more details about s-processing see subsection 5.3.8). But it is very difficult numerically to follow this evolution - the continuing slow expansion of the envelope and its further decrease in density creates a shock (at a distance of a few 10^{12} cm from the center, where the bottom of the outer convective zone is). After a few years of the evolution we are not able to follow its further evolution with the evolutionary code we have. Nevertheless, in all models where we have continued the calculations for a few years, the stream continues to rip-off material from the carbon core, with different rates for $k = 0.1$ and $k = 0.2$. In the case of $k = 0.1$ it can be predicted that almost all the carbon core might be disrupted by the stream if it will proceed in the same way (the carbon core tends to expand after it has decreased to a certain mass). Also, we would like to mention, that the region near the carbon core, where the most effective nucleosynthesis happens, is separated by the radiative zone from the outer convective envelope and we can not predict whether this mass region will be mixed with the outer region in the future or not. If the response of the star after the complete destruction of the secondary will be the same as in the case of destructed secondary immediately after the He shell explosion, all the nucleosynthesis product will be mixed with the outer convective envelope and will be presented there simultaneously with the carbon ripped off the carbon core.

The scenario with a surviving secondary is very interesting from many points of view, and especially from the point of view of nuclear processes. From 1d calculations we see that the structure of the star tends to have a drop in the density profile (smaller around the orbit than in the outer part of the envelope). In the real situation the matter within the orbit will not drop in density that much, getting material from poles, and the situation therefore will not be as catastrophic in regards of the density drop. Therefore this model can be handled only properly by at least a 2d calculations. But to consider it properly one needs not only to have a 2d model of the star - as our simulations have shown, the code also has to treat the convection properly and solve the nucleosynthesis together with convection (to achieve the He shell expansion and create a naked carbon core). Possibly the 3d stellar evolution project which is lead now by P.Eglleton at the Lawrence Livermore National Laboratory will be able to handle it.

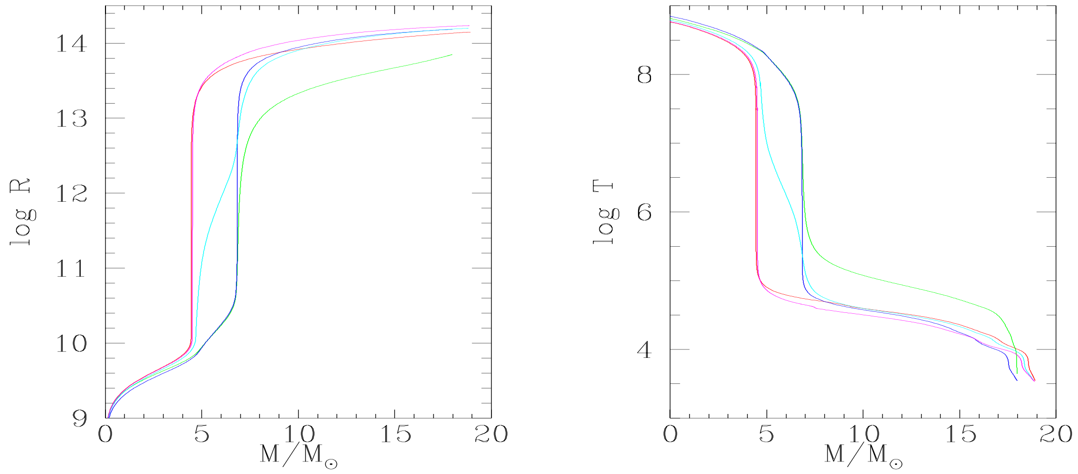

Figure 5.10: Radial coordinates and temperature of the primary star as a function of mass coordinates at four different stages: at the start of the spiral-in (green), at the end of the spiral-in – start of the merger (blue), in the middle of the merger, when the He shell is expanding (cyan), immediately after the He shell expanded (magenta) and 1 year later (red); for the model with $k = 0.2$.

5.3.6 Case: the undershooting

Scenario: whole energy installed, wide stream spreading, $k = 0.4$

As we mentioned before, undershooting may be important. As we have shown in our simulations previously described, the results of the merger depend strongly on the interaction between the existing convection zone and the zone created during the merger. Therefore undershooting from the created by merger convective zone may play significant role.

To create a self-consistent model of the merger with undershooting, we evolved the 18 $M_\odot$ star as it was described before, but with an assumed undershooting of 0.1 and picked up the model which has about the same central temperature as for the previously considered model. The model has an evolutionary path slightly different from the model without undershooting, but structures of models with and without undershooting for the chosen moments are almost the same. Small differences in these models are: the model with undershooting has surface abundances of H=0.64, He=0.35, C=0.0002, N=0.0016, O=0.00046 compared to the model without undershooting H=0.67, He=0.32, C=0.00021, N=0.0018, O=0.00046 (by mass fractions). The mass of the He core is $6.7\,\mathrm{M}_\odot$ and its radius is 10^{11} cm (compared to $6.9\,\mathrm{M}_\odot$ and $2.3 \cdot 10^{11}$ cm).

The calculations of the merger performed did not show significant differences with the case of the same k and no undershooting - we expected the development of a stronger intermediate convective zone, but the calculations did not show this tendency.

5.3.7 Case: a companion of a different mass

Scenario: whole energy installed, wide stream spreading, no undershooting, k=0.4

For these calculations we used a companion of one solar mass. This case, as was shown in Chapter 1, should lead to a faster merger. Also, a main sequence star of one solar mass of the same age as the previously considered secondary of two solar masses has lower entropy, therefore even with the assumed favourable entropy change coefficient of 0.4 the stream from the secondary should penetrate deeper. Indeed, calculations have shown that the effective penetration depth in this case is the same as for the secondary of two solar masses but with $k = 0$. In general this case is quite similar to the case with low k in subsection 5.3.5: the non-convective helium zone accumulates hydrogen-rich material, with the increase in mass loss rates the convective zone arises and starts to grow. The connection of the hydrogen-rich convective zone with the He burning convective shell starts once the secondary has lost about $0.55\,\mathrm{M}_\odot$. Later the evolution has the same behavior as was discussed in subsection 5.3.5, apart from the fact that our calculations did not show any significant carbon core rip-off, after the explosion the core still had some helium layers around. Therefore this case leads to an increase of the helium abundances in the outer envelope without significant carbon overabundances.

5.3.8 S-processing

To study the s-processing in details we took models described in subsection 5.3.5, cases when the He burning shell exploded and is entirely mixed with the convective envelope. Fig. 5.11 shows the

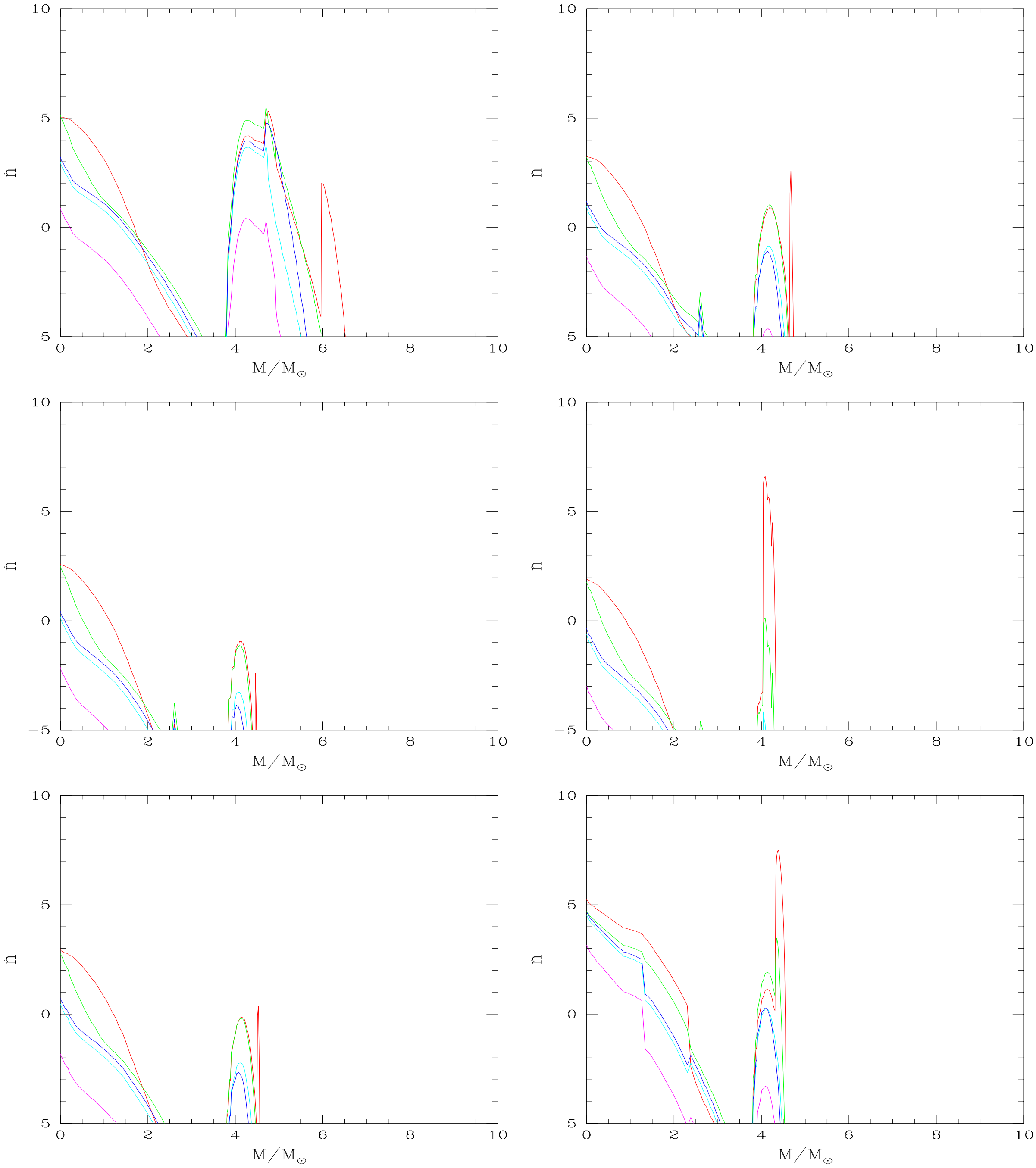

Figure 5.11: Neutron production [neutron g $^{-1}$ s^{-1}] by (α, n) reactions on different nucleus: ^{13}C (red), ^{17}O (green), ^{21}Ne (cyan), ^{22}Ne (blue), ^{25}Mg (magenta). X-axis is the mass of the star. Top left panel: before the merger, top right - during the He shell explosion, middle left - immediately after the He shell explosion, middle right - three years after the He shell explosion, the secondary survived, bottom left - ten years after the He shell explosion and bottom right 500 years after the merger

rates of neutron production by different channels at a few stage of the merger.

The top left panel shows neutron production rates at the start of the merger, when no hydrogen from the secondary has yet penetrated into the primary core. You can see there three maxima: first one is inside the carbon core. This site of the neutron production does not have any interest for us: unless completely destroyed during the merger, the core material will not get mixed with the envelope during the further stellar evolution. The second maximum is placed exactly within the He burning convective shell. The rates quickly drop down as one moves outwards: the temperature decreases, but all the species are mixed inward. The third maximum is placed close to the edge of the He convective shell, in the radiative region (it drops sharply at the core side since species there start to be mixed with the He convective shell). Till the start of the He shell explosion the picture does not change much, except that the third maximum becomes slightly smaller due to the decrease in the temperature (see also Fig. 5.7 and Fig. 5.8).

The top right panel shows the rates during the explosion: all the rates drop significantly due to the decrease in temperature, apart from the (α, n) reaction on the ^{13}C, where the rates is compete by an increase of the hydrogen abundance, this reaction takes place at the boundary of the expanding core. The middle left panel shows the rates immediately after the explosion: there almost neutron production rates falls down.

As mentioned in subsection 5.3.5, we considered two scenarios for the secondary. In the right middle panel we presented rates at three years after the explosion for the case when the secondary survived. The mostly productive reaction here is the reaction $^{13}\mathrm{C}(\alpha, n)^{16}\mathrm{O}$ (the production of ^{13}C is started in CN-cycle, which is ignited due to the fall of the hydrogen on the naked carbon core). The neutron flux produced by this site is high enough to be considered as significant for the s-process, if the evolution will proceed with the same behavior for at least a few decades.

At the bottom left panel we show the same for the case when the secondary has been disrupted by the explosion. The neutron production keeps these rates for a couple of hundred years and increases afterward (see right bottom panel). These rates keep the same order of magnitude value for a few thousand years.

In Fig. 5.12 we show the neutron exposition within the primary star as a function of the mass during and after the merger. The neutron exposition there is found as

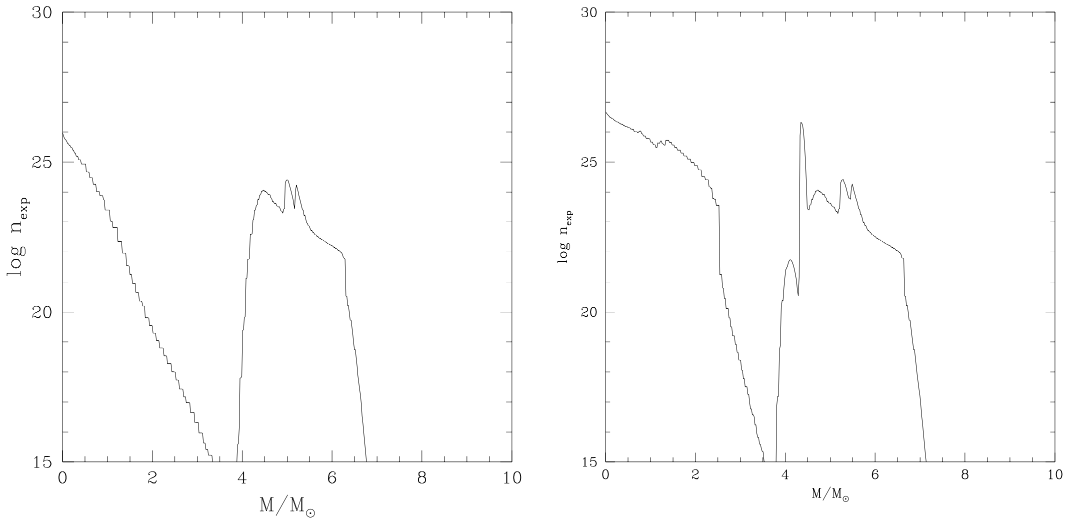

Figure 5.12: The neutron exposure as a function of the mass coordinates. Left panel shows the case with a surviving secondary, right panel with q destroyed secondary.

$$n_{\rm exp}(m) = \int n_n(m) v_n(m) dt \ , \tag{5.6}$$

where n_n is the neutron concentration, v_n is the characteristic Maxwell velocity of neutrons.

We want to point out that the case with the surviving secondary (left panel) takes into account only 3 years after the He shell explosion. If the rates of neutron production keep the same level as in Fig. 5.11, one may expect significant s-processing. Currently the main contribution came from neutron production in the He convective shell during quiet stages of the merger, and is not much different from one may expect from normal stellar evolution. These rates are just slightly higher than in a normal SG star, since our He convective shell expanded slightly in reaction to the spiral-in. Another positive moment is that in our case product will be mixed with the outer envelope. The right panel in Fig 5.12 shows the neutron exposition for the case with a destroyed secondary (integrated over approximately two thousand years). It has a well recognizable spike, with a value (a few 10^{26}) that implies that at this place significant s-processing definitely takes place. And what is more important, it is placed within the convective envelope.

5.3.9 The post-merger evolution

In a number of studies it has been shown that a star that would otherwise become a red supergiant can end its evolution as a blue supergiant if the ratio of core mass to total mass is decreased either

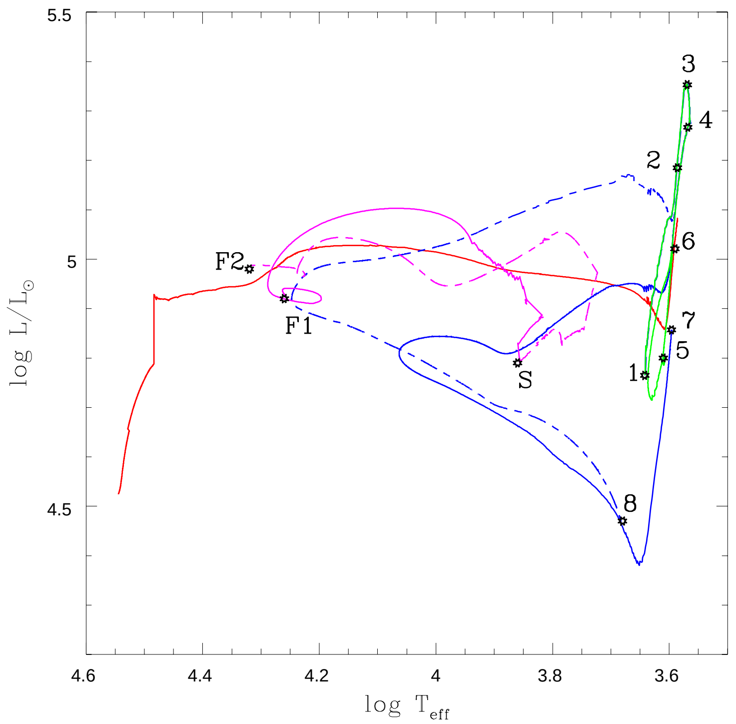

Figure 5.13: Evolutionary tracks: red – normal evolutionary track of a $18M_\odot$ star; magenta solid and magenta dashed – He layer is mixed by different 2 methods (see text); green – the spiral-in and the merger (model A); blue solid and blue dashed lines – the merger model with additional mixing (slow and fast, respectively), models B and C.

by accretion of matter or a reduction of the core mass (Podsiadlowski & Joss 1989; Podsiadlowski, Rappaport & Joss 1990) and/or if the helium abundance in the envelope is increased (Saio, Nomoto and Kato 1988b ; Barkat and Wheeler 1988; Podsiadlowski, 1997). For a metallicity of $Z = 0.02$, Podsiadlowski, Joss & Hsu (1992) found that the critical mass ratio was 0.27, while Saio *et al.* (1988b) typically required a helium abundance larger than 0.35 (for a metallicity of $Z = 0.005$) or larger than 0.53 (for a metallicity of $Z = 0.02$). However, all the results of the merger simulations which we have discussed so far did not show any tendency for the primary to become a BSG. One of reasons might be that the models considered are at the critical limit for stars to become blue (in respect to the core/total mass ratio). Another reason is that, once mixed, the star needs to have at least few thousand years for the thermal relaxation before it will become blue, but the models considered have been taken just too close to the point of carbon core ignition. In this subsection we will discuss the post-merger evolution for stars much younger at the start of the merger. The main aim of this investigation is to define whether and under what conditions a merger product becomes blue.

For this purpose, we evolved a $18\,\mathrm{M}_\odot$ star of LMC composition, with no overshooting, aiming to have a smallest possible core mass at the start of the AGB (to fulfill the known conditions for the star to become blue) (see Fig. 5.13, where the red line represents the evolutionary track of this star). This model was calculated using the Ledoux criterium. We picked up the model where a carbon core has already been formed, but the central temperature is still not very high: $\log T_c = 8.55$ (the star is not at the AGB at this moment). The star has a He-rich shell from $3\,\mathrm{M}_\odot$ till $5.5\,\mathrm{M}_\odot$; and the model has about 25000 years left before carbon core burning.

We insisted on a mass loss of $2\,\mathrm{M}_\odot$ and mixed all layers from $4\,\mathrm{M}_\odot$ to the surface. The first method we used for the mixing was like the method employed by Podsiadlowski, mixing gradually by a small amount going from the outer part. That assumes that convection acts very fast and everything is always uniformly mixed in convective regions. The second method is when we increased the mixing zone starting from the He layer to the surface . Here we calculated the mixing together with the nucleosynthesis, having changes of the composition profile on a realistic time scale even in the envelope. This method produces the mixing in the He layer close to what would have occurred during the merger, though we limited the rate with which this zone expanded and therefore it was not of very intensive burning near the core. The amount of the mixed He is roughly the same for both stars and both stars became BSG, although by slightly different paths, and this difference is probably caused by the difference in the type of mixing – see Fig. 5.13, where the first model is represented by the magenta solid line, and the second model by the magenta dashed line. Both of them start their evolution at point S and have different final points; the final He abundance in the envelope is 0.45 for the first model and 0.475 for the second (He/H by numbers are 0.21 and 0.23, respectively). The increasing of the extension of the blue loop for the model with higher He abundance is consistent with conclusions of Saio *et al.* (1988b). We stopped calculations when carbon was exhausted in the core. Also, we want to note that by the end of the mixing the central temperature has decreased to $\log T_c = 8.44$. The success of these models to become blue proves that our code is able to create a BSG with the same conditions as other groups.

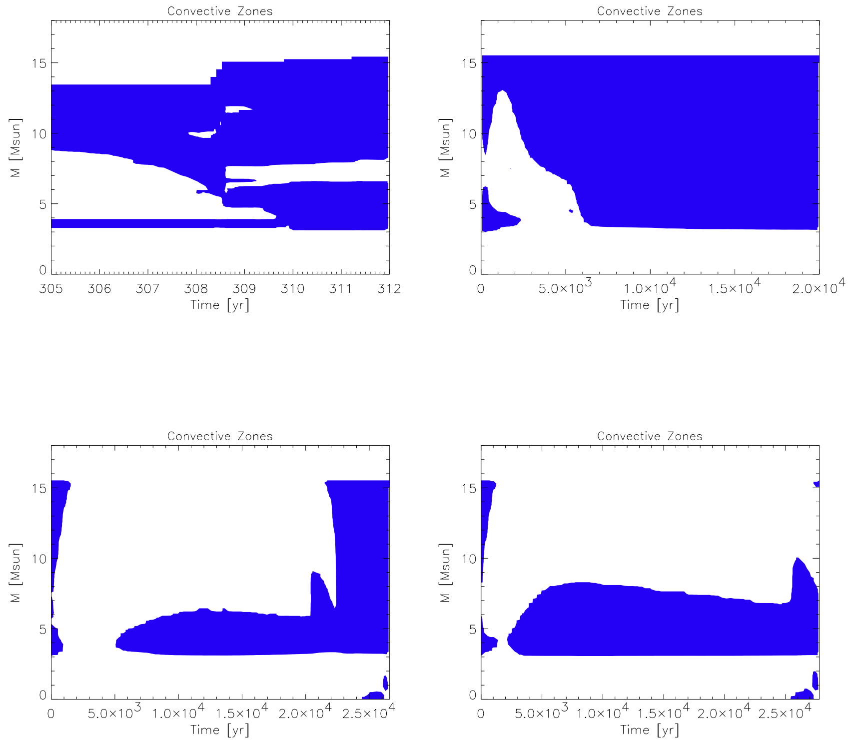

Figure 5.14: Locations of convective regions (by mass) for the merger: the left top panel – the spiral-in and the merger, right top panel – no additional mixing (model A), left bottom – slow mixing down to 3.22 $M_\odot$ (model B), right bottom – faster mixing down to 3.22 $M_\odot$ (model C).

As far as we have been ensured that this star can became blue, we insisted on further 2 $M_\odot$ loss, waited until the star relaxed, which has happened when $\log T_c = 8.57$ and started to do the spiral-in with a secondary of 2 $M_\odot$, which will give in result the same total mass 16 $M_\odot$(see the green line in Fig. 5.13, start is at the black point 1 – here the star already has only 14 $M_\odot$). During the spiral-in the primary evolves fast up on the AGB (points 1-2) and performs the upper loop during the merger (points 2-4). The point 2 in Fig. 5.13 corresponds to the start of the merger (about 300 years after the start of the spiral-in), the point 3 – to the end of the He shell explosion and the point 4 – to the end of the merger; the merger lasts about 8 years and the fast, "He explosive", part lasts for about one year. Also we would like to mention that the injected hydrogen continues its burning after the merger has been completed. For this star, according to its structure, we used for the stream-core interactions an entropy change coefficient of 0.1. The resulting effective stream penetration depth was down to 3.2 $M_\odot$, which though was not mixed thoroughly immediately. Instead we obtained two separate convective zones, which were connected to each other only for a small period of time during the merger (see Fig. 5.14, the top left panel). The merger type was of the "explosive" variety, but without eroding the carbon core. At the end of the merger the He abundance in the envelope was only 0.36. The central temperature during the merger drops quickly, by the end of intensive hydrogen burning it is only $\log T_c = 8.4$. During the relaxation, the star evolves down on the AGB (the star contracts). Once the thermal relaxation has finished, the star again climbs up the AGB. At point 5 the outer convective zone connects with the mixed internal zone and the outer He abundance becomes 0.48. This delayed dredge-up happens 6000 years after the merger has been completed (see Fig. 5.14, the top right panel). The dredge-up, except of He and CNO should dredge-up s-process elements if they have been formed inside the star. Now this model has a very high He abundance in the envelope and it has a core/total mass ratio of only 0.19. Therefore both conditions to become a BSG are satisfied. Nevertheless, as the calculations have shown, this star does not become blue. The star continues its evolution on the AGB; the calculations have been stopped after carbon burning had formed an oxygen core of about 1.2 $M_\odot\tilde{}$(see Fig. 5.13, point 6).

The failure of this model to produce a BSG has shown that the satisfaction of conditions described earlier is not sufficient to create a blue giant in our case. And the known question *why do stars not become blue giants?* is raised again. This question is related to the question which

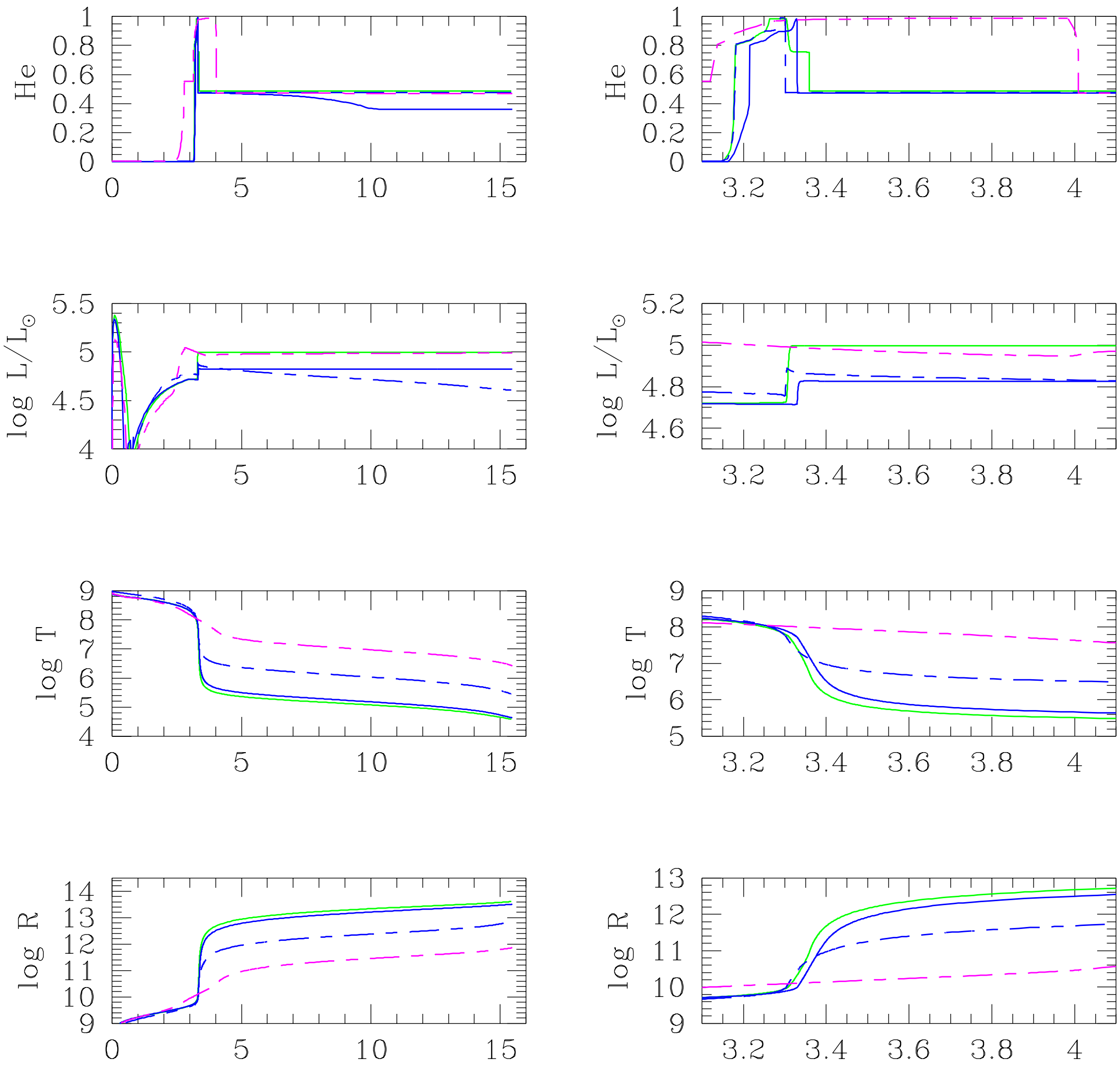

Figure 5.15: Structure of the primary star close to the point of carbon core burning for 4 different models, colors and type of lines corresponds to the ones in Fig. 5.13

was discussed already for more that few decades : *" why do stars become red giants?"* (e.g., Eggleton and Faulkner 1981, Renzini *et al.* 1992, Faulkner 1997, 2000). Some of the suggested and considered criteria were based on the core/total mass ratio (should be smaller than a certain value), the core density, the energy sources, the composition in the envelope, the change of the adiabatic index in the envelope. The case described is a perfect example of stars of very similar structures. The composition in the envelopes, rich in He, is quite similar to each other. But they have very different fate. Hence the limits described above are non sufficient for the determination of when a merger product will became a blue giant or a red giant. Therefore we started a systematic investigation, varying the original model and the details of the merger:

A — $18\,\mathrm{M}_\odot$ star which experienced mass loss of $4\,\mathrm{M}_\odot$.

B, C — Models with insisted artificial mixing *after* the merger as in model A, from the core boundary to the top. In model B the additional mixing has been performed down to 3.32, so the actual size of the core is 3.32, where 3.22 is the mass of the core during the merger. Also, B has faster mixing than C.

D, E, F — The same as the original model A at the start of the spiral-in, but interacted with a more massive secondary and with varied efficiency for the penetration depth.

G, H, I — The modified model A, for which the efficiency of the merger at the end of the merger (the penetration depth) has been decreased. For models H and I the additional mass of 1 $M_\odot$ and 2 $M_\odot$, respectively, has been added after the merger to the envelope (the added mass has the same composition as the envelope).

J — 18 $M_\odot$ star, taken before it entered the red giant region.

As our calculations in Chapter 2 have shown, the inner part of the primary star accumulates significant amounts of angular momentum. Most of the injected orbital angular momentum of course is concentrated in the differentially rotating convective envelope, but it also should become important that the angular velocity in the central region is very high, $\Omega \approx 10^{-4}$ [rad sec^{-1}]. Rotating uniformly during the spiral-in phase, radiative zones (above the core) will become differentially rotating in the post-merger stage. In such a case within a radiative zone some mechanisms of rotationally induced angular momentum transport might work, e.g. at least transport as the meridional circulation and the turbulent diffusion (Zahn 1992). We cannot currently make a completely realistic estimate for the rate of this diffusion. Also, it is probably not the only mixing mechanism working in these regions. But we can perform the simulation in which our star will experience an additional mixing at some rate in the radiative regions (more precisely, in radiative regions which have been disturbed by the stream-core interaction). Assuming that, we insisted on the additional mixing in the radiative zones after the merger (point 4, see Fig. 5.13), with the corresponding constant velocity of 300 cm/sec and with faster mixing with the velocity of 3000 cm/sec[3]. The result of these calculation are shown as blue solid and blue dashed lines in Fig. 5.13. These models make the blue loop, though the first one ends its evolution also on AGB (point 7), and the second is almost back to the AGB (point 8).

The qualitative difference between these 2 models and model A is that apart of the increase of the He abundance in the envelope at an earlier stage, the mixing helps to keep a sharp gradient of hydrogen at the edge of the core (see Fig. 5.15). The importance of the steepness of the hydrogen abundance in an evolved star of intermediate mass in respect to the development of blue loops during the stage of central helium burning has been discussed in Lauterborn (1971a,b). The star we are looking at is much more evolved and more massive, but the interesting point is that we have to deal with a star with a carbon core where the helium shell source dropped its luminosity due to the carbon core expansion and the hydrogen shell source taking over (see Fig. 5.15).

The next group of models we looked at , models D, E and F, is when the secondary is more massive, this, firstly, helps to decrease the core/total mass ratio and, secondly, it naturally limits the penetration depth of the stream since the secondary has a higher entropy. In these simulations all the stars performed a blue loop (see Fig. 5.16). The behavior of these models at the moment of deepest dredge-up has been found to be very similar (see Fig. 5.17), and it also has been found that in these models the outer convective zone does not create a common convective zone with the hydrogen burning zone even temporarily. At the blue stage the star which has larger core, developed a more massive convective zone above the core. Also, the smaller remnant core has a

[3]The value for the velocity of the meridional circulation in these conditions will be rather 3 cm/sec

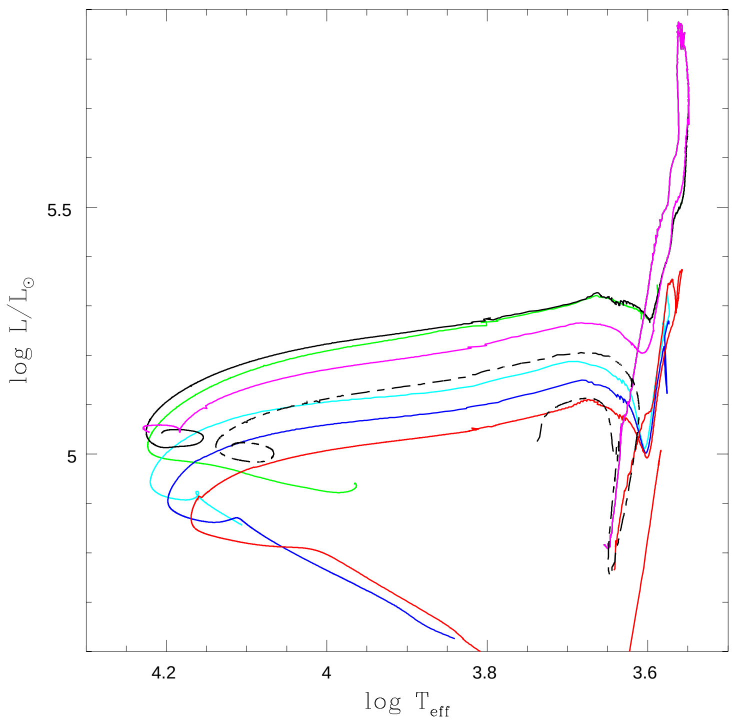

Figure 5.16: Evolutionary tracks for the merger and post-merger epoch: green – model D, black - model E, magenta – model F, red – model G, blue – model H, cyan – model I, black dashed – model J.

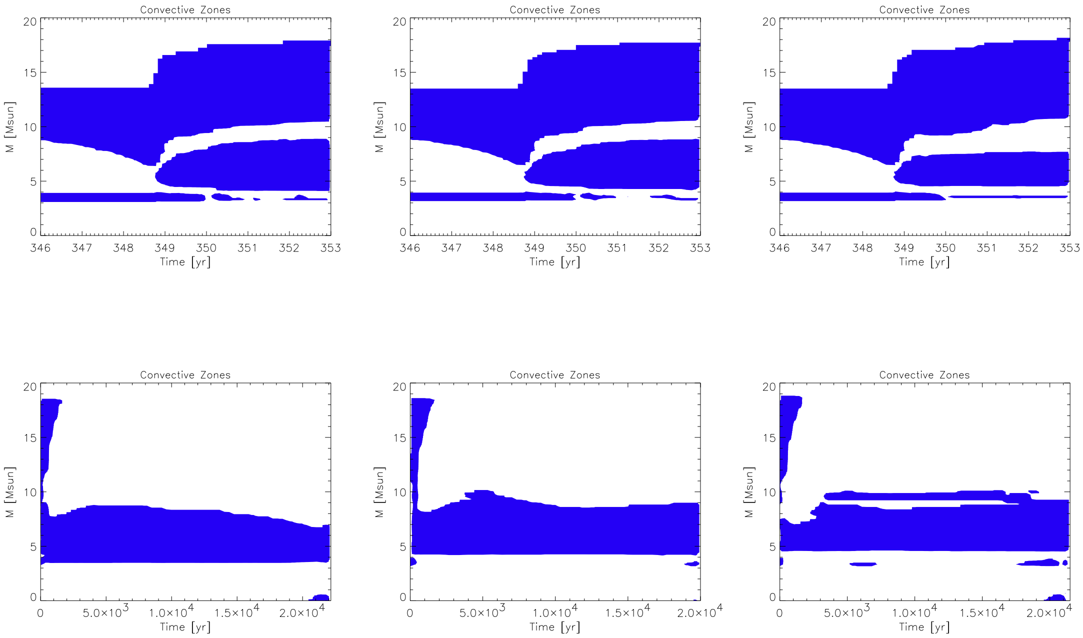

Figure 5.17: Locations of convective regions (by mass) near the moment of the deepest dredge-up (top panels) and complete post-merger evolution (bottom panels). From left to right: models D,E and F.

larger temperature decrease in the center of the core during the merger, and correspondingly, has a larger core expansion. The final surface composition in these models are almost the same and defined by the dredge-up during the merger (see Table 5.1).

Models G, H and I are models where we limited the efficiency of the stream penetration at the end of the merger (it is rather likely that the merger will not run with the same k_s as at the start of the merger – the star expands and changes its structure, the core region becomes rapidly rotating e.t.c.). As a result we created a merger product with a larger core mass. Also, since this core has been cooled less during the merger than in model A, the evolutionary time scale becomes shorter. All the models performed the blue loop, and the amplitude of this loop depends on the total mass of the star (see Fig.5.16). The time-scale of evolution for these model is close to each other, and therefore the question whether the star will end up as a red-giant or as a blue giant will be defined by its total mass (or by how far to the blue region the star evolved during the loop) – the more massive star has is more likely to end its evolution as a blue giant. At the same time, models D, E and F have shown that the post-merger time scale depends on the core mass and/or the core minimal

Table 5.1: Description of models and results of the merger calculations for a 18 $M_\odot$ primary (ZAMS mass).

Model	M_s	M_f	M_c	$\log T_c$	R_c/R_c^0	$\log T_{eff}$	$\log L$	He/H	N/C	N/O	τ[y]
A	2	16	3.22	8.41	1.9	3.59	5.02	0.24	9.9	3.1	25,000
B	2	16	3.22	8.41	1.9	3.60	4.86	0.145	4.6	1.3	26,500
C	2	16	3.22	8.41	1.9	3.68	4.47	0.23	35.1	3.0	28,000
D	5	19	3.62	8.44	1.86	3.97	4.94	0.14	3.8	1.2	22,600
E	5	19	4.32	8.51	1.55	4.21	5.04	0.14	3.8	1.2	21,000
F	5	19	4.68	8.54	1.43	4.22	5.04	0.14	3.8	1.2	21,000
G	2	16	4.08	8.48	1.62	3.67	4.39	0.15	4.7	1.3	22,000
H	2	17	4.08	8.48	1.62	3.84	4.63	0.15	4.7	1.3	23,000
I	2	18	4.08	8.48	1.62	4.11	4.86	0.15	4.7	1.3	21,000
J	2	20	4.00	8.47	1.74	4.12	5.02	0.1	0.39	0.23	21,700

Note. – M_f is the mass of the merger product, M_c is the mass of the resulting core, $\log T_c$ is the minimal temperature in the center of the core during the merger, $R_{c,d}/R_{c,i}$ is the maximum expansion of the core (which is defined as M_c) during the merger, $\log T_{eff}$ and $\log L/L_\odot$ are final effective temperatures and luminosities, He/H, N/C and N/O are final surface abundances (by number) and τ[y] is the lifetime of the merger product after the merger till the start of carbon core burning.
For evolutionary tracks see Fig. 5.13 and Fig. 5.16.

temperature during the merger.

Considering models D-I, we traced how the structure of the star changes when it is evolving into the blue region and and when it again wants to became a red giant. Fig. 5.18 presents the structures of models G and E for these moments. It can be seen that both stars have a more significant hydrogen shell source when they travel toward the blue region, and on its way to the red giant region stars have a dominant helium shell source.

One of the interesting issues is what would be happen if the star came into the common envelope phase when it does not develop a deep convective envelope. Model J represent the model of the star, taken before it became a red giant. This star also ended up as a BSG, but what is interesting, is that it does not change the surface composition (see Table 5.1), and that is explained by the time evolution of the convective zones during the spiral-in, the merger and post-merger effects. In such a case we have a BSG which has almost a normal surface composition, but the structure of the internal layers is very different from a normal star.

The last group of models we looked at was the group of models based on the originally evolved 20 $M_\odot$ star, of LMC composition, with overshooting 0.1. This star has a carbon core of 4 $M_\odot$ and a He core of 6.2 $M_\odot$. For model K we assumed a pre-merger mass loss of 4 $M_\odot$, models L and M at the start of the spiral-in have the original mass of 20 $M_\odot$, model L has the smallest

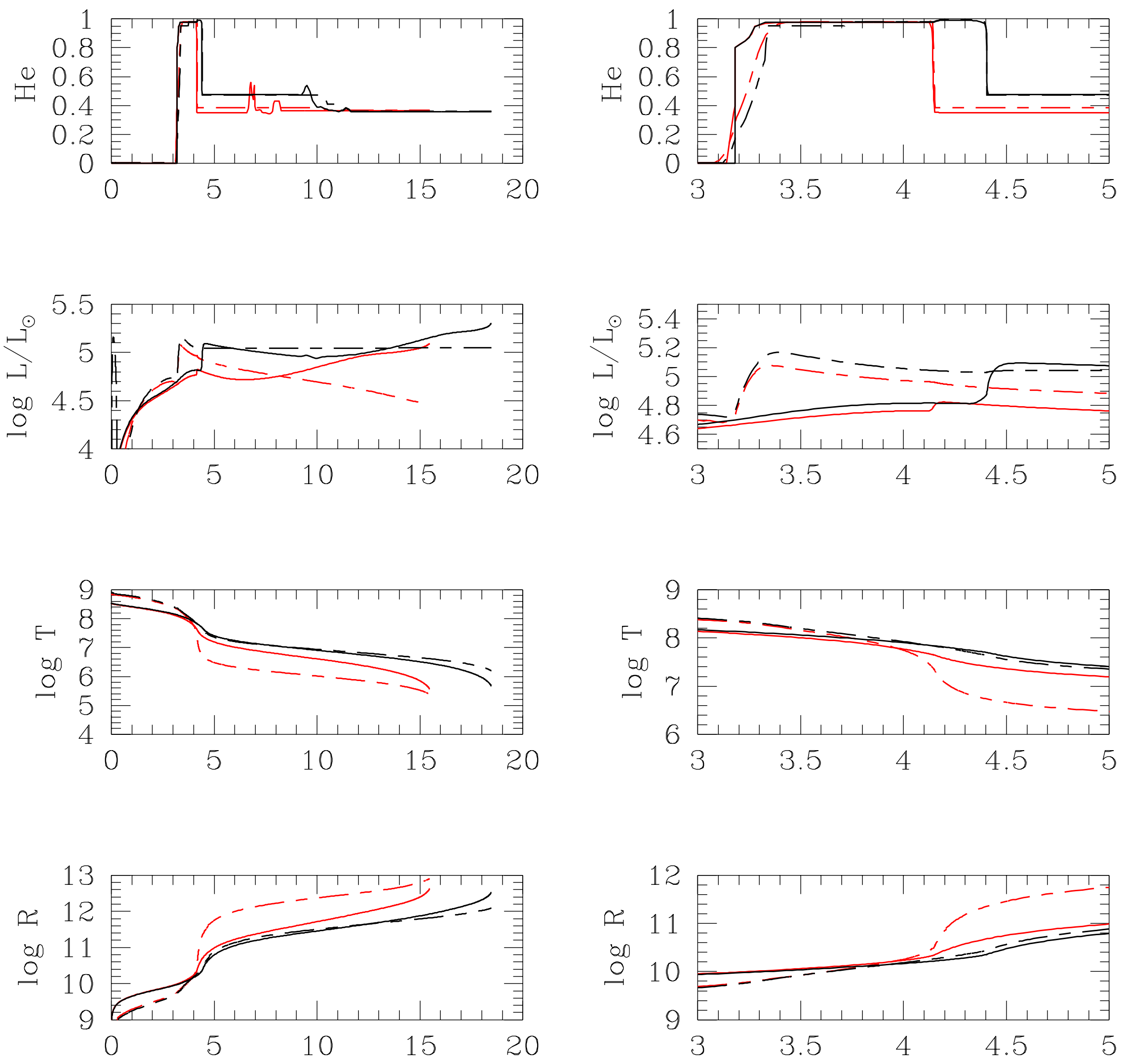

Figure 5.18: Structure of the primary star for model G (red) and model E (black) (see also Fig. 5.16). Solid lines for models of $\log T_{\rm eff} = 3.7$, when a star evolves toward the blue region, dashed lines shows the $\log T_{\rm eff} = 3.7$ point for model G on its way to the red giant region and the final model in the blue region for model E.

Table 5.2: Description of models and results of the merger calculations for the $20\,M_\odot$ primary

Model	$M_{\rm s}$	$M_{\rm f}$	$M_{\rm c}$	$\log T_{\rm c}$	$R_{\rm c}/R_{\rm c}^0$	$\log T_{\rm eff}$	$\log L$	He/H	N/C	N/O	τ[y]
K	2	18	4.95	8.62	1.4	3.60	5.06	0.20	12.3	1.4	8 300
L	2	22	4.07	8.34	2.7	3.60	5.08	0.19	0.95	0.54	19 300
M	2	22	4.95	8.62	1.5	3.99	5.04	0.12	3.0	0.48	8 700

Note. – Notations are the same as in Table 5.1.

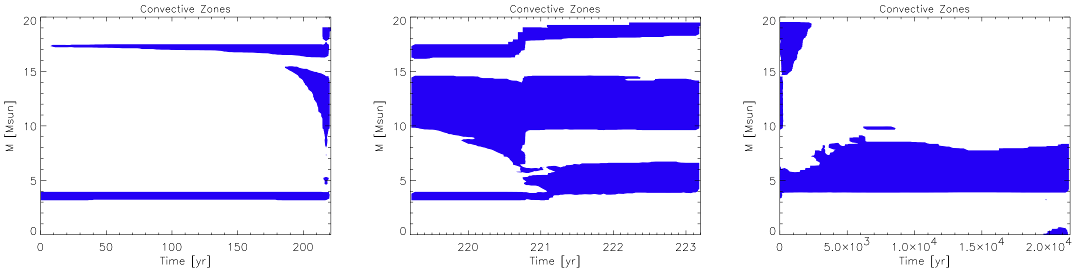

Figure 5.19: Locations of convective regions (by mass) during the spiral-in (left) near the moment of the deepest dredge-up (middle) and complete post-merger evolution (right) for models J.

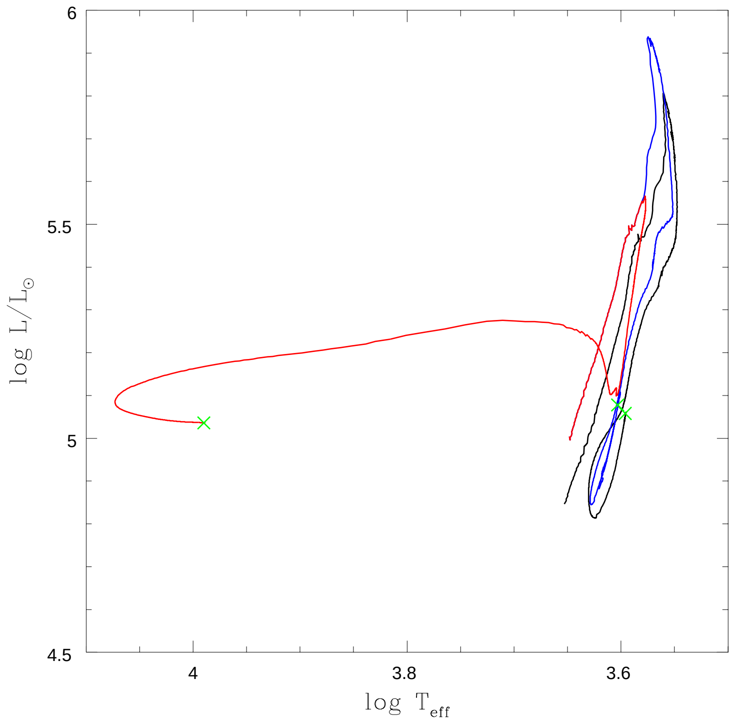

Figure 5.20: Evolutionary tracks for the merger and post-merger epoch: black - model K, blue – model L, red – model M. Green crosses represent end points of the evolution for the each model. L and M models have the same starting point.

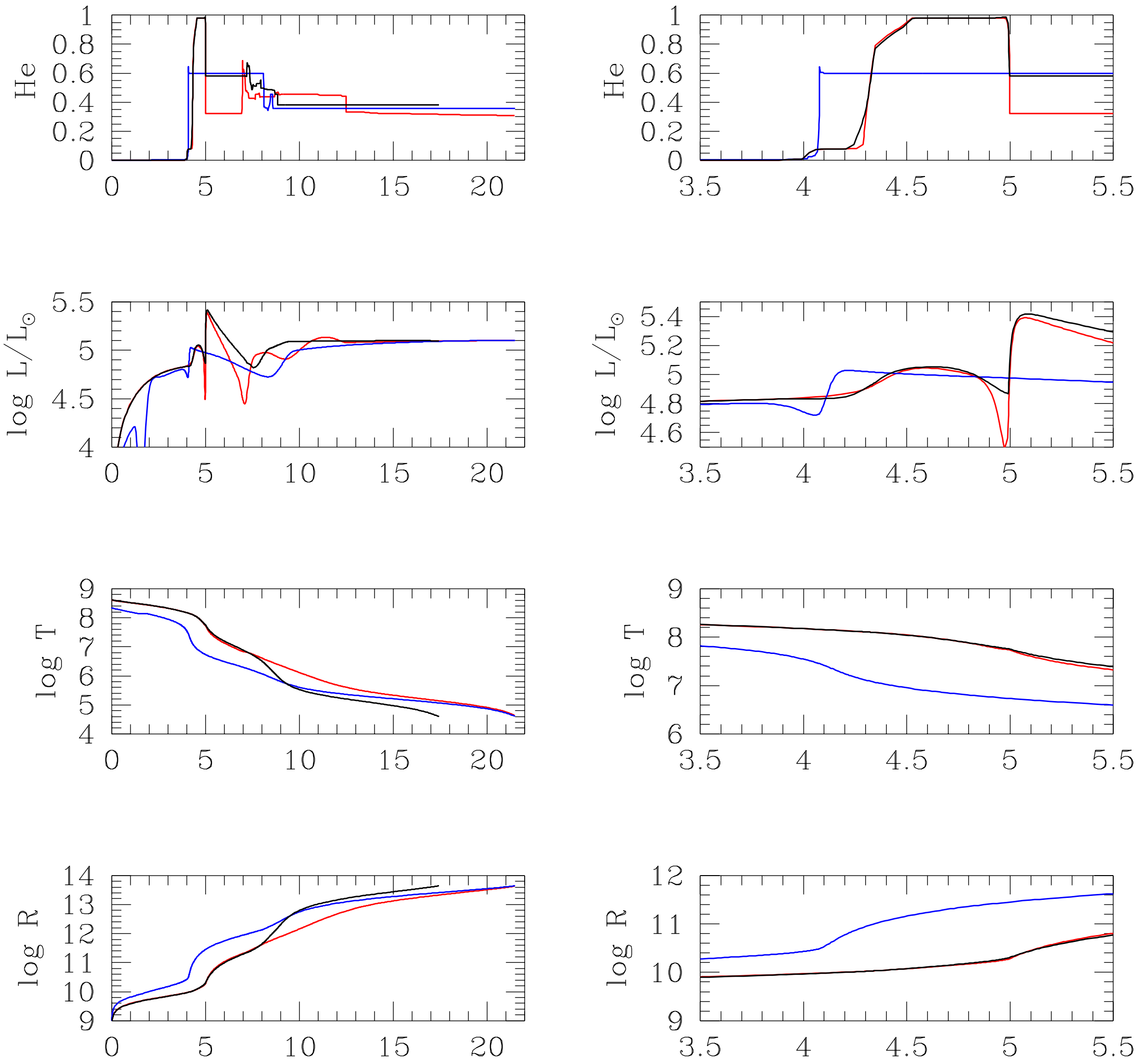

Figure 5.21: Structure of the primary star for model K (black) and model L (blue) and M (red) at the moment when the luminosity of the merger product after the merger has decreased to $\log L = 5.1$ (see also Fig. 5.20).

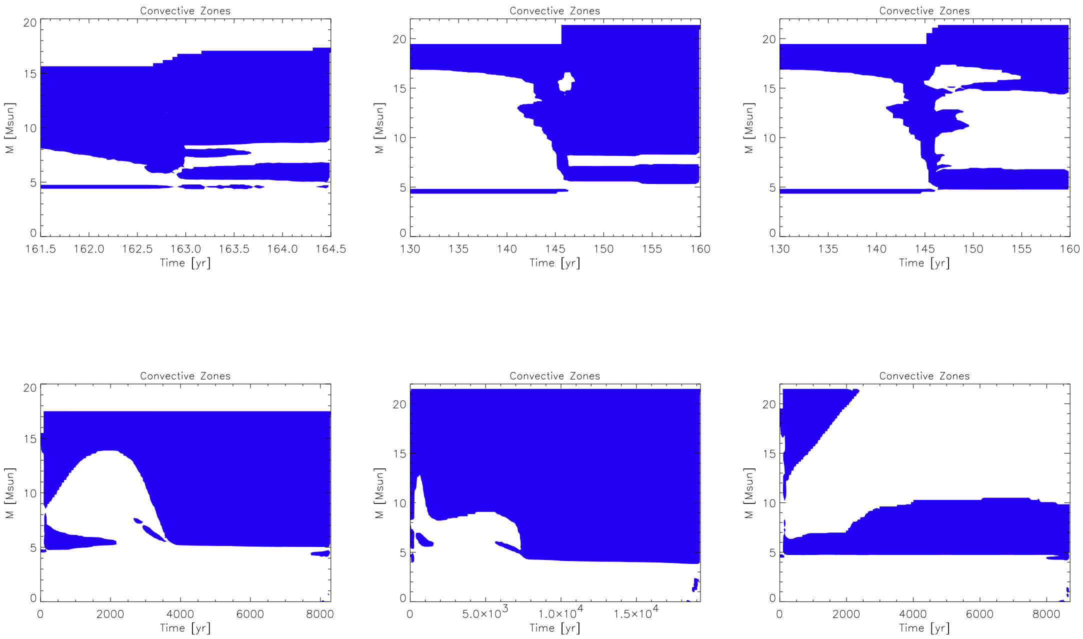

Figure 5.22: Locations of convective regions (by mass) near the moment of deepest dredge-up (top panels) and the complete post-merger evolution (bottom panels). From left to right: models K,L and M.

core, and the cores of models K and M are the same (see Table 5.2). Consistent with previous results, the calculation have shown that the only star where core did not experience deep dredge-up and which has the smallest core/total mass ratio became blue: model M (see Fig. 5.20). The role of the core/total mass can be clearly seen by comparing the internal structure of these models at the moment when all of them have decreased their luminosity after the merger to $\log L = 5.1$ (see Fig. 5.21) : models K and M have almost the same structure in the core region, but only M became a blue supergiant. The very special point we would like to note, is that although the N/C and N/O are small for model L, this is a model where the carbon abundance is very high: it is 13 times higher than before the spiral-in starts.

In general, combining the results from the calculated models, we can conclude that in the case of the merger one of the very important parameters of whether a star will move into the blue region is the efficiency of the hydrogen shell source. On the other hand, if the mass of the envelope is smaller than a certain value, the star will not evolve to the blue region even if it develops a hydrogen shell source. It is interesting that in the case of too strong erosion of the core, when the helium shell has been mixed with almost the entire envelope, a star will not proceed to the blue region. One of the possible explanation is that at the edge of the carbon core it is not possible to create a sharp gradient in the hydrogen profile, which has been found necessary for the blue giant stage. Stars which have evolved as blue giants, can have overabundances of Helium in the envelope, though typically near the the lowest range consistent with 87A, which has been determined as $\mathrm{He/H} = 0.25 \pm 0.05$ by Lundqvist and Fransson, 1996. Values for the N/C and N/O ratios are consistent with those for 87A: $\mathrm{N/C} = 6.1 \pm 1.1$ and $N/O = 1.7 \pm 0.5$ (Sonneborn *et. al* 1997). Stars which stays as red giants, have stronger He overabundances and in some cases very significant carbon overabundance. These objects may look like the carbon rich supergiant V Hydrae which is also a possible post-merger product.

5.4 Dicussion and Conclusions

This chapter has been devoted to the study of the processes which happen during the merger of a main-sequence secondary with the core of an evolved massive primary star during the common envelope stage of their evolution. Modelling the merger processes involved the modelling of the nucleosynthesis simultaneously with the mixing. We discussed the importance of several aspects which affect the result of the merger, such as the efficiency of the penetration depth, the evolutionary stage of the primary at the start of the merger, the role of convection and the importance of the secondary mass. Based on this study our main conclusions are the following:

- The key feature which determines the response of the primary during the merger are the locations and the further interactions of convective zones (either those that existed initially or those that were created during the merger). Depending on their evolution and interactions, the merger can follow either a quiet path or an explosive regime during which the core expands significantly.

- The evolutionary stage of the primary at the start of the merger is important since a) it defines the mass and the location of the helium-burning convective shell, which can later interact with the intermediate hydrogen-rich convective zone; and b) it defines the development of the outer convective zone (if the star starts the spiral-in when it did not yet have a deep outer convective zone and becomes a blue supergiant after the merger, there may be no change in surface abundances).

- The actual penetration depth is important since it determines the location of the intermediate hydrogen-rich convective reservoir. The penetration depth is a function of the primary structure (pressure and temperature gradient, or in other words of its age) and of the secondary mass (through its entropy).

We can conclude from this that the envelope of the merger product will likely be overabundant in helium if the CE stage started when the primary has not yet developed too steep a pressure and temperature gradient (but has a well developed He convective shell) or if the secondary has a low entropy (i.e. the mass of the secondary is less than $\sim 2\,\mathrm{M}_\odot$).

As the result of our systematic study of the post-merger evolution we have identified 3 different types of behavior of the convective zones during and after the merger, depending on different initial conditions.

– *Quiet merger.* During this merger the material from the secondary only gently touches the part of the helium layer, which becomes a part of the outer convective envelope (see e.g. Fig. 5.4).

– *Moderate merger.* A moderately explosive merger where only part of the He core expands. In this case the outer convective envelope may dredge up part of the He-rich layer, but an extensive He shell still remains (see e.g.Fig. 5.17). The merger does not necessarily cause significant changes of the surface composition. The hydrogen shell source may become the dominant nuclear source for an extended period of time.

– *Explosive merger.* During the explosive merger such a large amount of the core is ripped off that during or after the merger the envelope convective zone merges with the intermediate convective zone to form a large single convective zone all the way down to the core. This produces large changes in the surface abundances both during the merger itself (see e.g. Fig. 5.9) and during the subsequent delayed dredge-up (Fig. 5.14).

We have shown that only the products of a "moderate merger" scenario, with a temporarily dominant hydrogen shell source, can become a BSG, though this depends also on the ratio of the core mass to the total mass, which should be smaller than 0.275. We did not find that the helium overabundance in the envelope played a crucial role in determining whether the star became blue or not, although the helium abundance may affect the extent of the blue loops. Quiet mergers do not change the structure of the primary sufficiently to make the hydrogen shell source stronger than the helium shell source and do not decrease the core to total mass ratio as much as the other two types.

Those merger products that stay red supergiants are less luminous immediately after the merger than at the beginning of the spiral-in, but start to evolve up the AGB again after a few thousand years for as long as carbon burning continues. During the contraction stage, which happens immediately after the merger has been completed, the surface layers of the merger product could achieve the critical rotation; as a result we expect significant mass loss.

Significant neutron production occurs only in the scenario with an exploding He-burning shell, either with a surviving secondary or when the secondary is destroyed by the explosion. The key factor here is the absence of a He-burning shell between the convective envelope and the carbon core. The "moderate mergers", investigated so far only showed a moderate enhancement of s-process elements in the envelope.

We conclude that a "moderate merger" provides a good scenario for the progenitor of SN 1987A based on the following criteria:

- It creates a blue progenitor close to the observed position of the progenitor in the H-R diagram: $\log L/L_{\odot} = 5.15 - 5.5$, $\log T_{\rm eff} = 4.15 - 4.25$ (Woosley 1988);
- the progenitor will be overabundant in He (though the present models are near the lower end of the observationally deduced range) and the surface composition of the CNO abundances of the merger product are in good agreement with the abundances determined for the inner ring;
- the time scale for the post-merger evolution is in good agreement with the dynamical age of the inner nebula ($1.5 \div 2 \times 10^4$ y (Crotts and Heathcote 1997; Meyer 1997; Smith *et al.*, 1998);

– no significant carbon overabundance is produced as would be characteristic of the "explosive merger" scenario.

Based on the time-scale of the post-merger evolution, our best estimate of the initial primary mass is $\sim 18\,\mathrm{M}_\odot$. If the primary has experienced strong mass loss before the spiral-in, the mass of the secondary should be larger than $\sim 2\,\mathrm{M}_\odot$.

The case of an "explosive merger" seems to be a good scenario for the creation of objects like V Hydrae, which is a red supergiant apparently rotating near break-up (Kahane *et al.*. 1996) and very overabundant in carbon (even without the erosion of the carbon core, the carbon abundance can be as high [C/H]=8.75 as in model L (≈ 5 times higher than in then LMC), where for V Hydrae it has been found to be [C/H](N)=8.89 (Lambert *et al.* 1986).

Appendix A

Hydrodynamical equations

A.1 Spherical coordinate system

In a spherical coordinate system (r, ϑ, φ), where r is the radial coordinate, φ is the azimuthal angle and ϑ is the polar angle associated with the rotation axis, the momentum conservation equation (2.33) can be written in the form

$$\begin{aligned}
\frac{\partial \rho u_r}{\partial t} + \nabla \cdot (\rho u_r \vec{u}) - \rho \frac{u_\vartheta^2 + u_\varphi^2}{r} &= -\frac{\partial P}{\partial r} - \rho \frac{\partial \Phi}{\partial r} + \nabla \cdot \tau_r + \frac{1}{r}\tau_{rr} + f_r, \\
\frac{\partial \rho r u_\vartheta}{\partial t} + \nabla \cdot (\rho r u_\vartheta \vec{u}) - \rho \frac{u_\varphi^2 \cot\vartheta}{r} &= -\frac{\partial P}{\partial \vartheta} - \rho \frac{\partial \Phi}{\partial \vartheta} + \nabla \cdot (r\tau_\vartheta) + \cot\vartheta \tau_{\varphi\varphi} + r f_\vartheta, \\
\frac{\partial \rho r \sin\vartheta u_\varphi}{\partial t} + \nabla \cdot (\rho r \sin\vartheta u_\varphi \vec{u}) &= -\frac{\partial P}{\partial \varphi} - \rho \frac{\partial \Phi}{\partial \varphi} + \nabla \cdot (r \sin\vartheta \tau_\varphi) + r \sin\vartheta f_\varphi
\end{aligned} \tag{A.1}$$

where $(\tau_r, \tau_\vartheta, \tau_\varphi)$ are the vector components of the viscous stress tensor with $\tau_i = (\tau_{ir}, \tau_{i\vartheta}, \tau_{i\varphi}), i = (r, \vartheta, \varphi)$. In spherical polar coordinates the tensor components are:

$$\begin{aligned}
\tau_{rr} &= 2\eta_{rr} \frac{\partial u_r}{\partial r}, \\
\tau_{\varphi\varphi} &= 2\eta_{\varphi\varphi} \left(\frac{1}{r\sin\vartheta} \frac{\partial u_\varphi}{\partial \varphi} + \frac{u_r}{r} + \frac{u_\vartheta \cot\vartheta}{r} \right), \\
\tau_{\vartheta\vartheta} &= 2\eta_{\vartheta\vartheta} \left(\frac{1}{r} \frac{\partial u_\vartheta}{\partial \vartheta} + \frac{u_r}{r} \right), \\
\tau_{r\vartheta} &= \eta_{r\vartheta} \left(\frac{1}{r} \frac{\partial u_r}{\partial \vartheta} + \frac{\partial u_\vartheta}{\partial r} - \frac{u_\vartheta}{r} \right), \\
\tau_{\varphi r} &= \eta_{\varphi r} \left(\frac{\partial u_\varphi}{\partial r} + \frac{1}{r\sin\vartheta} \frac{\partial u_r}{\partial \varphi} - \frac{u_\varphi}{r} \right), \\
\tau_{\varphi\vartheta} &= \eta_{\varphi\vartheta} \left(\frac{1}{r\sin\vartheta} \frac{\partial u_\vartheta}{\partial \varphi} + \frac{1}{r} \frac{\partial u_\varphi}{\partial \vartheta} - \frac{u_\varphi \cot\vartheta}{r} \right).
\end{aligned} \tag{A.2}$$

Now we reduce the problem to a 2-dimensional problem, assuming that we have axial symmetry. In such a case the stress $\tau_{\varphi\varphi}$ will no longer play any role any more. Taking $u_\varphi = r\Omega(r,\vartheta)\sin\vartheta$, we have

$$\tau_{\varphi\varphi} = 0, \qquad \tau_{\varphi r} = \eta_{\varphi r} r \sin\vartheta \frac{\partial\Omega}{\partial r}, \qquad \tau_{\varphi\vartheta} = \eta_{\varphi\vartheta}\sin\vartheta\frac{\partial\Omega}{\partial\vartheta}$$

$$\begin{aligned}\frac{\partial}{\partial t}\left(\rho r^2\Omega\sin^2\vartheta\right) + \frac{1}{r^2}\frac{\partial}{\partial r}\left(\rho r^4 u_r\Omega sin^2\vartheta\right) + \frac{1}{r\sin\vartheta}\frac{\partial}{\partial r}\left(\rho r^2 u_\vartheta\Omega\sin\vartheta^3\right) \\ = \frac{\sin^2\vartheta}{r^2}\frac{\partial}{\partial r}\left(r^4\eta_{\varphi r}\frac{\partial\Omega}{\partial r}\right) + \frac{1}{\sin\vartheta}\frac{\partial}{\partial\vartheta}\left(\eta_{\varphi\vartheta}\sin^3\vartheta\frac{\partial\Omega}{\partial\vartheta}\right)\end{aligned} \tag{A.3}$$

For a case with $u_\varphi = r\Omega(r)\sin\vartheta$, and including the term accounting for the angular momentum source, this equation finally takes the form of the well known diffusion equation:

$$\frac{\partial}{\partial t}\left(\rho r^4\Omega\right) + \frac{\partial}{\partial r}\left(\rho r^4 u_r\Omega\right) = \frac{\partial}{\partial r}\left(r^4\eta_{\varphi r}\frac{\partial\Omega}{\partial r}\right) + \frac{3}{8\pi}\frac{\partial j}{\partial t} \tag{A.4}$$

The factor $\frac{3}{8\pi}$ arises from the fact that for a thin spherical shell the specific angular momentum $J = \frac{8}{3}\pi r^4\rho\Omega$ – to be consistent with equation (A.4).

A.2 Cylindrical coordinate system

In a cylindrical coordinate system (r,φ,z) the momentum conservation equation (2.33) can be written in the form

$$\begin{aligned}\frac{\partial\rho u_r}{\partial t} + \nabla\cdot(\rho u_r\vec{u}) - \rho\frac{u_\varphi^2}{r} &= -\frac{\partial P}{\partial r} - \rho\frac{\partial\Phi}{\partial r} + \nabla\cdot\tau_r + \frac{1}{r}\tau_{rr} + f_r, \\ \frac{\partial\rho u_z}{\partial t} + \nabla\cdot(\rho u_z\vec{u}) &= -\frac{\partial P}{\partial z} - \rho\frac{\partial\Phi}{\partial z} + \nabla\cdot\tau_z + f_z, \\ \frac{\partial\rho r u_\varphi}{\partial t} + \nabla\cdot(\rho r u_\varphi\vec{u}) &= -\frac{\partial P}{\partial\varphi} - \rho\frac{\partial\Phi}{\partial\varphi} + \nabla\cdot(r\tau_\varphi) + r f_\varphi\end{aligned} \tag{A.5}$$

The stress tensor components are:

$$\tau_{rr} = 2\eta_{rr}\frac{\partial u_r}{\partial r},$$

$$
\begin{aligned}
\tau_{\varphi\varphi} &= 2\eta_{\varphi\varphi}\left(\frac{1}{r}\frac{\partial u_\varphi}{\partial \varphi} + \frac{u_r}{r}\right) , \\
\tau_{zz} &= 2\eta_{zz}\frac{\partial u_\vartheta}{\partial \vartheta} + \frac{\partial u_z}{\partial z} , \\
\tau_{rz} &= \eta_{rz}\left(\frac{\partial u_z}{\partial r} + \frac{\partial u_r}{\partial z}\right) , \\
\tau_{\varphi r} &= \eta_{\varphi r}\left(\frac{\partial u_\varphi}{\partial r} + \frac{1}{r}\frac{\partial u_r}{\partial \varphi} - \frac{u_\varphi}{r}\right) , \\
\tau_{\varphi z} &= \eta_{\varphi z}\left(\frac{\partial u_\varphi}{\partial z} + \frac{1}{r}\frac{\partial u_z}{\partial \varphi}\right) .
\end{aligned}
\tag{A.6}
$$

Now we reduce the problem to a 2-dimensional problem, assuming that we have axial symmetry. In this case the stress $\tau_{\varphi\varphi}$ will not play role any more. Taking $u_\varphi = r\Omega(r,z)\,\mathrm{sin}$, we have

$$
\tau_{\varphi\varphi} = 0, \qquad \tau_{\varphi r} = \eta_{\varphi r} r \frac{\partial \Omega}{\partial r}, \qquad \tau_{\varphi z} = \eta_{\varphi z} r \frac{\partial \Omega}{\partial z}
$$

$$
\begin{aligned}
&\frac{\partial}{\partial t}\left(\rho r^2 \Omega\right) + \frac{1}{r}\frac{\partial}{\partial r}\left(\rho r^3 u_r \Omega\right) + \frac{1}{r}\frac{\partial}{\partial r}\left(\rho r^2 u_z \Omega\right) \\
&\qquad = \frac{1}{r}\frac{\partial}{\partial r}\left(r^3 \eta_{\varphi r}\frac{\partial \Omega}{\partial r}\right) + \frac{\partial}{\partial z}\left(r \eta_{\varphi z}\frac{\partial \Omega}{\partial z}\right)
\end{aligned}
\tag{A.7}
$$

If $u_\varphi = r\Omega(r)$, and including the term accounting for the angular momentum source:

$$
\frac{\partial}{\partial t}\left(\rho r^3 \Omega\right) + \frac{\partial}{\partial r}\left(\rho r^3 u_r \Omega\right) = \frac{\partial}{\partial r}\left(r^3 \eta_{\varphi r}\frac{\partial \Omega}{\partial r}\right) + \frac{1}{2\pi}\frac{\partial j}{\partial t}
\tag{A.8}
$$

The factor $\frac{1}{2\pi}$ is taken to be consistent with the integration over a cylindrical shell, where for the specific angular momentum we have $J = 2\pi r^3 h \rho \Omega$, where h is the height of the cylinder.

Appendix B

An adiabatic stream: the density profile

The condition of lateral hydrostatic equilibrium is

$$\frac{1}{\rho}\frac{\partial P}{\partial r} = -\frac{\partial \Phi}{\partial r} \tag{B.1}$$

The adiabaticity of the stream material $P = S\rho^{\gamma}$ implies that

$$S\gamma\rho^{\gamma-2}\frac{\partial \rho}{\partial r} = -\frac{\partial \Phi}{\partial r} \tag{B.2}$$

In the neighrborhood of L_1

$$S\gamma\int_{L_1}^{r}\rho^{\gamma-2}\frac{\partial \rho}{\partial r}dr = -\int_{L_1}^{r}\frac{\partial \Phi}{\partial r}dr \tag{B.3}$$

And since from the Eq. 3.7

$$\Phi(r) - \Phi_{L1} = \frac{\alpha}{2}r^2\Omega^2 \ , \tag{B.4}$$

we have that

$$S\frac{\gamma}{\gamma-1}\left(\rho(r)^{\gamma-1} - \rho_{\rm c}^{\gamma-1}\right) = -\frac{\alpha}{2}r^2\Omega^2 \ . \tag{B.5}$$

Finally we have the Eq. 3.8

$$\rho = \rho_{\rm c}\left(1 - \frac{\alpha}{2}\frac{\gamma-1}{\gamma}\frac{r^2\Omega^2}{s\rho_{\rm c}^{\gamma-1}}\right)^{1/(\gamma-1)} \ . \tag{B.6}$$

Appendix C

The evolutionary code

This appendix provides a short description of the evolutionary code. The original evolutionary code was written by Kippenhahn et. al (1967) and has been substantially updated and modified by Podsiadlowski, as described in Podsiadlowski (1989). This is a code based on the Henyey method (see Henyey et al. 1959, 1964) which solves the equations of stellar structure for a spherically symmetric star in hydrostatic equilibrium. We made a few modifications to this code. It includes e.g. calculations of nuclear reaction rates and the refining of mesh points (as will be described in detail below). Also additions to the code include calculations of the angular momentum transport, the treatment of the evolution in the presence of a companion (for the primary and for the secondary), the calculation of the nuclear burning together with mixing. These additions have been described in more details in Chapter 2 and Chapter 5. Also it were few minor additions such as taking into account the external gravitational potential, mass loss calculations (rates, loss from the surface and within, mass injection), special outer surface boundary conditions; but these involve rather technical details and will not be described here.

C.1 Nuclear Reactions

C.1.1 Energy generation rates and chemical composition changes

For all the chosen species we form a separate minimized reactions library. The composition changes are calculated implicitly: for each species j at mesh point k, the changes in composition over a time-step dt are defined as a function of reaction rates at the next moment of time:

$$dh_k^j = -dt \sum R_k^j \tag{C.1}$$

This is a 2-dimensional matrix, where h_k^j is the number fraction of species j for the mesh point k and $\sum R_k^j$ is the sum of all the reactions which involve h_k^j as a reactant or as a product.

Optionally, the NRN can be represented by a few sub-networks, where block separations are made at the elements where this division has little effect on the result. This method can be applied only for species involved in the s-process chain (e.g., all the species involved in the hot-CNO cycle have to be in one block). Each additional block in the s-process chain includes neutron composition. In the case of the nuclear burning together with mixing (described in Chapter 5), there is roughly a decrease of order m^2 in the number of operations, where m is the number of new blocks in contrast to the matrix solution of one big block of species:

$$N_{\mathrm{operations}} \approx 5 n_{\mathrm{levels}} n_{\mathrm{species}}^3 + n_{\mathrm{species}}^2 (3 + 6 n_{\mathrm{levels}}) + ...$$

$$\frac{N_{\mathrm{operations}}(n_{\mathrm{species}} = M)}{N_{\mathrm{operations}}(m\ blocks(n_{\mathrm{species}} \approx M/m))} \approx m^2$$

C.1.2 TEST: The hot CNO cycle

The nuclear reactions network has been checked for a region of temperature and density reasonable for the hot-CNO cycle by comparison with the calculations of the hot-CNO cycle (code given by Podsiadlowski). This code is correct for the adopted set of nuclear reactions and their rates. The discrepancies found have been identified as a result of the consideration of additional reactions in the NRN. The removal of those reactions from the NRN led to convergence of the results (see Fig. C.1, which presents the results of calculations by the control hot-CNO code, NRN with the full set of reactions from FTRL and with a reduced and changed set of reactions for two isotopes).

C.1.3 TEST: Time-steps

The implicit scheme which is used for the calculations of the energy generation rate and the species changes could be sensitive to the chosen time step. To check the dependence on time step, we calculated energy production rates as a function of time and as the average energy production rate for the time interval. In theory, for a good result, the energy production rate which is calculated by the code for the full time interval, should be pretty close to the average energy for the same

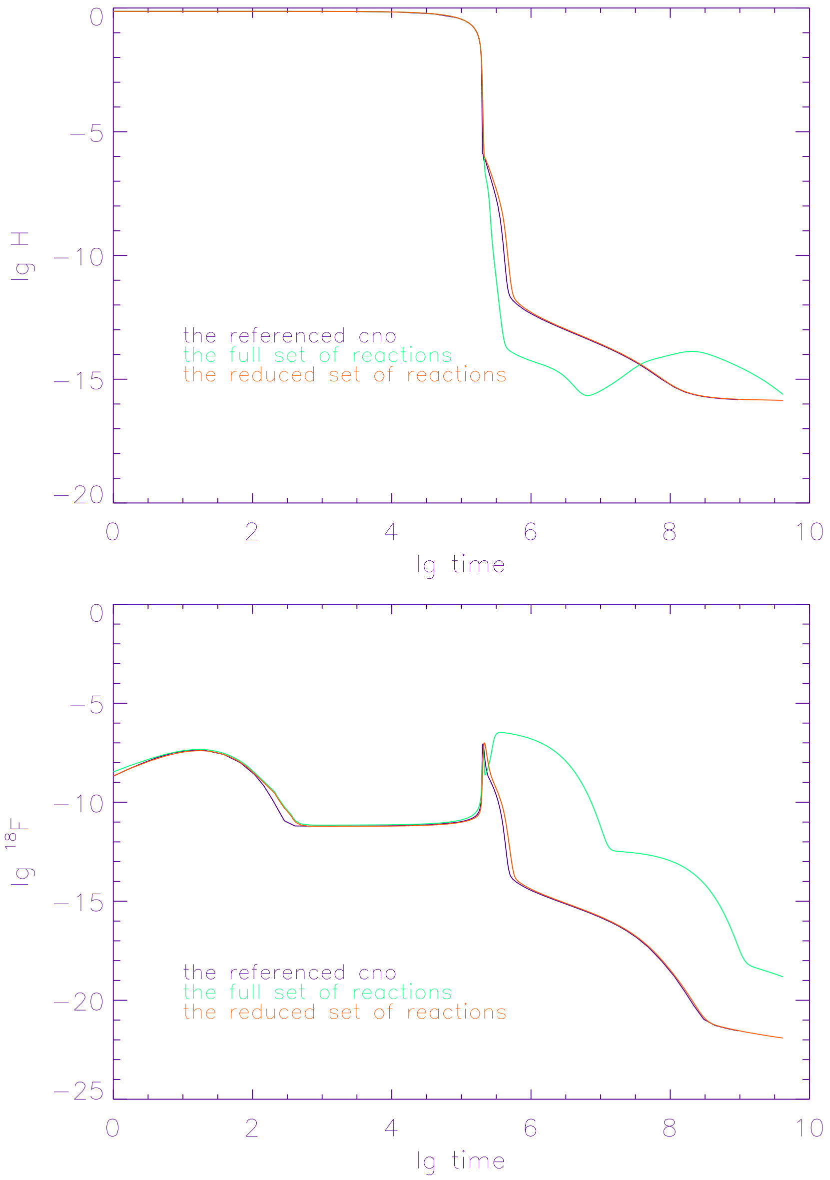

Figure C.1: The evolution of the abundances of H and ^{18}F in the hot-CNO cycle with time, $T_8 = 2.43$, $\rho = 320$ [g/cm^3]. The reference CNO calculation is the calculation using the CNO code given by Podsiadlowski with the reduced set of reactions; the other two correspond to calculations with the NRN using the full and the reduced set of reactions

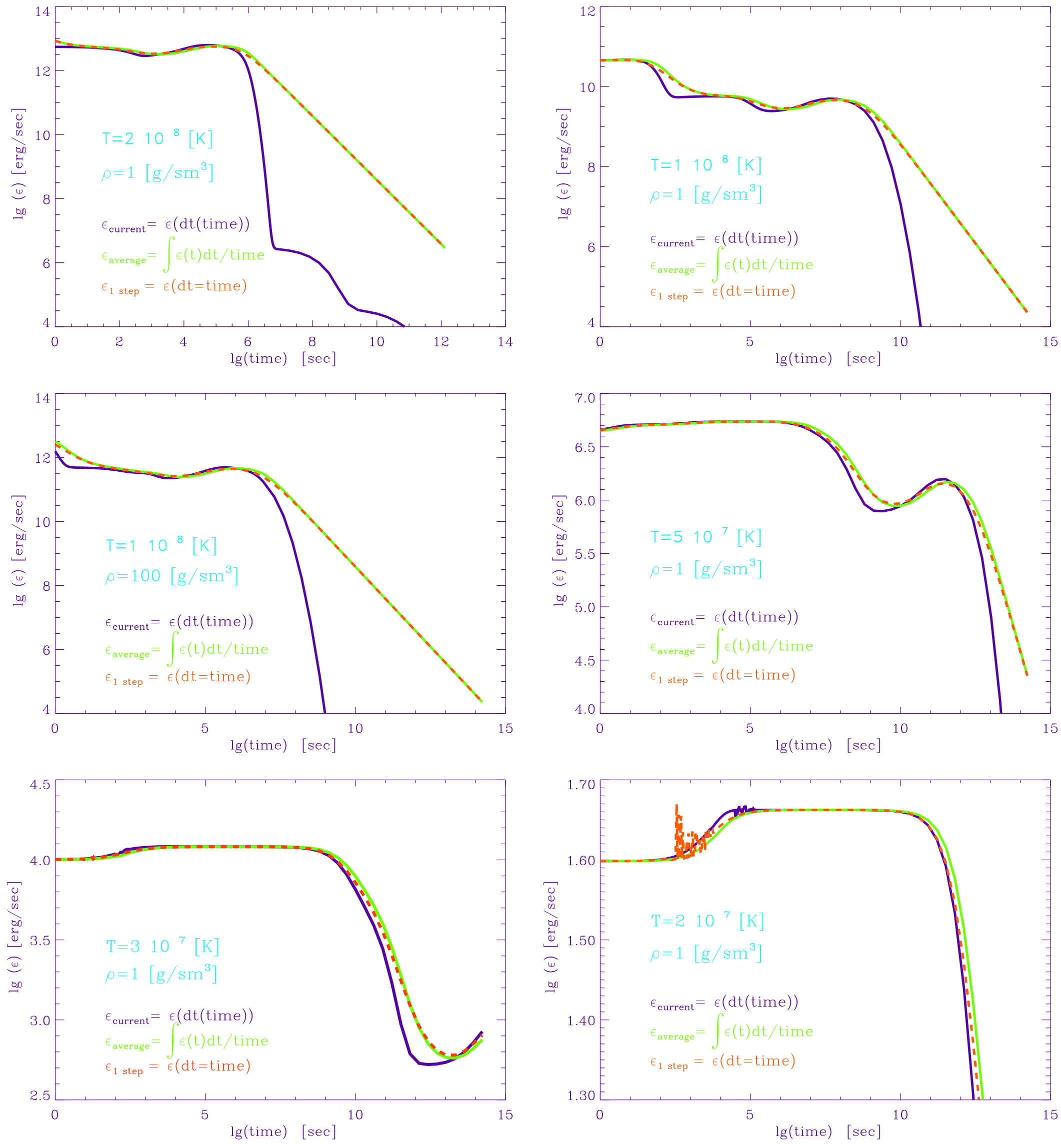

Figure C.2: Energy production rates (by NRN). There are diagrams for different values of the temperature.

time interval. Fig. C.2 presents the results of these calculations for different values of temperature and for a different density (just to show that the value of density does not have a strong effect on the characteristic behavior of the hot-CNO nucleosynthesis). Fortunately, for a large temperature range, the code works fine for a wide range of time steps. Surprisingly, it was found, that just in the case of relatively low temperature ($T_7 \approx 2$), the code is numerically unstable for small time step like $10 - 10^4$ sec and the resulting energy rate slightly declines from the average energy rate for a time step of more than 10^4 years. Such small time steps do not usually occur in normal evolutionary calculations, but are likely to be required for the case of calculations with hydrogen injection in the high temperature part of the star. This instability does not strongly affect the star's structure, but can amplify common numerical instability.

C.1.4 Energy generation calculations in a well mixed convective zone

The time step used in standard evolutionary calculations is normally large enough to consider the mixing in the convection zone as complete mixing. The mixing is usually calculated in two steps: first the composition change in each layer is calculated and then the composition is averaged over the convective region. The implicit scheme for composition changes we use can be sensitive to the assumption of how these changes take place. The total exhaustion of the nuclear fuel in a high temperature zone for the case of convective mixing might be stronger due to the inflow of nuclear fuel from other parts of the convection zone where the nuclear reactions are not so efficient. We therefore provide an alternative scheme we use for calculations of nuclear burning in a convective zone.

One can write the system of equations for the composition changes for the convective zone. Let us consider $\vec{H}$ – the composition vector and R_k – the matrix operator on the composition vector $\vec{H}$ at the level k; the resultant vector at each layer k will be the changes in the composition due to nuclear reactions:

$$d\vec{H}_{\rm nuc}(k) = R_k(dt, T(k), \rho(k), \vec{H}_t(k)), \tag{C.2}$$

where

$$\vec{H}_t(k) = \vec{H}(k) + d\vec{H}_{nuc}(k) \tag{C.3}$$

In the case of convection in N layers we can find one common vector of changes as:

$$d\vec{H}_{\rm nuc} = \sum_{k=1}^{N-1} R_k \frac{\Delta m_k}{M} \; . \tag{C.4}$$

here

$$R_k = (R_k(dt, T(k), \rho(k), \vec{H}_t(k)) + R_k(dt, T(k+1), \rho(k+1), \vec{H}_t(k+1)))/2 \; , \tag{C.5}$$

$$\Delta m_k = m(k+1) - m(k) \; , M = \sum_{k=1}^{N-1} \Delta m_k \tag{C.6}$$

This system of equations is solved iteratively. It also requires less operations than the calculations of the nuclear burning in each layer.

C.1.5 Initial composition

As an initial chemical composition the chemical composition provided by the ZAMS model is used. Since a larger number of species is required for the NRN, for all species, not included in a ZAMS star model, the solar abundance from Cameron (1982) were applied. To model stars with compostion as in LMC, abundances for heavy elements are taken as a half of solar abundance.

C.2 Mesh Points Refining

Let us consider a vector of control variables $Y(j)$ (temperature, pressure, e.t.c). We define $DY(i,j)$ as the difference between 2 neighboring mesh-points i and $i+1$, $DY(i,j) = Y(i+1,j) - Y(j+1)$. The values $DY_{\rm right}(j)$ and $DY_{\rm left}(j)$ represent the tolerable interval for the difference between 2 neighboring mesh-points for the variable $Y(j)$: $DY(i,j)$ should not be greater then $DY_{\rm right}(j)$ and if the interval is less then $DY_{\rm left}(j)$, the mesh point can be removed.

Let us define the next quantities:

$${\rm tol}_{\rm right}(i,j) = \frac{|DY(i,j)|}{|DY_{\rm right}(j)|}, \;\; {\rm tol}_{\rm left}(i,j) = \frac{|DY(i,j)|}{|DY_{\rm left}(j)|} \; .$$

$\mathrm{tol}_{\mathrm{right}}(i,j)$ characterizes how $DY(i,j)$ differs at mesh point i for a variable j from the tolerable maximum. The necessary condition is $\mathrm{tol}_{\mathrm{right}}(i,j) \leq 1$. If $\mathrm{tol}_{\mathrm{right}}(i,j) > 1$ at least one or more points has to be added.

$\mathrm{tol}_{\mathrm{left}}(j)$ defines how $DY(j)$ overlaps a minimal allowed value. The satisfactory value is $\mathrm{tol}_{\mathrm{left}}(j) \geq 1$. If $\mathrm{tol}_{\mathrm{left}} < 1$, one or more points can be removed.

The condition for having more points is the existence of at least one rapidly changing variable; so for each point i we find

$$TOL_{\mathrm{right}}(i) = \max_{(j)}\{\mathrm{tol}_{\mathrm{right}}(i,j)\} > 1 \ .$$

The first condition to remove the next mesh point is that for all the variables at the mesh point i will be $Tol_{\mathrm{left}}(i,j) < 1$, so

$$TOL_{\mathrm{left}}(i) = \max_{(j)}\{\mathrm{tol}_{\mathrm{left}}(i,j)\} < 1 \ .$$

The second condition for the removal of one mesh point is that after the removal of the mesh point the interval between two updated mesh points in a tolerable interval will satisfy the condition:

$$TOL2_{\mathrm{right}}(i) = \max_{(j)}\{\frac{|Y(i+2,j) - Y(i,j)|}{|DY_{right}(j)|}\} < 1$$

If we avoid the exclusion of the points which sharply change the sign of the differential and only remove the points with the same sign of the differential, the condition can be rewritten as the stronger constraint:

$$TOL2_{\mathrm{right}}(i) = \max_{(j)}\{TOL_{\mathrm{right}}(i+1) + TOL_{\mathrm{right}}(i)\} < 1$$

Appendix D

The hydro-movie code

The hydro-movie code provides the visual representation of the hydrodynamical simulations (for the 2d case, 3d it can only show a chosen slice). The main idea of a code like this (design and X-windows engine) has been borrowed from A. Kritsuk in 1998 and has been substabtially changed since then. It was mainly written to achieve a faster speed for the video representation (working directly with X-windows) compared to graphics packages available at the moment . Video representation is important for the case of hydro-simulations – it helps to better understand what is going on as the results are presented not as a static graph, but as a dynamically evolving picture (a human factor). It also makes it more comfortable to trace almost any possible variables and creates mpeg-movie. Basically the code consists of two parts: the X-windows Tcl-tk shell (see Fig. D.1) and the code itself (the code can be called from the command line as well, but it is more convenient to use the Tcl-tk shell with pop-up menus). The code itself is written using C++ and has about 5000 lines. It is extremely easy to adapt this code for any other input data. Also, some modifications have been done on the advise of Ph. Podsiadlowski, which have later been found as extremely useful (e.g. the velocity field). Below we describe the options list for the code. The results of the work of the code itself have been resented in Chapter 4.

Variables

The code shows the following values:

- Thermodynamic variables: density, pressure, temperature, relative density, relative pressure, relative temperature, entropy and adiabatic constant
- Velocities: all 3 components of the velocity, the velocity modulus, velocity divergence, ve-

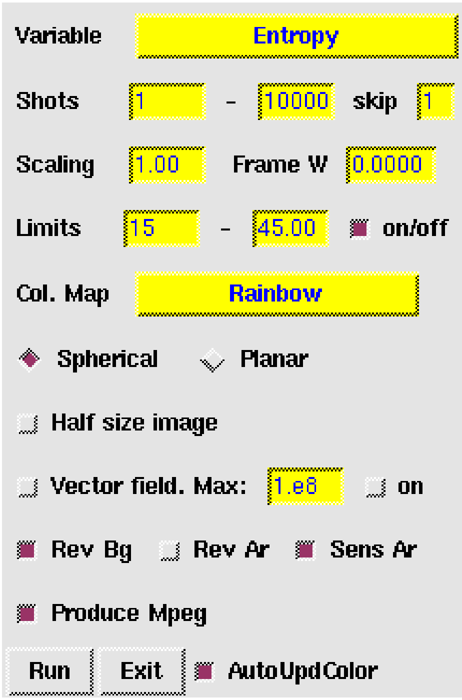

Figure D.1: The Tcl-tk shell for the Hydro Movie.

locity vorticity, Mach Number, Angular Momentum

– Energies: Kinetic Energy, Internal Energy, Total Energy

– Abundances: Hydrogen, Helium, Carbon, Oxygen, He3, neutron, Z

Shots

Numbers of output files to show (will be shown each *skip* number), starting from the left number to the right shot number).

Scaling

The original size of the X-window is defined as 200 dot points in the y-direction for a screen and x-size is scaled in respect to the y-size as in the physical domain. The *scaling* allows the increase or decrease of the viewable area.

Limits

The code automatically finds the maximum and minimum values. But sometime it is more convenient to look at the values only in some interval; this interval can be defined in the *Limits* values (the switch box should be turned on).

Color Maps

Different variables can be seen better in different color maps, especially if the variables are symmetrical with respect to zero. Normally Color Maps are chosen for any variable apriory and are updated automatically (when the variable is chosen), but this can be changed. Also, to prevent this feature, the box “AutoUpdatColor” should be ticked off.

Geometry

To show the picture in planar or polar coordinates. By default it is polar coordinates.

Vector field

On/off - will show arrows directed in the direction of the velocity at this point. Arrows can be scaled, by default it uses the maximum value. Arrows can be black/white (box reverse arrow) or depend on the background (they will automatically be black for a light background and white for a dark background at the same slide).

MPEG

With the MPEG box ticked on, the program will swap out images to later create a MPEG movie or to a graphic file.

Appendix E

The hydro-movies

At the attached CD-ROM you can find 7 mpeg-movies:

Four of them shows the "standard" stream (see subsection 4.2.1): **x.mpeg** shows the hydro gem composition at the region of interest, **S.mpeg** shows the entropy, **s.mpeg** shows the adiabatic constant, **div.mpeg** shows the velocity divergence.

Three other movies are devoted to simulations including nuclear burning: **s_nuc_steady.mpeg** shows the entropy for the case of a stream simulations with steady nuclear burning, **t_nuc.mpeg** and **d_nuc.mpeg** shows temperature and density for the case with the nuclear run-away (see subsection 4.2.5).

Bibliography

[1] Allen D. A., Meikle W. P. S., Spyromilio J., 1989. *Nature* **Vol. 342**, 403

[2] Arnett D., 1994. *American Astronomical Society Meeting*, **v. 185**.

[3] Baraffe I., El Eid M. F., Prantzos N., 1993. *Astr. Astrophys.* **Vol. 258**, 367.

[4] Barkat Z., Wheeler J.C., 1988. *Astrophys. J.* **Vol. 332**, 247.

[5] Blanco V. M., 1987. in: *ESO Workshop on the SN 1987A*, Garching, Federal Republic of Germany, July 6-8, 1987, Proceedings, 27.

[6] Beer H., Voss, F., Winters, R.R., 1992.*Astrophys. J. Suppl. Ser.* **Vol. 80**, 403.

[7] Bisnovatyi-Kogan, G.S., 2001. *Stellar Physics Vol2: Stellar Evolution and Stability*, Springer-Verlag Berlin and Heidelberg GmbH & Co. KG.

[8] Bisikalo D.V., Boyarchuk A.A., Kuznetsov O.A., Chechetkin V.M., 1997. *Astronomy Reports*, **Vol. 41** (issue 6), 794.

[9] Bondi H. , Hoyle F., 1944. *MNRAS* **Vol. 104**, 273.

[10] Busso M., Gallino R., 1985. *Astr. Astrophys.* **Vol. 151**, 205.

[11] Burbidge E.M. , Burbidge G.R., Fowler W.A, Hoyle F., 1957. *Rev.Mod.Phys.* **Vol. 29**, 547.

[12] Cameron A.G.W., 1960. *Astron. J.* **Vol. 65**, 485.

[13] Cameron A.G.W., 1982. *Essay in Nuclear Astrophysics*, ed. C. Barners, D. Clayton, and D. Schramm (Cambridge Univ. Press: Cambridge).

[14] Cannon R., 1992. *Stars With Compact Cores* Ph.D. Thesis, Cambridge University, Cambridge.

[15] Cannon R., 1993. *MNRAS* **Vol. 263**, 817.

[16] Chechev V. P., Kramarovskii Ia. M., 1981, *SvPhU*, **Vol.134**, 431

[17] Chevalier R.A., Soker N., 1989. *Astrophys. J.* **Vol. 341**, 867.

[18] Clayton D.D., Fowler W.A., Hull T.E., Zimmerman B.E., 1961. *Ann.Phys* **Vol. 12** , 331.

[19] Colella P., Woodward P.R., 1984. *J. Comp. Phys.* **Vol. 54**, 174.

[20] Collins T.J.B., Frank A., Bjorkman J.E., Mariol Livio 1999. *Astrophys. J.* **Vol. 512**, 322.

[21] Crotts A.P.S., Heathcote S.R., 1997. *American Astronomical Society Meeting*, 191, 40.

[22] Cox A. N., Vauclair S., Zahn, J.P., 1983, *Astrophysical process in upper main sequence stars*, 13th Advanced Course of the Swiss Society of Astronomy and Astrophysics (SSAA), Saas-Fee, 21-26 March, 1983, Sauverny: Geneva Observatory, 1983, edited by Cox, A.N.; Vauclair, S.; Zahn, J.P

[23] Denissenkov P.A., Ivanova N.S., Weiss A., 1999, *Astr. Astrophys.* **Vol. 341**, ,181

[24] Eggleton P.P., 1983. *Astrophys. J.* **Vol. 268**, 368.

[25] Eggleton P.P., Faulkner J. 1981. *Physical processes in red giants; Proceedings of the Second Workshop*, Erice, Italy, September 3-13, 1980, 179

[26] Faulkner J. 1997. in *Advances in Stellar Evolution, Proceedings of the Workshop Stellar Ecology*, held in Marciana Marina, Elba, Italy, 23-29 June 1996, 9

[27] Faulkner J. 2000. in Podsiadlowski Ph., Rappaport S., King A.R., D'Antona F., Burderi L., eds, *Evolution of Binary and Multiple Star Systems*, *ASP Conf. Ser.*, **Vol. 229**, 3.

[28] Filippenko A.V., Dickinson M., 1990. *IAU Circ.*, 5003, 2.

[29] Filippenko A. V., Hamann, F., 1999. *IAU Circ.*, 7086, 2.

[30] Fransson C. et al., 1989. *Astrophys. J.* **Vol. 336**, 429

[31] Gilman P.A. 2000. *Solar Physics*, **Vol. 192**, 27.

[32] Harrison T.G., Edwards T.W., 1980. *Astrophys. J.* **Vol. 187**, 303.

[33] Heger A., Langer N., Woosley S.E, 2000. *Astrophys. J.* **Vol. 528**, 368.

[34] Henyey L. G., Wilets L., Bohm K. H., Lelevier, R., Levee, R. D, 1959. *Astrophys. J.* **Vol. 129**, 628

[35] Henyey L. G., Forbes J. E., Gould N. L., 1964. *Astrophys. J.* **Vol. 139**, 306

[36] Hillebrandt W., Meyer F. 1989. *Astr. Astrophys.* **Vol. 219**, L3

[37] Hjellming M.S., 1989. *Rapid mass transfer in binary systems*, Ph.D. Thesis Illinois Univ. at Urbana-Champaign, Savoy.

[38] Hjellming M.S., Tamm R.E., 1991. *Astrophys. J.* **Vol. 370**, 716.

[39] Hjellming M.S., Webbink R.F., 1987. *Astrophys. J.* **Vol. 318**, 794.

[40] Heger A. , Langer N., 1998. *Astr. Astrophys.* **Vol. 334**, 210.

[41] Höflich P., 1988. invited talk *Spectarl analysis of SN 1987A: the first 7 months*.

[42] Hut P., 1980. *Astr. Astrophys.* **Vol. 92**, 167.

[43] Ivanova N.S., 1998 in proceeding of the symposium *Unsolved Problems in Stellar Evolution* (Baltimore, USA, May'4-7, 1998), 32

[44] Joss P. C., Podsiadlowski Ph., Hsu J. J. L. & Rappaport S., 1988. *Nature* **Vol. 331**, 237

[45] Kahane C., Audinos P., Barnbaum C., Morris M., 1996, *Astr. Astrophys.* **Vol. 314**, 871

[46] Kippenhahn R., Weigert A. and Hofmeister E., 1967, *Methods in Computational Physics* , **Vol. 7**, ed. B.Aider & M.Rothenbeg (New York:Academic), 129

[47] Kercek A., Hillebrandt W., Truran J.W., 1998. *Astr. Astrophys.* **Vol. 337**, 379.

[48] Kopal Z., 1968, *Ap&SS* **Vol. 1**, 411

[49] Kopal Z., 1972a, *Ap&SS* **Vol. 17**, 161

[50] Kopal Z., 1972b, *Ap&SS* **Vol. 18**, 287

[51] Kritsuk A., Bohringer H., Müller E., 1998. *MNRAS* **Vol. 301**, 343.

[52] Kruszewski A. 1963. Acta Astronomica, 13, 107.

[53] Lai D., Rasio F., Shapiro S.L. 1993. *Astrophys. J.* **Vol. 406**, 63.

[54] Lai D., Rasio F., Shapiro S.L. 1994. *Astrophys. J.* **Vol. 420**, 811.

[55] Lambert et. al., 1986. *Astrophys. J. Suppl. Ser.* **Vol. 62**, 373

[56] Landau L.D., Lifshitz E.M., 1959. *Fluid Mechanics*, Course of theoretical physics, Oxford: Pergamon Press, 1959

[57] Langer N., Arkorogi J.-P., Arnould M., 1989. *Astr. Astrophys.* **Vol. 210**, 187.

[58] Langer N., El Eid M. F., Baraffe I. 1989, *Astr. Astrophys.* **Vol. 224L**, 17

[59] Langer N. 1991a. *Astr. Astrophys.* **Vol. 248**, 531.

[60] Langer N. 1991b. *Astr. Astrophys.* **Vol. 252**, 669.

[61] Langer N., 1997. *The Eddington Limit in Rotating Massive Stars*, in: *Luminous Blue Variables: Massive Stars in Transition.* ASP Conference Series; Vol. 120, 83.

[62] Lauterborn D., Refsdal S., Roth M. L., 1971a. *Astr. Astrophys.* **Vol. 10**, 97

[63] Lauterborn D., Refsdal S., Roth M. L., 1971a. *Astr. Astrophys.* **Vol. 13**, 119

[64] LeVeque R. J., 1998. *Journal of Computational Physics*, 146, 346.

[65] Limber D.N., 1963. *Astrophys. J.* **Vol. 138**, 1112.

[66] Livio M., Soker N. 1988. *Astrophys. J.* **Vol. 329**, 764.

[67] Iben, I.Jr., Livio M. 1993. *PASP* **Vol. 105**, 1373.

[68] Lubow S.H., Shu F.U., 1975. *Astrophys. J.* **Vol. 198**, 383.

[69] Lubow S.H., Shu F.U., 1976. *Astrophys. J.* **Vol. 207**, L53.

[70] Lundqvist P., Fransson C., 1996, *Astrophys. J.* **Vol. 464**, 924

[71] Maeder A., Meyner G. 2000, *Annu. Rev. Astron. Astropys.* **Vol. 38**, 143

[72] Malagoli A., Cattaneo F., Brummell N. H., 1990. *Astrophys. J.* **Vol. 361**, 33.

[73] Mazzali P.A., Chugai N.N., 1995. *Astr. Astrophys.* **Vol. 303**, 118-126.

[74] Mazzali P.A., Lucy L.B., Butler K., 1992. *Astr. Astrophys.* **Vol. 258**, 399-411.

[75] Meyer F., Meyer-Hofmeister E. 1979. *Astr. Astrophys.* **Vol. 78**, 167.

[76] Meyer F., 1997. *MNRAS* **Vol. 285**, L11-L14.

[77] Fryxell B.A., E. Müller E. , Arnett W.D., 1989. *Max-Planck-Institut für Astrophysik Report* **449**, Garching, Germany.

[78] Nelson A. F., Benz W., Arnett W. D., 1994. *American Astronomical Society Meeting*, **Vol. 185**.

[79] Newman, M., 1978. *Astrophys. J.* **Vol. 219**, 676-689.

[80] Ostriker J.P., 1975. paper presented at *The Structure and evolution of Close Binary Systems, IAU Symp. 73*.

[81] Packet, W., 1981, *Astr. Astrophys.* **Vol. 102**, 17

[82] Paczyński B, 1976. in *The Structure and evolution of Close Binary Systems*, IAU Symp. 73, Combridge, ed. P.Eggleton, D. Mitton and J.Whelan, 75.

[83] Panagia N. et al., 1996. *Astrophys. J.* **Vol. 459**, L17

[84] Podsiadlowski Ph., 1989. *it Binary Models for SN1987A* Ph.D. Thesis, MIT.

[85] Podsiadlowski Ph., Joss P. C. . 1989. *Nature* **Vol. 338**, 401

[86] Podsiadlowski Ph., Joss P. C. , Rappaport S. 1990. *Astr. Astrophys.* **Vol. 227**, L9.

[87] Podsiadlowski Ph., 1992. *PASP* **Vol. 104**, 717.

[88] Podsiadlowski Ph., Joss P. C., Hsu J. J. L., 1992. *Astrophys. J.* **Vol. 391**, 246

[89] Podsiadlowski Ph. 1997. *Binary evolution and the Progenitor of SN 1987A*, in *SN 1987A: Ten years after*, eds. M. M. Phillips & N. B. Suntzeff, PASPC, in press

[90] Podsiadlowski Ph., 2000. in Podsiadlowski Ph., Rappaport S., King A.R., D'Antona F., Burderi L., eds, *Evolution of Binary and Multiple Star Systems*, *ASP Conf. Ser.*, **Vol. 229**, 239.

[91] Podsiadlowski Ph., Rappaport S., 2000. *Astrophys. J.* **Vol. 291**, 246

[92] Porter D.H., Woodward P.R., 1994. *Astrophys. J. Suppl. Ser.* **Vol. 93**, 309.

[93] Press W. H., Smarr, L. L., Wiita, P., J.1975, *Astrophys. J.* **Vol. 202**, L135

[94] Raiteri C. M., Gallino R., Busso M., Neuberger D., Kaeppeler F., 1993. *Astrophys. J.* **Vol. 419**, 207-223.

[95] Rasio F. A., Livio M., 1996. *Astrophys. J.* **Vol. 471**, 366.

[96] Ritter H., 1995. in the *proc. of the NATO Advanced Study Institute on Evolutionary Process in Binary Stars* **Vol. 477** 223.

[97] Renzini A., Greggio L., Ritossa C. and Ferrario L., 1992 *Astron. J.* **Vol. 400**, 280

[98] Robinson F.J., Chan K.L., 2001. *MNRAS* **Vol. 321**, 723.

[99] Rossi P., Bodo G., Massaglia S., Ferrari A., 1997. *Astr. Astrophys.* **Vol. 321**, 672.

[100] Ruffert M., Rampp M., Janka H.-T, 1997. *Astr. Astrophys.* **Vol. 321**, 991.

[101] Ruffert M., Janka H.-T, 1998. *Astr. Astrophys.* **Vol. 338**, 535.

[102] Ruffert M., Janka H.-T, 1999. *Astr. Astrophys.* **Vol. 344**, 573.

[103] Russell S. C., Dopita M. A., 1992, *Astrophys. J.* **Vol. ,**, 384, 508

[104] Saio H., Nomoto K. , Kato M., 1988a. *Nature* **Vol. 342**, N23, 403-405.

[105] Saio H., Nomoto K. , Kato M., 1988b. *Astrophys. J.* **Vol. 331**, 338.

[106] Sandquist E., Taam R. E., Burkert A., 2000. *Astrophys. J.* **Vol. 533**, 984

[107] Savonije G. J., Papaloizou J. C. B., 1985. *Interacting binaries* proceedings of the Advanced Study Institute, Cambridge, England, July 31-August 13, 83.

[108] Sawada K., Hachisu I., Matsuda T., 1984, *MNRAS* **Vol. 1984**, 206

[109] Schatzman E., Maeder A., Angrand F. , Glowinski R., 1981. *Astr. Astrophys.* **Vol. 96**, 1.

[110] Scherrer P.H., Bogart R. S., Bush R. I., Hoeksema J. T., Kosovichev A. G., Schou J., Rosenberg W., Springer L., Tarbell T. D., Title A., Wolfson C. J., Zayer I., MDI Engineering Team, 1995. *Solar Physics*, 162, 129.

[111] Smith L. J., Nota A., Pasquali A., Leitherer C., Clampin M., Crowther P.A., 1998. *Astrophys. J.* **Vol. 503**, 278.

[112] Sonneborn G. et al., 1997. *Astrophys. J.* **Vol. 477**, 848

[113] Suess H.E., Urey H.C., 1956. *Rev.Mod.Phys* **Vol. 28**, 53.

[114] Taam R. E., Sandquist E., 1998. *ASP Conf. Series*, **Vol. 138**, 349.

[115] Taam R. E., Sandquist E., 2000. *Ann.Rev.Astron.Astrophys.*, **Vol. 38**, 113.

[116] Thorne K. S., Żytkow, A. N., 1975. *Astrophys. J.* **Vol. 199**, 19

[117] Truran, 1981 *Synthesis of the heavy elements*, In: *Nuclear astrophysics; Proceedings of the International School of Nuclear Physics, Erice, Italy, March 25-April 6, 1980*, Oxford, Pergamon Press, 161.

[118] Urpin V. A., Shalybkov D. A. , Spruit H. C., 1996. *Astr. Astrophys.* **Vol. 30**, 455.

[119] Wampler E.J., Wang L., Baade D., Banse K., D'Odorico S., Gouiffes C., Tarenghi M, 1990. *Astrophys. J.* **Vol. 362**, L13-L16.

[120] Williams R.E., 1987a. *in Proc. IAU Coll.* **Vol. 108**, 118.

[121] Williams R.E., 1987b. *Astrophys. J.* **Vol. 320**, L117-L120.

[122] Wang L., 1991. *Astrophys. J.* **Vol. 246**, L69

[123] Wang L., Mazzali P.A., 1991. *Astr. Astrophys.* **Vol. 241**, L17-L20.

[124] White G. L., Malin D. F., 1987. *Nature* **Vol. 327**, 36-38..

[125] Woosley S.E., 1988. *Astrophys. J.* **Vol. 330**, 218-253.

[126] Woosley S.E., Heger A., Weaver T. A., Langer N., 1997. in *SN 1987A: Ten years after*, eds. M. M. Phillips & N. B. Suntzeff, PASPC, in press

[127] Zahn J.P., 1975. *Astr. Astrophys.* **Vol. 41**, 329.

[128] Zahn J.P., 1992. *Astr. Astrophys.* **Vol. 265**, 115.

[129] Zeldovich Ya.B., Raizer Yu.P., 1966. *Physics of Shock Waves and High-Temperature Hydrodynammics Phenomena*, Academic Press, New York and London.